UNIVERSITAT
POLITÈCNICA
DE VALÈNCIA

W BEC
Wireless In-Body
Environment

iTeAm
Instituto de Telecomunicaciones
y Aplicaciones Multimedia

In-body to On-body Experimental UWB Channel Characterization for the Human Gastrointestinal Area

Instituto de Telecomunicaciones y Aplicaciones Multimedia

Universitat Politècnica de València

A thesis for the degree of

PhD in Technologies for Health and Well-Being

Valencia, October 2019

Author:
Sofia Pérez Simbor

Supervisors:
Dr. Concepción García Pardo
Prof. Narcís Cardona Marcet

When the endoscope won't reach,
the wireless will be there.
After one day of fasting,
the capsule will be traveling
The pill will be swallowed,
your inside will be captured.
The photos though,
are not enough.
But don't worry,
the UWB signal has quality.
Now the path loss has come
but it won't stay long.
The model will help
to your transmission detect!.

Acknowledgements

Reduir tres anys d'agraïments en solament unes línies es difícil per no dir que és impossible. Per altra banda, aquest es segurament l'únic apartat de tota la tesi on puc parlar amb llibertat sense estar sotmesa a un idioma i una manera de redactar que no em defineixen. De totes formes vaig a intentar anomenar a totes aquelles persones que han estat amb mi sempre, des del comencament fins a la fi d'aquesta etapa. Primer, i sens dubte, agrair a ma mare, hi han milers (o milions) de raons, però, com he de resumir, diré que sempre ha aguantat lo inaguantable recolçant-me sense dubtar-ho a cap moment. Per descomptat a Laia i Máximo. A mi padre y a Amparo. Tampoc puc oblidar a la tia Maria Jesús ni a la meua cosina Noelia. Y tampoco a mi tia Carmen, tio Claudio y mi primo Claudio. Per descomptat, Ferran, la nova incorporació a la familia.

Por otro lado quedan las otras personas imprescindibles que han estado ahí mucho tiempo y espero que no se vayan. Julia, Marta, David, Héctor, Rubén, Nuria, Ana, Laura, Paula, Silvia, Fran, Juan, Roman, Jose Manuel, Adrian, Jorge, Manolo. La gente que llegó a mitad, Neffer, Tomo. Y luego en general, aquellos que hacen la vida más fácil, ya sea con palabras o con espadas.

Durante este tiempo, he compartido espacio durante muchas horas al día con mis companeros de trabajo en el MCG, que son muchos, especialmente, con Martina, Sergio y Alejandro. Además mi supervisora Conchi, que siempre me ha ayudado con paciencia y de la cual he aprendido mucho. Por supuesto también Narcís.

And last but not least, I want to thank everyone on the WIBEC project, ESRs to which I shared multiple things, Reinier, Andrea, Xiao, Mehrab, Pritam, Faheem, Mohammad, Pengfei, Rafa, Mirko, Giulia, Salman, Deepak, supervisors, and everyone who has been there. Smart people that made all the trainings, secondments and meetings interesting, fun, and unforgettable.

A tots vosaltres, gràcies!

Abstract

The current global population in developed countries is becoming older and facing an increase in diseases mainly caused by age. New medical technologies can help to detect, diagnose and treat illness, saving money, time, and resources of physicians. Wireless in-body devices opened a new scenario for the next generation of medical devices. Frequencies like the Ultra Wide-band (UWB) frequency band (3.1 - 10.6 GHz) are being considered for the next generation of in-body wireless devices. The small size of the antennas, the low power transmission, and the higher data rate are desirable characteristics for in-body devices. However, the human body is frequency dependent, which means higher losses of the radio frequency (RF) signal from in- to out-side the body as the frequency increases. To overcome this, the propagation channel has to be understood and known as much possible to process the signal accordingly. This dissertation aims to characterize the (RF) channel for the future of in-body medical devices.

Three different methodologies have been used to characterize the channel: numerical simulations, phantom measurements, and living animals experiments. The phantom measurements were performed in a novel testbed designed for the purpose of in-body measurements at the UWB frequency band. Moreover, multi-layer high accurate phantoms mimicking the gastrointesintal (GI) area were employed. The animal experiments were conducted in living pigs, replicating in the fairest way as possible the phantom measurement campaigns. Lastly, the software simulations were designed to replicate the experimental measurements. An in-depth and detail analysis of the channel was performed in both, frequency and time domain. Concretely, the performance of the receiving and transmitting antennas, the effect of the fat, the shape of the phantom container, and the multipath components were evaluated. Finally, a novel path loss model was obtained for the low UWB frequency band (3.1 - 5.1 GHz) at GI scenarios. The model was validated using the three methodologies and compared with previous models in literature. Finally, from a practical case point of view, the channel was also evaluated for UWB signals at lower frequencies

ABSTRACT

(60 MHz) for the GI area. In addition, for the next generation of leadless pacemakers the security link between the heart and an external device was also evaluated.

The results obtained in this dissertation reaffirm the benefits of using the UWB frequency band for the next generation of wireless in-body medical devices.

Resumen

La población mundial en países desarrollados está envejeciendo y con ello existe un aumento de enfermedades en gran medida causadas por la edad. Las nuevas tecnologías médicas pueden ayudar a detectar, diagnosticar y tratar estas enfermedades y con ello ahorrar dinero, tiempo y recursos de los sistemas sanitarios. Las tecnologías inalámbricas implantables han abierto un nuevo panorama para la próxima generación de tecnologías médicas. Frecuencias como la *Ultra Wide-Band* (UWB) de 3.1 a 10.6 GHz están siendo consideradas para la nueva generación de dispositivos inalámbricos para dentro del cuerpo humano. Las características como el reducido tamaño de las antenas, la baja potencia de transmisión y la alta velocidad de datos son las más buscadas en este tipo de dispositivos. El problema surge porque el cuerpo humano depende de la frecuencia de modo que a mayores frecuencias, mayores son las pérdidas por propagación. Conociendo el canal transmisión en se puede solventar el problema de las altas pérdidas. Esta tesis tiene como objetivo caracterizar el canal de radio frecuencia (RF) para la nueva generación de dispositivos médicos implantables.

Para caracterizar el canal se han empleado tres diferentes metodologías: simulaciones numéricas, medidas en *phantom* y experimentos en animales vivos. Las medidas en *phantom* fueron realizadas en un nuevo sistema de medidas expresamente diseñados para medidas de dentro a fuera del cuerpo humano en la banda de frecuencias UWB. Además, se utilizó un novedoso recipiente con dos capas de *phantom* imitando la zona gastrointestinal del cuerpo. Estos *phantoms* fueron creados para este tipo de medidas y son extremadamente precisos a las frecuencias UWB. Para los experimentos en animales se utilizaron cerdos y se intentó reproducir en ellos las medidas previamente realizadas en *phantom*. Las simulaciones software se realizaron con la intención de replicar ambas metodologías. Una vez realizados los experimentos se realizó un extensivo estudio del canal en dominio frecuencial y temporal. Mas en detalle, se compararon las antenas usadas en recepción y transmisión, el efecto de la grasa en el canal, la formas del recipiente contenedor de *phantom* y las componentes

multicamino. Como resultado se ha propuesto un modelo de propagación del canal para la banda baja de las frecuencias UWB (3.1 -5.1 GHz) para la zona gastrointestinal del cuerpo humano. Este modelo de propagación ha sido validado utilizando las tres metodologías previamente descritas y comparada con otros estudios existentes en literatura. Finalmente, se midió el canal de propagación para una determinada aplicación a bajas frecuencias con señales UWB. También se realizaron medidas del canal de propagación en la zona cardíaca del cuerpo humano desde un punto de vista de seguridad de datos.

Los resultados obtenidos en esta tesis confirman los beneficios que tendría la utilización de frecuencias UWB para las futuras generaciones de dispositivos médicos implantables.

Resum

La població mundial a països desenvolupats està envellint-se i enfrontant-se a un augment d'infermetats principalment causades per la edat. Les noves tecnologies mèdiques poden ajudar a detectar, diagnosticar i tractar aquestes malalties, estalviant diners, temps i recursos sanitaris. Els dispositius implantables sense fils han generat un nou panorama per a les noves generacions de dispositius mèdics. Les freqüències com la banda de *UWB* estan sent considerades per a les futures tecnologies implantables. La reduïda grandària de les antenes, la baixa potència de transmissió i les altes velocitats de dades son característiques buscades per als dispositius implantables. Per contra, els éssers humans depenen de la freqüència en el sentit que a majors freqüències, majors les pèrdues per propagació quan el senyal travessa el cos humà d'interior a exterior. Per solventar aquestes pèrdues el canal de propagació s'ha d'entendre i conèixer de la millor manera possible. Aquesta tesi doctoral te com a objectiu caracteritzar el canal de radio freqüència (RF) per a la nova generació de dispositius mèdics implantables.

S'han emprat tres metodologies diferents per a realitzar aquesta caracterització: simulacions software, mesures amb fantomes i experiments amb animals vius. Els experiments amb fantomes es van realitzar a un sistema de mesures dissenyat expressament per a les transmissions de dins a fora del cos humà a les freqüències UWB. També es van utilitzar un contenidor per als fantomes de dues capes, imitant l'area gastrointestinal dels humans. Per als experiments a animals es van emprar porcs, replicant els experiments al laboratori en fantomes de la forma més semblant possible. Les simulacions software foren dissenyades per a imitar les experiments amb fantomes i animals. Després dels experiments el canal de propagació es va investigar exhaustivament des del domini freqüèncial i temporal. S'ha observat com les antenes en transmissió i recepció afecten al senyal, la influència de la grassa, la forma del contenidor de fantoma i les possibles contribucions multicamí. Finalment es proposa un nou model de propagació per a les baixes freqüències UWB (3.1 a 5.1 GHz) per a la zona GI del cos humà. El model es va validar utilitzant les tres metodologies abans

esmentades i també foren comparades amb models ja existents a la literatura. Finalment des d'un punt de vista aplicat, el canal es va avaluar per al senyal UWB a baixes freqüències (60 MHz). A més a més, per a la nova generació de marcapassos sense fil es va investigar el canal des d'un punt de vista de seguretat de dades.

Els resultats obtinguts a aquesta tesi confirmen els avantatges d'emprar la banda de freqüències UWB per a la nova generació de dispositius mèdics implantables.

Table of contents

List of Figures

17

List of Tables

Chapter 1

Introduction

This chapter introduces the topic of this dissertation, the objectives, publications obtained through this research, and the funding that made it possible.

1.1   Background

The current global population in developed countries is decreasing and aging due to the low natality and low mortality of the most developed countries [1]. Longer life expectation as a result of better healthcare and living conditions leads to some medical problems mostly caused by aging, e.g., arrhythmias, tumors, and polyps. Thus, physicians have to attend more patients in less time, which leads to misdiagnosis problems caused by human errors that are derived from the lack of time and extenuation of the physician. Nevertheless, the technology can help to overcome these human factors. Thus, modern medicine develops towards more automatized and reliable methods of prevention, diagnosis, and treatment of diseases. The improvement of drugs (insulin delivery), medical knowledge (biotechnology research), and medical technology (neural implants, pacemakers, ingestible capsules), are examples of modern medicine. Concretely, medical technology is a wide term that includes some different topics such as telemedicine, big data, and medical devices.

For this dissertation, the research was focused on the next generation of in-body wireless medical devices. These have highly increased the possibilities of early detection, treatment, and healing of many diseases. e.g., polyps, diabetes, cancer, heart anomalies. In-body devices are those located inside the human body either in a permanent or temporal time. Moreover, in-body devices are categorized in three main groups: implantables, injectables, and ingestibles [2]. The implantable devices are surgically implanted inside the body and they last

for large periods of time (pacemakers, neural sensors). The injectable ones are microsensors or microstimulators injected by means of a needle. Finally, the ingestible devices are those which are swallowed through the mouth imitating the shape, size, and form of a pill (endoscopic capsules), they usually take pictures, measure biological parameters, or deliver drugs inside the human body. All these in-body devices are meant to cause a minimal impact over the patient, and to be the most effective in time, economical and medical resources. All the wireless in-body devices use the body as the propagation medium. However, the signal is highly distorted due to the heterogeneity of the human body and its frequency dependence. This heterogeneity leads to divide the human body in different scenarios to properly characterize it from a radiofrequency (RF) channel point of view. The gastrointestinal (GI) area of the human body will be the most investigated in this dissertation, but also the cardiac scenario will be explored.

The Wireless Capsule Endoscopy (WCE) is an outstanding device that scales up the working range of the detection of GI diseases. In contrast to the conventional endoscope, which only works until the duodenum, the WCE is an easy-to-swallow pill (approximately 25-30 mm × 10 mm in length and diameter) that takes pictures of the small and large bowel of the patients. Then, the WCE transmits the pictures to a set of receivers that the patient has over the abdomen. Then, such pictures are recorded for later inspection of the physician. This methodology was first used in 2001 [3] and currently is used worldwide. However, it has serious drawbacks such as the amount of time that a physician has to spend in watching all the pictures, the low quality images, and the unexpected movement of the pill inside the body [4]. The next generation of WCE is leading towards the automatization of the process to save time and human resources. Computer vision algorithms are helping in recognition of diseases [5, 6] but they are still in an early stage. Moreover, the localization of the capsule inside the human body is still a challenge that is currently under research [7–10]. Better image quality, higher data rate, and faster processes will enhance the performance of the WCE for the next generation of wireless medical devices.

Besides, the leadless pacemaker is a promising device for the next generation of wireless medical devices. The current pacemaker or the implantable cardioverter defibrillator have shown extremely good performance on the treatment of some diseases such as the bradycardia, tachycardia or heart failure. However, they show some drawbacks like infections, cable breakage or venous stenosis. Thus, the leadless pacemaker will eliminate these problems caused by the leads that current pacemakers have. The leadless pacemaker is still a device under deep research. Some aspects are: the communications [11], placement of the nodes [12], how to charge the device [13], the synchronization [14] of the

signal, and the security of the RF link [15]. The security of the RF channel will be also investigated in this dissertation considering the case when a malicious attacker is trying to interfere the signal between the intra-heart node and the subcutaneous node that serves a bridge between the in-body and the off-body devices.

Regarding the frequency band selected for the signal transmission of in-body devices, a promising RF band for the next generation of in-body wireless devices is the UWB frequency band (3.1 to 10.6 GHz). It has numerous properties that are beneficial for the communications around the body: the low power transmission, the higher data rate, and the smaller size of the antennas are the most relevant for our purposes [16]. Therefore, there are many researchers that are working on this band for different purposes for communications in-, on- and off-body [17–22] (further explanation in Chapter 2). However, as mentioned before, the major drawback of the UWB frequency band is the high path losses that the signal experiences from in- to out-side the body. To overcome this issue, a good understanding of the channel and a proper characterization have to be carried out.

The Ultra Wide-Band signal

The definition of an UWB signal was for some time a question of debate. Luckily the scientific community has arrived to an agreement and there are two main definitions of UWB [16, 23]. A signal is considered to be UWB when the bandwidth of the signal is equal or larger than 500 MHz (UWB with large absolute bandwidth) or when the signal bandwidth is larger than 20% of its carrier frequency (large relative bandwidth). In this dissertation, the first definition will be the most studied at the license free frequency band (3.1 to 10.6 GHz) (Chapter 5 and Chapter 7). Nevertheless, the second definition of UWB will be also considered in Chapter 6.

In addition, the UWB signal can be modulated in different ways. The Multiband Orthogonal Frequency Division Multiplexing (MB-OFDM), where the signal is divided into 500 MHz subbands [24], so the channel is considered frequency independent for every whole subband. On the other hand, some applications not only for body networks [25] but also for other wireless communications applications such as radar or indoor communications [26], use impulse-radio UWB (IR-UWB), where the bandwidth is considerably higher compared to MB-OFDM and the frequency dependence of the channel can play an important role. Results in [25] and [26] showed that to overcome this, the signal has to be recovered with a proper design of the receiver. In our research IR-UWB modulation of the signal is the one considered for all the

experiments and simulations. Therefore, every time the term UWB is used along this dissertation it will be referring to IR-UWB.

1.2 Funding

1.3 Objectives of this dissertation

Hypothesis: If the characterization of the in- to on-body channel at UWB frequencies can be standardized, then it would be independent of the application and the antennas used and it could be employed for the next generation of in-body wireless medical devices.

This dissertation has the objective to characterize the in-body to on-body (IB2OB) channel at the UWB frequency band using software simulations, experimental phantoms, and *in vivo* measurements for the next generation of wireless medical devices. Concretely, the main scenario under interest is the GI area in which different UWB signals are considered. One with large absolute bandwidth from 3.1 to 5.1 GHz, and then a signal with a large relative bandwidth for 60 MHz as central frequency. Moreover, the cardiac scenario was also researched for the next generation of leadless pacemakers.

Firstly, to accomplish with the investigations planned, a dedicated measurement testbed for phantom measurements in laboratory was created. This had the objective to isolate the measurements from the environment and to perform different extensive measurement campaigns to properly obtain the losses that appear in the human body from inside to outside it. The measurements performed in laboratory were replicated in different experiments conducted in living animals. Finally, software simulations replicating both experiments were designed. From this, different characteristics of the channel were obtained, like the propagation losses as a function of the distance, the influence of the frequency in the path loss, the delay characteristics of the channel, or the influence of certain tissues in the propagation losses.

This thesis dissertation is divided as follows, a state of the art is fully detailed in Chapter 2. Then, the system measurements and the methodology

to perform all the experiments and the simulations are described in Chapter 3 and 4. The results are divided in three chapters. Chapter 5 shows the extensive results of the channel characterization for IB2OB GI scenarios for the UWB frequency band. Chapter 6 describes the results for low frequency UWB signals at the GI area and finally Chapter 7 are the results of the characterization of the cardiac channel.

1.4   List of Publications

International Journals

[J1] **S. Perez-Simbor**, C. Andreu, M. Frasson and N. Cardona, "UWB Path Loss Models for Ingestible Devices," in *IEEE Transactions on Antennas and Propagations*, vol. 67, no. 8, pp. 5025-5034, Aug. 2019

[J2] C. Garcia-Pardo, C. Andreu, A. Fornes-Leal, S. Castelló-Palacios, **S. Perez-Simbor**, M. Barbi, A. Vallés-Lluch, N. Cardona, "Ultrawideband Technology for Medical In-Body Sensor Networks: An Overview of the Human Body as a Propagation Medium, Phantoms, and Approaches for Propagation Analysis," *IEEE Antennas and Propagation Magazine*, vol. 60, no. 3, pp. 19-33, June 2018

[J3] M. F. Awan **S. Perez-Simbor**, C. Garcia-Pardo and N.Cardona "Experimental Phantom-based Security Analysis for the Next Generation Leadless Cardiac Pacemaker," *Sensors*, pp. 1-21, 2018

International Conferences

[C1] **S. Perez-Simbor**, M. Barbi, C. Garcia-Pardo, S.Castelló-Palacios, N. Cardona "Initial UWB In-Body Channel Characterization Using a Novel Multilayer Phantom Measurements Setup," in *IEEE Wireless Communications and Networking Conference, WCNC*, Barcelona, Spain, April 2018.

[C2] **S. Perez-Simbor**, K. Krhac, C. Garcia-Pardo, K. Sayrafian, D.Simunic, and N. Cardona, "Impact of Measurements Points Distribution on the Parameters of UWB Implant Channel Model," in *IEEE Conference on Standards for Communications and Networking (CSCN)*, p. 6, Paris, France, October 2018

[C3] **S. Perez-Simbor**, M. Barbi, M. Ramzan, X. Fang, C. Garcia-Pardo, N. Cardona, Q. Wang, N. Neumann, D. Plettemeier, "Experimental Path loss models comparison and localization of Wireless Endoscopic Capsule

in the Ultra Wideband Frequency Band," *Bodynets*, pp.1-11, Oulu, Finland, October 2018

[C4] M. Barbi, **S. Perez-Simbor**, C. Garcia-Pardo, C. Andreu, A. Fornes-Leal, and N. Cardona, "Localization for Capsule Endoscopy at UWB Frequencies using an Experimental Multilayer Phantom," in *IEEE Wireless Communications and Networking Conference, WCNC*, Barcelona, Spain, April 2018

[C5] M. F. Awan *et al.,* "Experimental phantom-based evaluation of Physical Layer Security for Future Leadless Cardiac Pacemaker," in *International Symposium on Personal Indoor and Mobile Radio Communications (PIMRC)*, Bologna, Italy, September 2018

[C6] A. Fornes-Leal, C. Garcia-Pardo, **S. Perez-Simbor** and N. Cardona, "Impact of the Variability of the EM Properties of Biological Tissues on UWB Channel Modelling for Implanted Devices", in *European Association on Antennas and Propagation, (EUCAP)*, p. 5, Krakow, Poland, March-April 2019

[C7] **S. Perez-Simbor**, C. Garcia-Pardo, and N. Cardona, "Initial Delay Domain UWB Channel Characterization for In-body Area Networks", in *13th International Symposium on Medical Information and Communication Technology (ISMICT)* p.5, Oslo, Norway, May 2019

[C8] M. Barbi, **S. Perez-Simbor**, C. Garcia-Pardo, and N. Cardona, "Analysis of the Localization Error for Capsule Endoscopy Applications at UWB Frequencies", in *13th International Symposium on Medical Information and Communication Technology (ISMICT)* p.1-6,Oslo, Norway, May 2019

[C9] M. F. Awan, K. Kansanen, **S. Perez-Simbor**, C. Garcia-Pardo, S. Castelló-Palacios, and N. Cardona, "RSS-Based Secret Key Generation in Wireless In-body Networks", in *13th International Symposium on Medical Information and Communication Technology (ISMICT)* p.1-6,Oslo, Norway, May 2019

[C10] X. Fang, M. Ramzan, Q. Zhang, **S. Perez-Simbor**, Q.Wang, N. Neumann, C. Garcia-Pardo, N. Cardona, and D. Plettemeier, "Experimental In-Body to On-body and In-body to In-Body Path Loss Models of Planar Elliptical Ring Implanted Antenna in the Ultra-Wide Band",in *13th International Symposium on Medical Information and Communication Technology (ISMICT)* p.1-5, Oslo, Norway, May 2019

International Research Visits

[V1] Technische Universität Dresden - Institut für Nachrichtentechnik, Dresden, Germany. July - August 2017 (2 months)

[V2] Oslo University Hospital - Intervention Center, Oslo, Norway. August - December 2018 (4 months)

Research Projects

[P1] Wireless In-body Environment (WIBEC).

– Funding institution: European Union's H2020-MSCA-ITN

– Grant number: 675353

– Start date: 01/01/2016

– Duration: 48 months

COST Technical Documents

[TD1] M. Barbi **S. Perez-Simbor**, C. Garcia-Pardo, S. Castelló-Palacios, C. Andreu, A. Fornes-Leal, "Localization for Capsule Endoscopy at UWB Frequencies using an Experimental Multilayer Phantom," in *5th MC and 5th Technical Meeting* , European COST Action CA15104, IRACON, Graz, Austria, September 2017

[TD2] **S. Perez-Simbor**, M. Barbi, C.Garcia-Pardo, S. Castelló-Palacios and N. Cardona, "Initial UWB In-body Channel characterization Using a Novel Multilayer Phantom Measurements Setup", in *7th MC and 7th Technical Meeting*, European COST Action CA15014, IRACON, Cartagena, Spain, May 2018

[TD3] **S. Perez-Simbor**, C. Andreu, C. Garcia-Pardo, M. Frasson and N. Cardona, "UWB Path Loss Models for Ingestible Devices", *9th MC and 9th Technical Meeting*, European COST Action CA15014, IRACON, Dublin, Ireland, January 2019

National Journals

[NJ6] C. Garcia-Pardo, C. Andreu, A. Fornes-Leal, S. Castelló-Palacios, **S. Perez-Simbor**, M. Barbi, A. Vila-Jimenez, M. Cabedo-Fabres, V. Pons, M. Frasson, A. Valles-Lluch and N. Cardona, "Wireless Communications for Medical In-body Devices: Challenges for In-body Propagation," *Waves Journal*, 2018

National Conferences

[NC1] C. Garcia-Pardo, C. Andreu, *S. Perez-Simbor*, S. Castelló-Palacios, A. Fornes-Leal, M. Barbi, A. Valles-Lluch and N. Cardona,"UWB Propagation for Medical In-Body Devices," *XXXIII Simposium Nacional de la Unión Científica Internacional de Radio, URSI*, p.5, Granada, Spain, September, 2018

Chapter 2

State of the Art

In this section a wide explanation of the Wireless Body Area Networks and all of its characteristics from a channel characterization point of view are described. In addition, the previous channel models present in literature are discussed

2.1 Wireless Body Area Networks

Wireless Body Area Networks (WBANs) are defined as a short-range, wireless communication in the vicinity of, or inside, a human body (but not limited to humans) [27]. On the contrary to the Personal Area Networks (PANs), WBANs are mainly used for medical and healthcare uses. Nevertheless, they can also be applied to other purposes such as entertainment, video streaming or military. WBANs include different few technologies, i.e., not only RF transmission is used but also Human Body Communications (HBC), which uses the electrical current of the human body to propagate the signal or also the molecular communications, which use the biological neuronal networks and molecules to propagate through the human body.

Currently, the standard 802.15.6-2012 [27] defines the frequencies used for the different scenarios around the human body. The Medical Implant Communications Service (MICS) band (from 402 to 406 MHz) is chosen for the communications inside the human body, either in- to in-side or in-to out-side. Nevertheless, this narrowband frequency band has a maximum data rate of 455 kbps. The Industrial Scientific and Medical radio band (ISM) band (2.45 GHz) is also defined for the communications over the human body, and it has a maximum data rate of 971 kbps. Unfortunately, none of these data rates are enough to assure the requirements of the next generation of WCE. Finally, the

standard defines the UWB frequency band (3.1 - 10.6 GHz) as the frequency band for communications from outside the body to external medical devices.

2.1.1 EM properties of the human tissues

Living bodies have different tissues, organs, liquids, and elements which vary in composition, shape, color, as well as, EM properties. The permittivity (ε) and the conductivity (σ) are the main properties that determine some propagation effects under interest such as the path loss, the reflection, or velocity of propagation through the tissues. (The permeability μ is associated with magnetic materials, so, since the human body is nonmagnetic it is considered as in free space [28]). The ε is given as the relation between the relative permittivity (ε_r) and the free space permittivity (ε_0) $\varepsilon = \varepsilon_r \varepsilon_0$. Since the ε_0 is a known constant, the ε is only ε_r dependent, which is a dimensionless, complex and frequency-dependent term. In addition, ε_r is given in the Eq. 2.1,

$$\varepsilon_r = \varepsilon_r^{'} + j\varepsilon_r^{''} \tag{2.1}$$

where $\varepsilon_r^{''}$ is known as the dielectric constant and the complex part $\varepsilon_r^{''}$ is the loss factor. Moreover, $\varepsilon_r^{''} = \sigma/(\omega\varepsilon_0)$, being $\omega = 2\pi f$, the angular frequency. The loss factor shows the relation between the permittivity and the conductivity [29]. Commonly, the values used for the characterization of the human body are the dielectric constant and the loss factor. Furthermore, in literature, it is often used to characterize the human tissues the empirical values obtained by Gabriel in [30]. Even though many investigators have reported different empirical values for different tissues [31–33], this dissertation will be taken as the reference values the ones given by Gabriel, since after all they are the most used in literature. In the Fig. 2.1 EM properties (dielectric constant and loss factor) of the main tissues at the gastrointestinal area are plotted.

As seen in Fig. 2.1 muscle, colon, and small bowel have similar dielectric constant and loss factor, which allows the interchangeability of the tissues for certain applications, such as software simulations or phantom measurements. Contrarily, the fat shows lower values for both the dielectric constant and the loss factor.

2.1.2 Scenarios in WBANs

Because of the singular characteristics of the human body, the scenario, where the RF link operates, influences some of the characteristics of the WBANs, such as the channel model or the antennas to use. The 802.15.6 standard [27], defines seven different scenarios according to the position of the transmitting and receiving antenna at the human body. The antennas located inside the
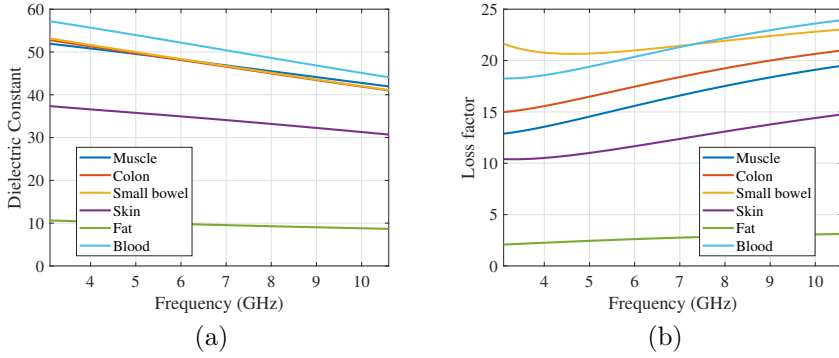
Figure 2.1: Electromagnetic properties of human tissues. Reference values given by Gabriel in [30]

human body (implantable or ingestible) are considered in-body. The antennas that are placed outside the human body but in direct contact with the skin or the clothes are on-body, while the antennas located outside the human body but not in contact with the skin or the clothes are considered off-body. This last category is usually referred to the external medical devices. Fig. 2.2 and Table 2.1 summarize the different scenarios.
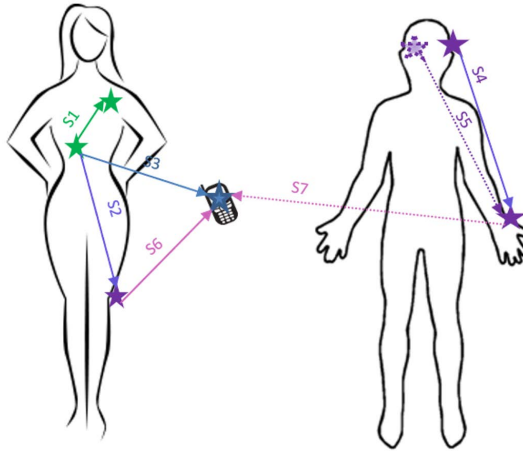
Figure 2.2: Scenarios defined for the WBANs

Table 2.1: Scenarios in WBANs

Scenario	Description	Frequency band
S1	In-body to in-body (IB2IB)	MICS
S2	In-body to on-body (IB2OB)	MICS
S3	In-body to off-body (IB2OFF)	MICS
S4	On-body to on-body (LoS) (OB2OB)	ISM or UWB
S5	On-body to on-body (NLoS)(OB2OB)	ISM or UWB
S6	On-body to off-body (LoS)(OB2OFF)	ISM or UWB
S7	On-body to off-body (NLoS)(OB2OFF)	ISM or UWB

In Table 2.1 only the main frequency bands are shown. The standard [27] defines more frequency bands used mainly for the on-body applications like the ISM band from 902 to 928 MHz among others. However, they are not used as often as the MICS, ISM (2.45 GHz), and the UWB frequency band, thus they are not included in the Table 2.1. Each scenario, has different channel models, which depend on the frequency, the scenario, and sometimes the location in within that scenario (line-of-sight (LoS) or non-line-of-sight (NLoS)).

2.1.3   Channel Characterization in WBANs

The losses due to the channel in any propagation environment are an unavoidable problem, which can be overcome with the correct knowledge of the signal's behavior. WBANs are not an exception and the proper characterization of the channel is a must. Usually the channel models are defined by the path loss models, which refers to the losses due to the propagation path. In WBANs the effect of the antennas cannot be completely isolated from the losses of the channel. So, according to the International Telecommunication Union, Radiocommunication Sector (ITU-R) [34] the annotation of SL is chosen as the ratio between the transmitting and receiving power including losses of the transmitting and receiving antennas and the path loss, usually expressed in decibels (dB). Frequently, the SL can be indiscriminately called as path loss (PL) since they are mainly the same concept in WBANs because of the irremovable antenna effect.

$$SL(dB) = 10 \log (p_t/p_r) = P_t(dB) - P_r(dB) \qquad (2.2)$$

Eq. 2.2 describes the ratio between the transmitting (Tx) (P_t) and receiving (Rx) (P_r) power. This is the theoretical way of extracting the SL values, how-

ever this has to be mathematically modeled so it can be used for the scientific community without having to measure the channel every time. The channel model usually used for the propagation in free-space has a logarithmic form which is widely known in the scientific community Eq. 2.3.

$$SL(dB) = SL_0(dB) + 10n \log (d/d_0) + N(\mu, \sigma) \tag{2.3}$$

in Eq. 2.3, d is the distance, the $SL_0(dB)$ is the SL reference value for the reference distance d_0, n is the system loss exponent, which mainly defines the behavior of the model. Finally, the $N(\mu, \sigma)$ is the scattering parameter of the model, which follows a log-normal distribution with mean, μ and variance σ, where μ is usually 0. Moreover, the logarithmic model is used to define the channel losses in WBANs. The aforementioned standard [27] is extended with the report described in [35], where each scenario has a channel model which defines it. In Table 2.2 the different parameters for some scenarios are described. One can see in the Table 2.2 that some scenarios such as S3, S6 and S7 are not represented, this is because S6 and S7 do not have a standardized model but some values according the position of the Tx and Rx antenna. Moreover, the S3 is defined a combination of S2 and S6 or S7, which as said are a set of values according to the position of the antennas.

Table 2.2: Channel models in WBANs

Scena-rio	Freq. Band	Channel model	Location	PL_0 (dB)	n	σ (dB)
S1	MICS	CM1	Deep Tissue	35.04	6.26	8.18
			Near Surface	40.94	4.99	9.05
S2		CM2	Deep Tissue	47.14	4.26	7.85
			Near Surface	49.81	4.22	6.81
S4, S5	ISM	CM3*	Hospital Room	36.1	6.6	3.8
			Anechoic Chamber	-16.8	29.3	6.89
	UWB		Hospital Room	3.38	19.2	4.4
			Anechoic Chamber	-31.4	34.1	4.85

*The PL model used is given by $PL(dB) = PL_0 + n log_{10}(d) + N(\mu, \sigma)$ The reference distance (d_0) is considered 50 mm

From the Table 2.2 it is possible to distinguish that the PL models defined in WBANs are still an open issue because it strictly depends on the location of the antennas (surface or deep tissue) and also the environment of the measurements (hospital or anechoic chamber). Moreover, the methodology used to perform

(a)   (b)   (c)
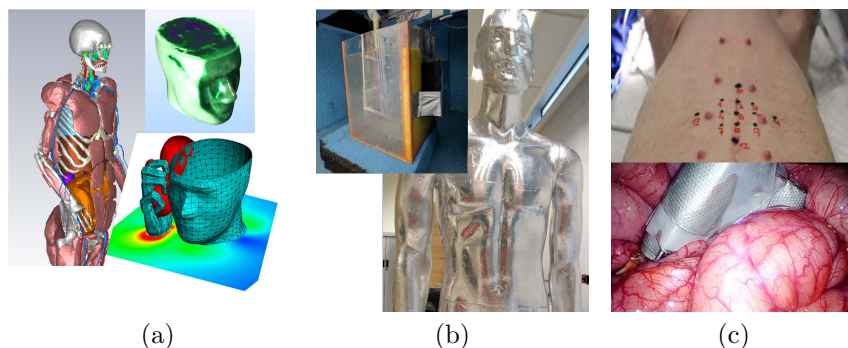
Figure 2.3: Examples of the three methodologies. (a) Software simulations (CST MWS, COMSOL Multiphysics, and Altair Feko), (b) EM phantom and human model phantom, (c) *in vivo* experiments in pigs

the channel characterization changes according to the scenario under interest. For external measurements (on-body to on-body (OB2OB) or off-body to off-body (OB2OFF)), the channel can be easily measured using human subjects due to the non-invasive character that the experiment has. Nevertheless, for in-body measurements the methodology to measure the channel increases its complexity. Invasive experiments on living humans are strictly forbidden due to ethical restrictions [36]. Therefore, the channel has to be characterized by means of software simulations, phantom measurements, and *in vivo* animal experiments. In Fig. 2.3 some examples of these three methodologies for WBANs are shown.

Software simulations

Electromagnetic software simulations are high computational electromagnetic (CEM) software that use different numerical methods to solve Maxwell's equations. They are used to calculate different parameters e.g., Specific Absorption Rate (SAR), S-parameters, antenna impedance, gain, far field. Some of the advantages that simulations present over experimental measurements are the feasibility, the simplicity, and economic resources. Extending this, to design and run simulations only a powerful computer and a commercial software license are required. Moreover, many different software are currently available in the market, e.g., CST MWS, HFSS, Feko Altair, COMSOL Multiphysics. Another positive point for simulations is the total control of the variables and conditions of the simulations, which may help to understand the behavior of some characteristics, i.e., the size of the design or the location of the anten-

nas. Contrarily, the computational time and complexity of the model can lead to large time of computation and memory capacity limitations. Disadvantageously, even though the simulations are getting closer to the real conditions of the human body, there are still some parameters that simulations cannot recreate like the blood flow, the respiration, or the internal movements that living bodies have. In Fig. 2.3 (a) some human models are shown. Concretely, the Hugo model of the CST and two head models used for SAR computation of the Feko Altair and the COMSOL Multiphysics software.

Mainly, the computational methods are divided in time- and frequency-domain. Inside these categories different computational methods are found, Finite-Differences in Time-Domain (FDTD) and Finite Integration Technique (FIT) for time-domain and Method of Moments (MoM) and Finite Element Method (FEM) for frequency-domain. Usually the time-domain methods are robust, flexible, and more suitable for wide frequency range simulations but they require large memory resources and close boundary conditions. Frequency-domain methods try to replace the problem of integrating different equations by the equivalent functions. However they are commonly more computationally expensive [37]. In [38] a summary of each method is detailed, here the main characteristics of each computational method are described. FDTD is the most used for EM propagation through the human body, it is a simple algorithm that divides the structures in small homogeneous cells. FIT is an evolution of FDTD, it allows to have heterogeneous cells, making it more suitable for complex geometries. FEM also divide the structure in small elements that can be rectangular or triangular shaped, it is appropriate for complex structures at low frequencies due to the memory complexity constraints. Finally, MoM solves the Maxwell's equations in their integral form, it is used for SAR or metallic structures, it does not perform well with large or complex structures.

Intuitively, the use of one or another method is conditioned by the problem to solve. Open boundary conditions are mainly used for radiation or scattering problems, while absorption and EM radiation by biological tissues are close-boundary models. There are more computational methods to solve the Maxwell's equations like the transmission line matrix method, uniform theory of diffraction, or hybrid methods. Nevertheless, these are out of the scope of this research for further information please refer to [37]. A summary of the most common methodologies and software are listed in Table 2.3.

From the Table 2.3 one can see that multiple software employ similar methods to solve the Maxwell's equations. Other important characteristic to take into account when choosing one software is the human models that the software provides. CST MWS provides a full set of voxel human and animal models [39, 40]. Altair Feko [41] and Ansys HFSS [42] also provide human models. Nevertheless, they are less complete than the ones provided by CST. It is not

Table 2.3: Numerical methods and software application

Method	Commercial software	Model design	Solver Domain
FIT	CST MWS	Close boundary conditions	Time domain
FDTD	FEKO		
FEM	Ansys HFSS	Close boundary conditions	Frequency Domain
	CST MWS		
	FEKO		
	COMSOL		
MoM	CST MWS	Open Boundary conditions	Integral Equations
	Ansys HFSS		
	FEKO		

as usual but also possible to find some self-developed software to resolve the Maxwell's equations and design human models as reported in [43].

Phantom measurements

Phantoms are defined as a replica of some human characteristics, e.g., shape, texture, density, weight, EM properties. Phantoms are mainly used to perform experimental measurements (also called *in vitro* testing) in laboratory when they cannot be conducted in living bodies. Some common examples are the manikins for car crash tests or odontologist students, in which the shape, weight and teeth of the human bodies are replicated (Fig. 2.3 (b)). For WBANs the parameters to mimic are other aspects of humans such as the EM properties of the tissues. For any kind of body communications (in-, on- and off-body) the EM properties have high impact in the RF communication link. In Fig 2.3 (b) it is also shown phantoms that are chemical mixtures that properly mimic the EM properties of the human tissues.

For channel characterization purposes, experimental measurements are an unavoidable step. Phantom measurements have several advantages in front of software simulations. Firstly, the more realistic conditions that phantom measurements have and the larger quantity of sample points in comparison with simulations. One sample point in simulations can take several hours to compute depending on the complexity of the model, while measurements with

an spectrum analyzer or Vector Network Analyzer (VNA) take only several seconds. The feasibility of the phantom measurements is also higher than *in vivo* experiments, only a laboratory and equipment is required and not a dedicated team and surgical facilities. These experiments are a vital part of the channel measurements because they allow to perform large set of values and control some of the variables that occur in measurements, such as the displacement between antennas, the distance between them or the quantity and amount of tissues between antennas.

Previous phantom measurements in literature were conducted to measure in only one frequency point or narrow band [44, 45] or as seen in [20, 46] in UWB frequency bands but with a poor approximation of the properties. Others [39] have used as phantoms tissues from dead animals, however the EM properties of the living bodies mismatch for *in vivo* and *ex vivo*. Luckily, the accuracy of ultra-wideband phantom has increased in the last years thanks to a group of researchers in the Universitat Politècnica de València (UPV) [47, 48], which have developed a new formulation based in acetonitrile to mimic the EM properties of the human tissues in an ultra-large frequency band (0.5 to 18 GHz).

In vivo measurements

In vivo measurements is the methodology that has the closest conditions compared with the real application. When it comes to channel characterization, the on-body measurements can easily be performed in human beings [25, 49, 50], attaching the antennas to the body and measuring the losses with no human pain or harm. However, for implanted devices, human experimentation must be considered as the ultimate stage of the study due to the high risk it has, as it is regulated by the Declaration of Helsinki [51].

Alternatively, animal experimentation is used for the characterization of in-body channels. The selection of the animal will depend on the scenario of application; rats and mice [52] are by far the most used animals mainly for genetic disorders or cancer studies [53]. Pigs are mainly used for gastrointestinal (Fig. 2.3 (c)) and cardiac measurements [54–57]; other mammals like dogs are also employed for cardiac scenarios [58]. There are many positions for or against the experimentation in animals, like if they should have the same rights as humans or if humans are above animals and they can be used indistinctly. Currently, there is a middle point, and animal experimentation has some ethics and moral laws to follow depending on the location of the experiment [36, 59]. The relation between the pain induced to the animal and the benefit it will give to humans is the primary balance to perform or not experiments in living beings, popularly named as the cost-benefit balance. Moreover, there

are three main rules generally followed by all the regulations, which are meant to minimize the use of animals in research. These are named as the triple R principles: Replace, Reduce, Refine.

- **Replace** the animal models with other *in vitro* studies, phantoms, numerical methods, which will give the same result as the animal experiment.

- **Reduce** the number of subjects to the minimum justifiable.

- **Refine** or eliminate the pain, harm or damage of living beings.

Following these principles, the channel characterization is only used in animals, when there is no other option. As explained in the previous sections, software simulations and phantoms measurements are becoming, but they are not yet as efficient as *in vivo* measurements to characterize the channel by themselves. The measurement conditions such as the body temperature, the movement of internal fluids, and the tissues that form the channel make this methodology the most reliable for channel characterization. On the contrary, the high price of the procedure because of the specific conditions of having surgical facilities, medical doctors, and specific technicians. Moreover, the uncontrollable conditions of the media and the multiple variables that appear in *in vivo* experiments make this procedure risky in terms of money, time and resources, e.g., the premature decease of the animal; the rupture of vessels, devices, and cables; and the high movement of the fluids, which may lead in a significant movement of the antenna.

2.2 Summary of proposed propagation channel models in the literature

According with the sections above, the proper characterization of the channel has to be performed by means of software simulations, phantom, and *in vivo* measurements. Doing this, each methodology supplies the lack of the others. Software simulations allow to control all the variables and environment but the conditions are unreal. Phantom measurements have more realistic conditions and can precisely control some of the variables. *In vivo* measurements have the most realistic conditions but the environment and some variables are unpredictable. In the previous section a rough overview of different proposed models has been given, now, in Table 2.4 a summary of the path loss models in similar conditions (frequency band, scenario of interest) as the case of study of this dissertation is listed.

The Table 2.4 is divided in the following order: Firstly, the general scenario and the methodology employed for the characterization of the channel, then the frequency and distance range for which the model is valid, the scenario of application, which is mainly the abdominal or gastrointestinal area. Finally, the mathematical expression used to characterize the channel and the reference are given.

Numerical simulations are the most common way to characterize the channel due to the simplicity they provide. Different software can be used for this purpose. CST is used in [60], where a human model is embedded to use the FIT solver. They use a linear mathematical model to characterize the channel as given in Eq. 2.4, where α is the path loss exponent and μ and σ are the mean and the variance of the normal distribution that defines the scattering due to the heterogeneous environment inside the human body (please note that the terms μ and σ are no longer related to the EM properties of the human tissue).

$$SL(dB) = SL_0(dB) + \alpha(d/d_0) + N(\mu, \sigma) \tag{2.4}$$

In [61] numerical simulations using FIT with the CST were performed to compute the PL model as a function of depth and the calculation of the channel impulse response. In this work, the mathematical model used to characterize the attenuation is not given by the logarithmic model but with an exponential model given in Eq. 2.5. Where β and λ are the fitting constant and the path loss exponent respectively. As well as with the logarithmic model (Eq. 2.3) μ ans σ are the mean and the variance of the normal distributions due to the heterogeneity of the human model. In [61] only simulations have been performed and the model starts at very for short distances of 1 mm, which are impossible to achieve for IB2OB communications.

$$SL(dB) = SL_0(dB) + \beta(d/d_0)^{\lambda} + N(\mu, \sigma) \tag{2.5}$$

In [62] also numerical simulations using FDTD with with XFDTD^{TM} from REMCOM, Inc. are performed. The mathematical model used to characterize the channel is a logarithmic component as in Eq. 2.3, which in this case it is frequency and distance dependent. Moreover, in contrary to the standard literature models they use as scattering component a Weibull distribution. They examine the channel for specific subbands (500 MHz) in the range of 3.1 to 6 GHz, only in simulations and without a double validation with experimental measurements. Finally, they do not propose a final model but some considerations of which subband to use regarding the distance between antennas.

[20] and [63] are studies performed by the same group, which have some similarities but interesting differences. They both use numerical simulations with FDTD method to solve the Maxwell's equations, they also use the same

frequency band of study 3.4 to 4.8 GHz, with multiple receivers in the abdom-
inal region, simulating the case of study of an endoscopic capsule. In [20], they
propose different models for each 200 MHz subbands but then they perform all
the study averaging the values obtained. The main difference between them
is the distance range, which goes from 5 to 9 cm and 2 to 24 cm leading to
different values which disagree with themselves. The study performed in [20] is
the last proposed model, so it is most likely to be considered as the valid one.

The work performed in [56] considers two scenarios of interest the IB2IB and
the IB2OB. In both cases the methodology used to characterize the channel is
based on phantoms measurements for the frequency range between 3.1 to 8.5
GHz. The phantoms used are matched for the whole UWB frequency band,
and the setup is dedicated for the purpose of IB2OB measurements. For the
IB2OB measurements the path loss model has a logarithmic form and a distance
range of 5.5 to 20 cm. For IB2IB the model used to model the channel is not
logarithmic but lineal as given in Eq. 2.4. Nevertheless, these results are not
validated with simulations or with *in vivo* measurements. Being difficult to
check if the model is valid or not.

In vivo measurements were performed in [55, 64] both experiments were
performed in pigs. As well as in [61], the frequency band chosen for the charac-
terization of the channel is 1 to 6 GHz, which is an extremely large bandwidth
for the purpose of in-body communications. Moreover in [64] the results are not
validated with phantoms or simulations, which cannot validate the measure-
ments performed. It is different in [55] where the measurements were performed
for a frequency band from 3.4 to 4.8 GHz. This work can be considered the
continuation of that started in [20] and shows agreements between both mea-
surements. Nevertheless, the phantom experiments performed in that work
do not propose a model, they are only used to calculate the matching of the
antennas.

There are some works that use different methodologies to model the sys-
tem loss, in [39] numerical simulations and experimental measurements with
phantoms are proposed. CST MWS is used to design the model and run the
simulations, whereas tissues such as muscle, intestines, fat, and skin are used.
In this work, nonetheless, they do not distinguish between the IB2IB and the
IB2OB environment and propose an exponential model Eq. 2.5. Moreover they
use real tissues from a dead animal, but *ex vivo* [65] and *in vivo* tissues are
demonstrated to have different EM properties.

Continuing with the use of two different methodologies, in [54] they per-
formed experimental measurements in both, phantom and a living animal. The
phantom used for this experiments is an aqueous phantom that properly mimic
the EM properties of the muscle. They performed both experiments using the
same antennas and trying to set the environment conditions as similar as pos-

sible. Nevertheless, the amount of data points obtained was not significant and the linear models presented Eq. 2.4 are not noteworthy.

Moreover, many of the works described in the Table 2.4 did not have as a purpose to model the channel but other aims such as, SAR evaluation [39], correlation of the channel [56] or calculation of the Bit Error Rate (BER) [20, 55]. Thence, it is necessary to dedicate an extensive work to characterize the channel by the means of the three aforementioned methodologies. In this dissertation the channel is characterized using numerical simulations, aqueous phantom measurements, and *in vivo* measurements.

Table 2.4: UWB Path Loss models reported in literaure

Scenario	Methodology of Analysis	Frequency Range (GHz)	Distance Range (cm)	Scenario of Application	Path Loss Model	Ref
IB2IB	Experimental Measurements	3.1 - 8.5	$3 \leq d \leq 8$	Muscle Tissue	Linear	[56]
IB2OB	Numerical Simulations	1 - 6	$1 \leq d \leq 15$	Abdominal Region	Linear	[60]
			$0.1 \leq d \leq 12$	Chest Region	Power	[61]
		3.1 - 6	$4 \leq d \leq 24$	Chest Region	Logarithmic	[62]
		3.4 - 4.8	$5 \leq d \leq 9$	Abdominal Region	Logarithmic	[20]
			$2 \leq d \leq 24$			[63]
	Numerical Simulations & Experimental Measurements	3.5 - 4.5	$0 \leq d \leq 9$	Abdominal Region	Power	[39]
	Experimental Measurements	3.1 - 8.5	$5.5 \leq d \leq 20$	Muscle Tissue	Logarithmic	[56]
	Experimental & *in vivo* measurements	3.1 - 5	$3 \leq d \leq 11$	Muscle Tissue & Abdominal Region	Linear	[54]
	In vivo measurements	1 - 6	$5 \leq d \leq 16$	Abdominal Region	Logarithmic	[64]
		3.4 - 4.8	$3 \leq d \leq 12$			[55]

Chapter 3

System Description

This chapter describes the elements and setups of the performed measurements in laboratory, in vivo, and numerical simulations

3.1   Measurements description

As discussed in Section 1.3 the experiments carried out to characterize the channel are phantom-based laboratory measurements and living experiments in animals. The common elements that can be found in both methodologies are the use of antennas designed for the purpose of body communications, devices that allow the spatial position of the elements, and a device to measure the power of the received signal (VNA or spectrum analyzer).

Antennas

The antennas used for body communications have different characteristics compared with the free-space antennas. Firstly, they have size constraints, because they are limited to few centimeters in length and width and secondly, material constraints because of the need for biocompatible materials since they are located inside the human body. Moreover, the tissues surrounding the antenna have different EM properties than the free-space, which highly affect some characteristics of the antenna like the electrical dimensions [66]. To minimize this tissue effect, in-body antennas are usually coated with a biocompatible material, having this material high-permittivity and low-losses properties.

Besides, due to the particularities of the UWB in-body channel that merges the effects of the antenna and the channel, it is crucial to know what is the final application for which the antenna will be employed. Multiple antennas

have been proposed for in-body communications [2] and they highly depend on the final application of use. Ingestible antennas (WCE type antennas) are mainly omnidirectional antennas due to the unpredictable behavior that the device can experience when it is inside the human body traveling along the gastrointestinal tract [67, 68]. On the other hand, for implantable antennas, which are supposed to be always located at the same position inside the body, directional antennas are more appropriate for this communication link [69].

Following these requirements, eight antennas have been chosen for the experiments in this dissertation and have been listed on Table 3.1 and 3.2. (The column *Name* refers to how the antennas will be called all through this dissertation, on tables, graphs and the text itself).

The first two antennas (Fig. 3.1 and Fig. 3.2) were designed to be located inside the human body. The first antenna (*In 1*, Fig. 3.1, [70]) is an UWB planar monopole with CPW-feeding and circular patch. It was designed to serve as ingestible antenna due its omnidirectional pattern and its size (23 mm × 20 mm). This antenna will be the most used for almost all the experiments. The second in-body antenna (*In 2*, Fig. 3.2, [71]) is an elliptical planar antenna of 5.85 mm in diameter, with Rogers TMM10 ($\epsilon_r = 10.2$) designed for in-body measurements at the low-UWB frequency band for the gastrointestinal area with directional pattern.
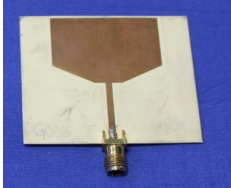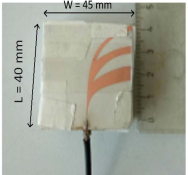
There are five different antennas that were used for on-body communications at the UWB frequency band. The first on-body antenna (*On 1*, Fig. 3.3, [49]) is a generic planar patch antenna (45 mm × 40 mm), which was designed for the purpose of on-body communications. It showed an omnidirectional pattern and also good performance for IB2OB and IB2OFF communications, this antenna will be the most used among all the experiments explained in this research. The UWB antipodal Vivaldi antenna (*Vivaldi*, Fig. 3.4, [72]) was fabricated on a flexible substrate of Rogers RO 3010 with $\epsilon_r = 10.2$ and thickness of 0.255 mm. As seen in the Fig. 3.4, the dimensions of the antenna are 40 mm × 45 mm × 20 mm in length, width, and thickness.

The next two antennas (*On 2* and *On 3*, Fig. 3.5 and Fig. 3.6, [50]) were designed for IB2OB communications being then completely matched for the different layers of the human body (skin, fat, muscle, fat, tissue). This means that they cannot be used on phantom but only for real *in vivo* experiments. On 2 antenna is an UWB slotted patch on-body antenna that has a metallic plane on the back, which acts as a reflector. This increases the size of the antenna (50 mm× 50 mm × 12 mm) but it also creates a directional antenna. On the other hand, On 3 antenna was designed to be a copy of the previously explained In 1. As seen this is also a CPW feeding with circular patch antenna with omnidirectional pattern.

Table 3.1: Antennas used for the characterization of the in-body channel (I)

Figure	Size (mm)	Pattern	Scena- rio	Freq. Band	Na- me
Figure 3.1: In-body CPW feeding antenna	20×23	Omni- directional	in-body	[3.1,8.5] GHz	In 1
Figure 3.2: In-body el- liptical planar antenna	∅=5.85	Directional	in-body	[3.1,5.1] GHz	In 2
Figure 3.3: On-body planar patch antenna	50×44	Omni- directional	on-body & off-body	[3.1,8.5] GHz	On 1
Figure 3.4: On-body UWB Antipodal Vi- valdi antenna	45×40 × 20	Directional	on-body	[3.1,6] GHz	Vivaldi

Table 3.2: Antennas used for the characterization of the in-body channel (II)

Figure	Size (mm)	Pattern	Scena-rio	Freq. Band	Na-me
Figure 3.5: On-body slotted patch antenna	50×50 ×12	Directional	on-body	[3.1,6.1] GHz	On 2
Figure 3.6: On-body CPW feeding antenna	40×45	Omni-directional	on-body	[3.1,8.5] GHz	On 3
Figure 3.7: On-body planar patch antenna	38×32	Quasi omni-directional	on-body	[3.1,5.1] GHz	On 4
Figure 3.8: Heli-cal invert-F dipole antenna	∅=16 h=26	Omni-directional	in-body & on-body	[46,68] MHz	Helical

The last antenna used in this dissertation was an Helical invert-F dipole antenna (*Helical*, Fig. 3.8, [73]). This antenna is designed to be matched at low frequencies (46 to 68 MHz). Nevertheless, the wavelength of the signal at these frequencies is approximately of 10 m. To reduce this wavelength a magnetic material was added to the design, having three layers of copper foil-magnetic sheet-copper foil, and a very small size of 26 mm in height and 16 mm diameter. This antenna works either inside and outside the human body, being the inner antenna coated with silicone. Besides, the in-body antenna was attached to an FPGA based transmitter, so the antenna is now completely wireless and can be inserted inside the animal without any cables. The counterpart is the relative large size of the transmitter which is inserted inside a plastic box of 4 cm × 4 cm × 2 cm, which has to be minimized for real applications.

3D spatial positioning systems

For all the experiments used on this research the exact location of the transmitting and receiving antennas was a required parameter for the post-processing of the data. The most used along the experiments (in both phantom and *in vivo*) was a 3D magnetic tracker from *Ascension Technology Corporation* (*trakStar* with a *Mid-Range Transmitter*, Fig. 3.9). The Electronic Unit (Fig. 3.9 (a)) is the driver that synchronizes all the components and send the information to the laptop to which is connected. Then, the mechanism is based on the creation of a magnetic field of 44 cm × 56 cm × 60 cm in X, Y, and Z by the Mid-range transmitter (Fig. 3.9 (b)) reaching all the space under interest and the spatial position of the 6DOF Sensors (Fig. 3.9 (c)) in X, Y, and Z

(a)　　　　　　　(b)　　　　　　　(c)
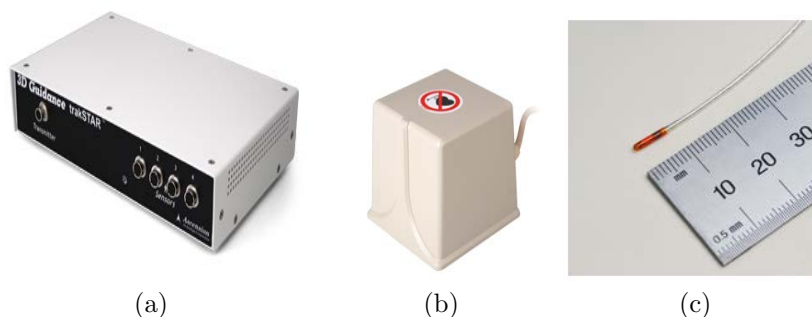
Figure 3.9: 3D trakstar magnetic tracker from *Ascension Technology Corporation* [74](a) Electronic Unit, driver, (b) Mid-Range Transmitter, (c) 6DOF Sensors Model 130

| (a) | (b) | (c) |
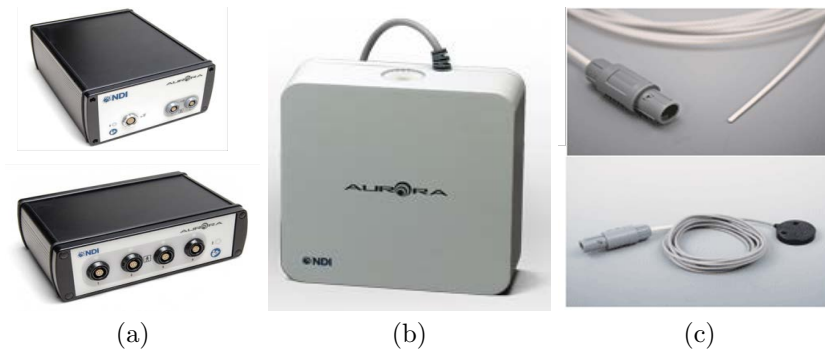
Figure 3.10: 3D electromagnetic *Aurora* tracker from *Northern Digital* [75] (a)System Control Unit (SCU) (top) and Sensor Interface Unit (SIU) (bottom), (b)Planar Field Generator, (c)Aurora 6DOF Flex Tube (top), Type 2 and Aurora 6DOF Reference (bottom)

with respect to the center of the magnetic transmitter is computed. For our purposes, the magnetic sensors are attached to the center of each antenna in the measurements, so knowing the XYZ coordinates, it is possible to calculate the Euclidean distance between antennas.

The second positioning system used in the measurements was employed only for *in vivo* measurements performed for the characterization of low UWB signals. The *Aurora tracking system* from *Northern Digital* Fig. 3.10 was the chosen one for these measurements. On contrary to the previous tracker, now, there are two different sensors, one that serves as a reference Fig. 3.10 (c) (bottom) the Aurora 6DOF References. The second one Fig. 3.10 (c) (top), whose position is computed with respect to the first. Moreover, the sensors are connected to the Sensor Interface Unit (SIU), which is connected to the System Control Unit (SCU). The SCU is the driver that controls all the external elements of the positioning system. In this case, the EM transmitter (Fig. 3.10 (b)) generates a 50 cm × 50 cm × 50 cm field in the front vicinity of the transmitter.

3.1.1 Laboratory Measurements

As mentioned in Section 2.1.3, phantom-based measurements in laboratory are essential for the characterization of the channel. Although currently, this kind of measurements themselves need an extended validation with *in vivo* measurements, they provide fast and accurate measurements in a controllable environment. In the future, the trend to perform experiments with animals will
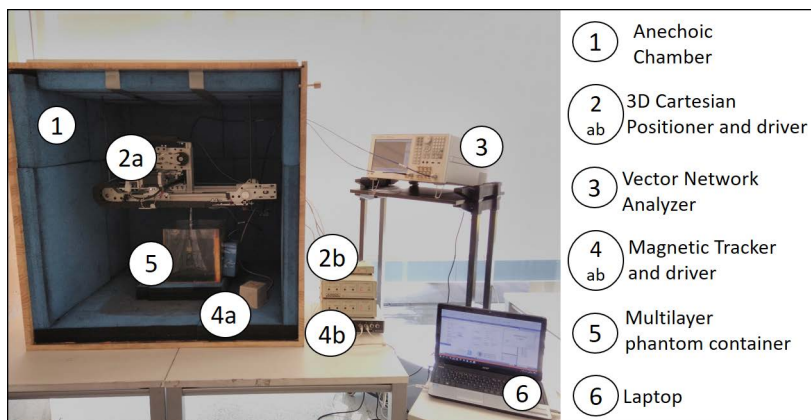
Figure 3.11: Phantom measurement setup

decrease for moral and ethical issues becoming phantoms an essential way to characterize the channel. For that, the need to improve phantom measurements in laboratory is growing, for example, enhancing the quality of the phantoms or designing laboratory testbeds dedicated for the purpose of in-body measurements in phantoms.

Phantom Measurement System

Concerning the measurement scenario, phantom experiments are usually measured in research laboratories, which may be not exclusively dedicated for that purposes. This leads to some inaccuracies and undesired effects due to the possible reflections or unexpected contributions of the environment. Therefore, in order to avoid all these issues and to have more accurate phantom measurements a dedicated measurement testbed was built. It was designed for the purpose of IB2OB measurements but it is also applicable to any kind of in-body communications (IB2IB and IB2OFF).

The developed testbed is shown in Fig. 3.11 and the main components are: a VNA (*Agilent Technologies E5072A*), a laptop, and a small anechoic chamber. Inside the small anechoic chamber, a 3D spatial positioner, a phantom container, and a magnetic tracker are placed. Moreover, the testbed is software controlled by a laptop so all the elements of the setup are connected to it and the process is automatized.

Going into details, the anechoic chamber Fig. 3.11 element 1 is used to minimize the undesired contributions at the receiver due to the surrounding

environment in the laboratory, as in [76], where OB2OB measurements are performed inside an anechoic chamber. It has an internal volume of 1 m^3 and the structure is built with pine wood of 22 mm width. The interior of the chamber is coated with aluminum foil of 13 μm width, this coating creates a sort of Faraday Cage for the frequencies under study (3.1 - 10.6 GHz), isolating the inside of the cage from the outside. Then, the aluminum foil is re-covered with a flat absorber (*MVG-AEMI, AEL 2.25*). These flat laminated absorbers are made from 3 open cell polyurethane foam layers of 1.9 cm each. They are designed to attenuate at least 20 dB for frequencies above 1.3 GHz.

Besides, for in-body scenarios, the separation distance between antennas is in the range of a few centimeters. Therefore, an imprecise estimation of the antenna location caused by their manual placement could lead to large relative errors. To overcome this issue, a 3D Cartesian positioner (*Arrick Robotics tGlide 3-axis positioner*) is placed inside the anechoic chamber (Fig. 3.11, element 2a). This positioner has a 1 mm precision along the X, Y and Z axis and 30 cm × 30 cm × 10 cm movement range. Then one of the antennas used for the measurements is attached to the positioner so it can be accurately moved enhancing the precision of the measurements. Furthermore, this positioner is connected to a driver, which is located outside the chamber through an electrical connection (Fig. 3.11, element 2b). The driver is then connected to the laptop that has a dedicated software to control the movement of the positioner. In addition, to the accuracy provided by the antenna positioning system, the spatial position of each antenna is given by a 3D magnetic tracker from *Ascension Technology Corporation* (Fig. 3.1 and Fig. 3.11, element 4).

Finally, the antennas are connected to the the VNA Fig. 3.11 element 5, which calculates the S-Parameters of the system. Usually the transmitting antenna is connected to the port 1 of the VNA while the receiving antenna to the port 2. Then the reflexion coefficient of the system given by S$_{11}$ and S$_{22}$ assures that the antennas are matched for the given measurements. To evaluate the channel, multiple measurements of the S$_{21}$ are calculated for different positions with the help of the positioner and the magnetic tracker.

Phantom characteristics

Phantoms are developed to mimic some characteristics of the human body, they can mimic the shape, weight, color, and texture of the tissues. Nevertheless, in this research phantoms are considered as aqueous mixtures that accurately mimic the EM properties of the human tissues for a desired frequency band. Salt and sugar solutions are commonly used as EM phantoms. These phantoms nonetheless, only provide accurate values for narrow bands [44, 45]. For larger bands, UWB phantoms with sugar or salt are not accurate, for example in [46,
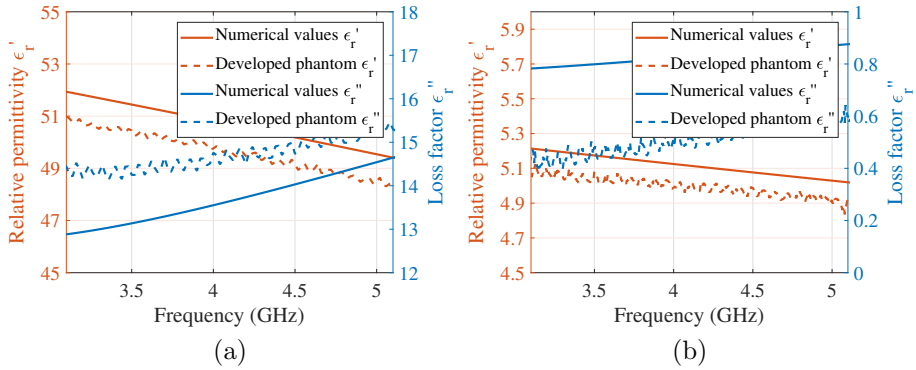
Figure 3.12: Relative permittivity and loss factor of human tissues and developed phantoms used for laboratory measurements (a) Muscle phantom (b) Fat phantom

55] phantoms are used, but the composition and performance of the phantoms are not described nor shown.

In this research, a novel formula for phantoms is used. These phantoms are now based on acetonitrile along with other chemical components [47, 48], and they mimic the EM properties of the human tissues for a large frequency band i.e., [0.5, 18] GHz. This represents a significant improvement in phantom measurements because now it is possible to perform highly accurate measurements for UWB signals.

In this dissertation the main scenario under interest is the gastrointestinal scenario, where some of the main tissues involved are muscle, fat, colon, small bowel, and skin. According to [30] and Fig. 2.1, colon, muscle, and small bowel have very similar EM properties, thence they are considered as interchangeable tissues. To standardize to the literature, where the main tissue of study is the muscle, this one is the chosen tissue to mimic and to perform the measurements.

In Fig. 3.12 muscle and fat phantom are shown. Concretely, Fig. 3.12 (a) plots the relative permittivity and loss factor of the muscle, which is composed with acetonitrile (54.98%) and NaCL (1.07%) [47]. Fig. 3.12 (b) shows the fat phantom used, which is a simplified version of the original proposed in [32]. This version achieves also a good approximation of the numerical values reported in [30] and it can be defined as an emulsion of 86% of oil in water, in which 1% of TX-100 was used as sufractant. Moreover, from the Fig. 3.12 the good performance of the phantoms is demonstrated, achieving for the muscle case a 1% of deviation with the numerical values, whereas 4% and 12% of deviation are reached for the relative permittivity and loss factor in the fat case.
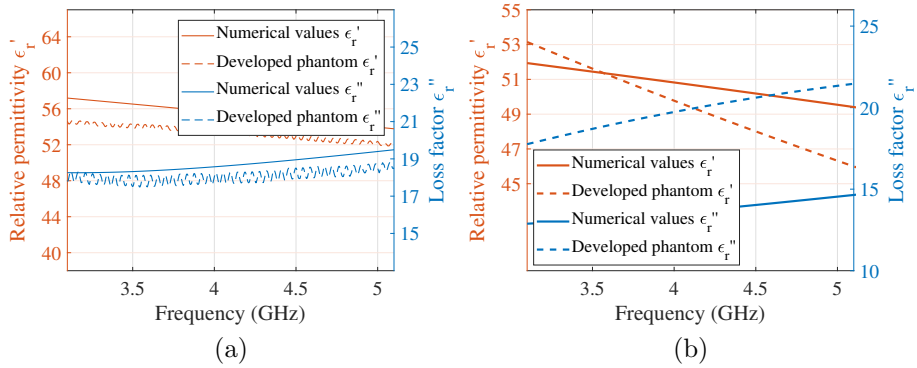
Figure 3.13: Relative permittivity and loss factor of human tissues and developed phantoms used for laboratory measurements (a) Blood phantom (b) Sugar UWB phantom

However, different experiments were performed, in which the use of other kind of phantoms was necessary. This dissertation was focused on the GI area of the human body but some experiments were performed mimicking the cardiac scenario. In those cases, the blood has now a major role on the characterization of the channel. In Fig. 3.13 (a) the developed blood phantom can be seen [47]. From the reference values given in [30], it shows a distortion of only 5.2% to 1.8% for the permittivity and 2.25% to 3.23% for the loss factor. As with the previous tissues i.e., muscle and fat phantom, the EM properties of the developed phantom show high level of agreement between theoretical tissue and the experimental phantoms.

On the other hand, the phantoms developed with acetonitrile are expensive and difficult to handle due to their toxicity and corrosive behaviour. Therefore, for some experiments a cheaper, easier to handle, and develop phantom was used. The phantom is shown in Fig. 3.13 (b) and considering the muscle as the reference tissue [30] it can be seen how the relative permittivity varies from 0% (both lines have an intersection point at 3.6 GHz) to 7% and from 37% to 46% for the loss factor. These EM properties are not as accurate as the previous phantoms used but for the purpose of that experiment (explained later in section 4.1.1) it was a good approximation.

Phantom containers

The phantoms described in Fig. 3.12 are liquid solutions that need to be placed in a recipient. This is a major disadvantage of liquid phantoms among other kind of phantoms such as semisolid or solid phantoms (unfortunately, for the
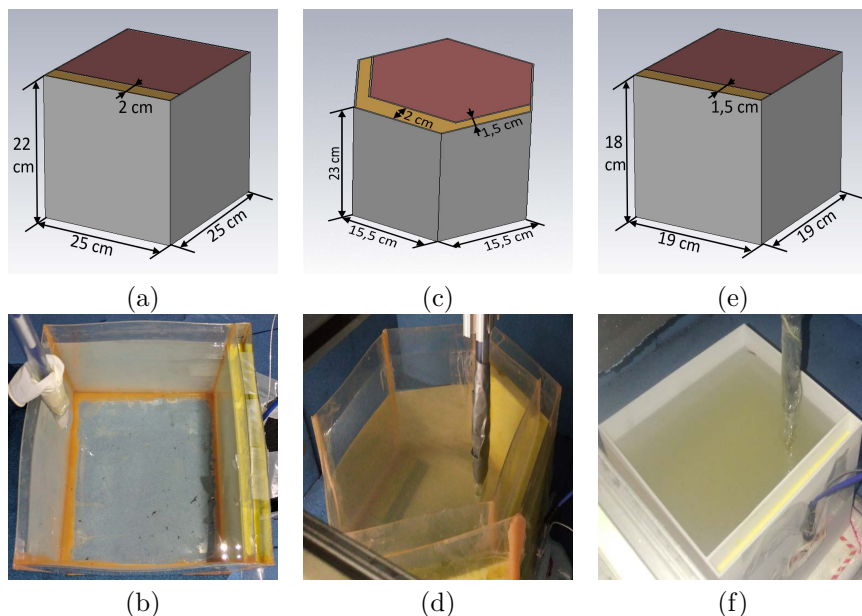
Figure 3.14: Phantom containers used for the laboratory experiments. (a) Large-square container, simulation (b) large-square container. (c) Hexagonal container, simulation (d) hexagonal container. (e) Small-squared container, simulation (f) small-squared container

purpose of in-body channel characterization there are no solid or semisolid phantoms developed). Moreover, liquid phantoms are easier to work with for in-body communications since the antennas placed inside can be freely moved. The literature is full of references of phantom measurements with liquid phantoms. [41, 44, 46, 56]. However, these studies only consider one layer of tissue between the antennas. This is not a trivial issue, the EM wave suffers from reflections and refractions for each medium change. In this dissertation a bilayer and a trilayer phantom container have been chosen to perform the laboratory measurements, which are considered as an improvement from all the previous works based on monolayer phantom measurements.

For the **GI** measurements, the chosen shape used for the measurements basically consists in a polyhedral shape with a big layer for the muscle and a thinner one for the fat phantom, which is considered the best configuration for torso-based IB2OB measurements [77]. In addition, three different containers were developed to compare the measurements and to observe how the channel is affected by the shape of the containers.

In Fig 3.14 the containers used for the phantom measurements are depicted. In Fig 3.14 (a, c and e) the schema of the containers with their size is shown, while in Fig. 3.14 (b, d, f) the developed containers are shown. Regarding the materials used for the containers, the first and second container corresponding to Fig. 3.14 (a, b) and (c, d) were made of polyethylene terephthalate (PET) of 1.5 mm width, where the faces are pasted with epoxi resin. The last container Fig. 3.14 (e, f) was manufactured by a 3D printer using hard polypropylene (PP). The use of plastic is preferred to other elements like glass, due to the transparency plastic presents against the EM wave. The dielectric constant of plastic is approximately 2.5 and barely varies with frequency, while the glass can vary from 4.5 to 20. Moreover, it should be stressed that the main component used for the phantoms, acetonitrile, is a corrosive element that dissolves many materials such as acrylonitrile butadiene styrene (ABS) plastics or glue. PET, PP and epoxi resin were chosen due to the resistant they offer in front of acetonitrile.

From Fig. 3.14 it is seen that the shapes and sizes of the containers differ between them. The shapes are either squared or hexagonal and the size varies from 6 l to approximately 15 l of volume. The large-squared container has and overall internal volume of 25 cm $\times$ 25 cm $\times$ 25 cm with two layers of 23 cm $\times$ 25 cm $\times$ 25 cm and 2 cm $\times$ 25 cm $\times$ 25 cm, and 15.625 l (please note that for all the containers, the 2 to 3 top cm are left empty to avoid overflow). Between layers, there is a divider sheet also made of PET and 1.5 mm of width. On the hexagonal container, nonetheless, the edge length is 15.5 cm and the height is 25 cm, being the total volume 15.604 l (Area of regular hexagon $\times$ height = base $\times$ apothem $\times$ 3 $\times$ height = 15.5 cm $\times$ 13.42 cm $\times$ 3 $\times$ 25 cm = 15604 cm^3 = 15.604 l). In this case the fat layer is divided in three faces, the central one of 2 cm and the two lateral faces of 1.5 cm width. Lastly, the small squared container has 19 cm edge size and 18 cm height. The PP has a width of 2 mm, being the fat layer smaller than in the other cases with only 1.5 cm width. Achieving then 19 cm $\times$ 19 cm $\times$ 18 cm = 6.5 l.

On the **cardiac** scenario, where the blood has a main role, a trilayer phantom setup was used to replicate this scenario in the fairest possible manner. For that, a blood layer was included in the large-squared container shown in Fig. 3.14 (a,b). A PET bottle of 10 cm $\times$ 15 cm $\times$ 20 cm was inserted inside the container (Fig. 3.15). This phantom measurement setup is a novelty from the previous phantoms experiments because now, not only two layers, but three are considered for the measurements. The counterside of this setup is smaller range of movement that the in-body antenna has compared with the bi-layer measurement.
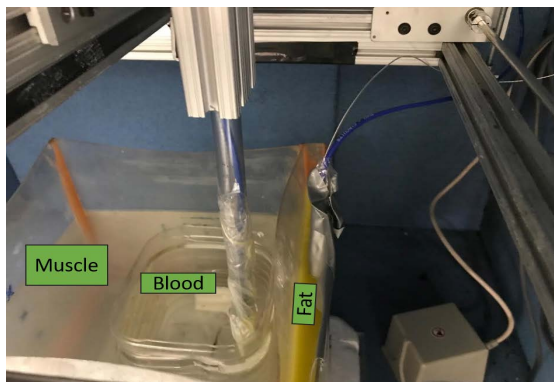
Figure 3.15: Phantom container setup with blood, muscle, fat phantom, and both in-body antennas [15]

3.1.2 *In vivo* measurements

Experimental measurements in living animals are a required step when it comes to channel characterization for in-body scenarios. The heterogeneity of the human body and the movement of the tissues, organs, and fluids make this kind of measurements still a necessary part of the channel modeling. Multiple animals are used for experimentation, but concerning the gastrointestinal area of the human body, pigs and similar animals are the most used for these measurements [53]. This is explained by the similar GI conditions of humans and pigs either in size and distribution of the organs.

Living animals experiments are always conducted by experienced professionals, assuring that the animal is treated and controlled throughout the experiment ensuring animal welfare according to the ethical standards [36] (an ethical committee approved the experiments under the protocol WIBEC 2015/0463). Gastrointestinal experiments are conducted by digestive surgeons in hospital facilities. The common methods used for digestive operations are either laparotomy or laparoscopy. Laparotomy is the oldest method which consists of open surgery, while the laparoscopy is a newer method much less invasive for the patient. The laparoscopy performs some incisions in the abdominal cavity of the patient, where a gas (CO_2) is inserted, then the laparoscope itself that has a light and a camera is introduced into the inflated abdominal. Next, some perforations to insert the endoscopic tools (graspers, needle driver...) are performed. Other important tools are the trocars, which are shaped tubes used by all the instruments as a support to be introduced in the abdominal cavity.
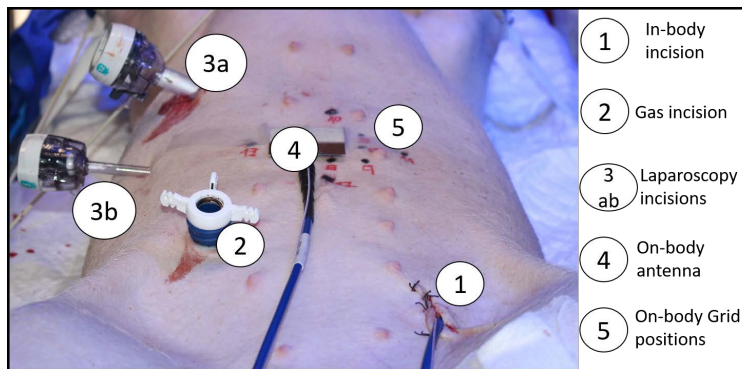
Figure 3.16: Laparoscopy performed in living animals experiments

For this research four *in vivo* experiments were performed, in which three of them were carried out through laparoscopy and the last one was performed only with a small incision. The laparoscopy method is preferred to other methods to assure the longer life expectancy of the animal during the operation. Besides, the real-life conditions are better maintained throughout the operation than with the open surgery.

Fig. 3.16 shows the laparoscopy commonly performed in the abdominal cavity of the pig. As seen four incisions are performed: Fig. 3.16 element 1, to insert the in-body antenna, the cable connected to the VNA, and the wire of the magnetic sensor attached to the antenna; Fig. 3.16 element 2, to insert the gas (CO_2) used to inflate the abdominal cavity of the pig; and Fig. 3.16 elements 3a and 3b to insert the laparoscope itself and the laparoscopic instruments e.g., graspers, trocars, to precisely move the in-body antenna to the place under interest. Moreover, in Fig. 3.16 elements 4 and 5 represent the on-body antenna and the on-body grid used to perform the measurements.

These *in vivo* experiments were performed to mimic as much as possible the phantom measurements performed in the laboratory, mainly using the same antennas, cables, magnetic tracker, and VNA. The procedure used to perform the experiments was the following: firstly, the in-body antenna was inserted into the abdominal cavity of the animal together with the magnetic sensor; the antenna and the magnetic sensor were recovered with latex to avoid the direct contact with the internal fluids. Secondly, the in-body antenna was placed at the desired location and the gas is extracted from the animal so the most realistic conditions are kept. Then the on-body antenna is located over the abdomen of the animals and the forward transmission coefficient (S_{21}) is calcu-

lated for each sample point over the abdomen. The distance is simultaneously calculated using the magnetic tracker and sensors for each measurement point.

The last *in vivo* experiment was performed for the low UWB signals, which as explained in section 3.1 the in-body antenna was attached to a transmitter of 4 cm × 4 cm × 2 cm. The transmitter is bigger than the laparoscope working channel so other method has to be employed to conduct the measurement. It consisted on performing a small incision over the abdomen of the animal and manually inserting the transmitter with the 6DOF sensor of the EM tracker *Aurora* surrounded with small bowel. In this case, a spectrum analyzer was chosen to connect the receiver antenna because the FPGA transmitter is autonomous. In this case, the EM field generator (Fig. 3.10 (b)) was interfering the low UWB signal. Therefore, the procedure was slightly different than before. Firstly, the receiver positions were marked over the abdomen of the pig and the transmitter with the 6DOF sensor (Fig. 3.10 (c)) was introduced inside the animal and the distance between the in-body antenna and the on-body positions was measured. Then, the EM field generator was switched off and the measurements with the receiver antenna and the spectrum analyzer (*Anritsu MS2723B*) were carried out. Lastly, the antenna and the sensor are extracted and introduced at other position of the abdomen of the pig.

3.2 Software simulations

Software simulations are the most extended methodology to characterize the channel due to its simplicity and feasibility. Nevertheless, as explained in section 2.1.3 they are not able yet to mimic all variables that appear in human body. In this dissertation, numerical calculations are used to complement the measurements in laboratory and in animal experiments. This means that all the designs are performed with the intention to mimic the experimental measurements either in phantom or *in vivo* experiments.

Firstly, it must be stressed that the software used for simulations is the commercial software CST Microwave Studio® (CST MWS) because of the multiple human models it offers. The main computer used for the computation of the simulations was an *AZKEN MUGA T- Series 5*, with 6 processors Intel(R) Xeon(R) CPU E5 v3 3.5 GHz, and 64 GB of RAM. Moreover, a GPU NVIDIA Tesla K40c was added to improve the speed of the calculations. However, even with the GPU some trade-offs in simulations were taken into account as later will be explained. For the simulations performed on the UWB frequency band the time-domain analysis was chosen due to the broadband nature of the system, the FIT method on CST. On the other side for low UWB signals the frequency domain solver was chosen due its faster behavior. Concretely, the

FEM method was selected because it has close boundary conditions like our models, which are enclosed inside the human body or phantom containers.

Chapter 4

Methodology

This chapter describes all the experiments performed in phantoms and living animals, as well as, the numerical simulations designed to replicate the experiments.

4.1   Phantom-based measurements

All the experiments listed in this section have been measured with the phantom measurement testbed described in section 3.1.1. Moreover, the experiments are divided according to the phantom container used for the experiments (Fig. 3.14), in this way, the methodology used for the measurements is easier to understand. On the contrary, the measurements campaigns were performed in such a way that from the results of one experiment the need to perform other measurements changing some variables arose. Therefore, at the end of the section a table summarizing the experiments, and a temporal line describing the order of the experiments are added.

   All the phantom measurements share some of the characteristics used to perform the experiments. All of them had a common task: measure the S_{21} for IB2OB scenarios in the gastrointestinal tract (only one of them in the cardiac area). For that purpose, measurements were taken with the VNA (Fig. 3.11 element 3), which was previously calibrated in order to compensate the effect of the coaxial cables and connectors through a *full*-calibration method using a *Rosenberger Calibration Kit RPC - 3.50*.

   Five S_{21} snapshots per position were taken in order to enhance the Signal-to-Noise Ratio (SNR), then the average value per position is calculated. The phantom container is then placed inside the chamber and the muscle and fat phantom were poured in their respective compartments. It should be mentioned

that since the phantom properties vary with temperature the latter was strictly controlled at 24°C by a thermostat.

The magnetic sensors (trakStar, Fig. 3.9) attached to the antennas provide their XYZ position information. The effect of the sensors over the antennas was tested and it was checked to be negligible. Moreover, in order to avoid inaccuracies, for each snapshot, the position is calculated 100 times. Then, the average value of the distance is taken for each snapshot.

The variable characteristics for each phantom measurement campaign, such as the frequency band used, the container, the antennas, and their positions, and the VNA parameters are described in the following.

4.1.1 Measurements performed with a large-square container

The large-square container, hereinafter in this section, container, was the container where the first measurements were conducted. This rectangular shape is the most commonly used in literature due to its simplicity and its relative similarity with the human gastrointestinal part. The container showed in Fig. 3.14 (a) and (b) is a novel multilayer phantom container, which allows the channel measurements not only for a single layer but two of them, concretely, muscle and fat.

The phantom measurement campaigns performed with this container are

- Case A

- Homogeneous case

Case A

The measurements were taken for different positions of the in-body and on-body antennas, being these antennas the described in Section 3.1 (Fig. 3.1 and Fig. 3.3) and named *In 1* and *On 1*. The in-body grid was set up in a uniform cubical 3D lattice with a certain resolution in XYZ plane, whereas the on-body grid was located over the outer wall of the fat layer of the container.

In Fig. 4.1 the schema of the distribution of the sample points is shown. On the left, the general view of the phantom container and the sample measurement points are displayed, while the zoomed grids are depicted on the right. From the general view, one can see the big compartment used for the muscle phantom and the smaller layer of only 20 mm width used for the fat phantom. Besides, as observed, the receivers (i.e., on-body antenna) locations are shown using different color circles located on the YZ plane and numbered from 1 through 5. Ideally, the receivers are located forming a cross-shape grid with 20 mm

Figure 4.1: Case A: Phantom measurement grid setup. On the left, the general view for the 5 Rxs and the in-body positions. On the right the zoomed view of the 5 Rxs and the in-body grid.

distance from the central position (Rx1). Nevertheless, those antennas were manually attached to the wall of the container, so there is a human error which caused a displacement of the antennas as seen in Fig. 4.1. The inner grid, where the in-body antenna (the transmitter) is located, is represented by the cyan circles and they are placed forming a $12 \times 11 \times 2$ lattice in XYZ. These in-body sample points are almost perfectly spaced with a resolution of 10 mm $\times$ 10 mm $\times$ 10 mm in XYZ, thanks to the 3D cartesian positioner where the in-body antenna is attached. Table 4.1 shows the VNA parameters of this measurement campaign.

Table 4.1: Phantom measurements Case A
Measurement setup parameters

Resolution points	N = 3201
Frequency Band	f = [3.1, 8.5] GHz
Resolution frequency	Δf = 1.69 MHz
Resolution Bandwidth	3 kHz
Output Power	8 dBm

Homogeneous Case

An homogeneous phantom measurement campaign was also carried out to perform an initial comparison between the receiving on-body antennas. The antennas used for this measurement campaign were the in-body and on-body antennas described in Section 3.1 and in (Fig. 3.1, Fig. 3.3, and Fig. 3.4) and named *In 1*, *On 1*, and *Vivaldi*. As a remark, the *On 1* antenna has an omnidirectional pattern, while the *Vivaldi* antenna has a directive one. On the contrary to previous case described before (Case A), for this phantom measurement campaign, only one type of phantom for the channel characterization was employed. This is because the aim of this campaign was to perform an initial comparison between on-body antennas. Therefore, the key point of the experiment was to maintain the same conditions used to perform the measurements for both on-body antennas i.e., the relative position of the setup inside the anechoic chamber (Fig. 3.11 element 1), the phantom container, and the phantom itself. Moreover, the phantom used for this measurements is no longer the acetonitrile phantom described in Section 3.1.1 and Fig. 3.12 but the sugar phantom shown in Fig. 3.13 (b) which is easier to develop and handle. This phantom was not as accurate as the previous phantoms used, but as said the main point in this experiment was to maintain the same conditions for both antennas.

The VNA parameters are summarized in Table 4.2.

Table 4.2: Phantom measurements Case Homogeneous Measurement setup parameters

Resolution points	N = 3201
Frequency Band	f = [3.1, 6] GHz
Resolution frequency	Δf = 905.97 kHz
Resolution Bandwidth	3 kHz
Output Power	8 dBm

In Fig. 4.2 the schema of the distributions of the sample points is shown. Now the container used for the measurements is the same as large-squared container but the smaller layer previously used for the fat phantom now is empty and the on-body antennas are attached to the sugar phantom directly. The measurements were done in three consecutive days to assure that the properties of the phantom depicted in Fig. 3.13 (b) were maintained. Moreover, the measurements were alternated between the on-body omnidirectional patch antenna (*On 1*) and the directive UWB antipodal Vivaldi antenna (*Vivaldi*). Finally, 13 receiving positions for each antenna were measured. In Fig. 4.2 left

Figure 4.2: Case Homogeneous: Phantom measurement grid setup. On the left, the general view for the 13 Rxs and the in-body positions. On the right the zoomed view of the 13 Rxs and the in-body grid.

side one can see that the on-body receivers were placed forming a 3 cm × 3 cm grid (receivers 1 to 9) and four receivers located 5 cm away from the central position forming a cross shape grid (receivers 10 to 13). As seen, the common misplacement resulting from the manual handling of the sensor and the antenna lead to some misalignment between the ideal grid and the real one. The inner sample positions were performed with the 3D cartesian positioner forming a 11 × 3 × 3 lattice in XYZ being the distance between sample positions 1 cm × 3 cm × 1 cm in XYZ respectively.

4.1.2 Measurements performed with an hexagonal container

The hexagonal container was developed to explore the influence of the shape of the container in the measurements. It was meant to be as high as the large-square container and able to contain the same volume of liquid inside it.

Fig. 3.14 (c) and (d) shows the shape and the size of the container. More-over, in this case, a comparison between antennas was also performed, com-paring two in-body and two on-body antennas. The in-body antennas used for the measurements are those described in Table 3.1 (Fig. 3.1 and Fig. 3.2) and named as *In 1* and *In 2*. The on-body antennas used for the measurements were also listed in Table 3.1 and Table 3.2 (Fig. 3.3 and Fig. 3.7), concretely *On 1* and *On 4*. The measurements performed with these four antennas al-

Table 4.3: Phantom measurements Hexagonal container
Measurement setup parameters

Resolution points	N = 1601
Frequency Band	f = [3.1, 6.1] GHz
Resolution frequency	Δf = 1.87 MHz
Resolution Bandwidth	3 kHz
Output Power	8 dBm

lowed the comparison of the channel performance for different antennas at the same conditions, and also the comparison with previous measurements. In the measurements performed in Case A the antennas used for these measurements were also utilized but with different container shape.

In Table 4.3 the VNA parameters for the measurements are described, the resolution points were reduced because there was no evident difference between both configurations and the last is more time-efficient. The methodology used for the measurements is schematically shown in Fig. 4.3. In this measurements 4 pairs of antennas were employed, but only the positions of a pair of them are shown. All the on-body antennas were intended to be placed at the same position, but the manual placement of the antennas created a deviation of ± 2 cm. They were placed over the fat layer of the phantom container, 4 receiving positions over the central face of the container (Rx1-4) and two receiving positions (Rx5 and 6) over the lateral fat-faces of the container. The first set of 4 Rxs were placed with respect to the central position and located 20 mm from it in Y- and Z-axis (20 mm in horizontal and vertical position). The second set of Rxs are placed 20 mm from the edge in horizontal position and at the middle position of the container in Z-axis. The in-body antennas were attached to the 3D cartesian positioner so their placement is completely accurate. They were placed in a rectangular grid in (XYZ) with 6 × 9 × 3 sample positions with a 10 mm displacement between each position.

4.1.3 Measurements performed with a small-squared container

The measurement campaign carried out with the small squared container had the objective to compare how the channel behavior is affected by the size of the container. The measurements were performed with the large-squared container and then with a container that had the same volume but different shape (hexagonal). Now, maintaining the initial squared container shape, the size is reduced
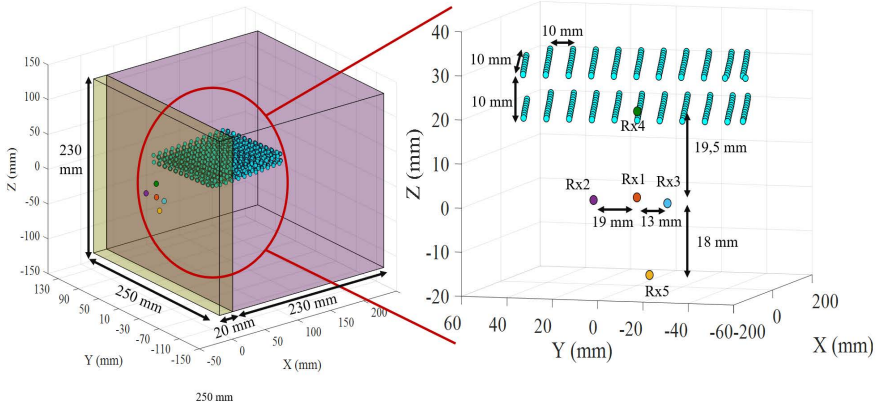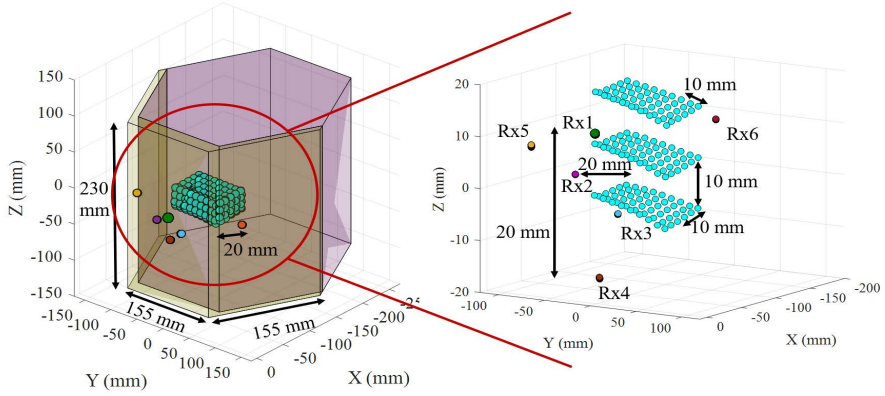
Figure 4.3: Case Hexagonal: Phantom measurement grid setup . On the left, the general view for the 6 Rxs and the in-body positions. On the right the zoomed view of the 6 Rxs and the in-body grid.

Table 4.4: Phantom measurements Case C
Measurement setup parameters

Resolution points	N = 1601
Frequency Band	f = [3.1, 6.1] GHz
Resolution frequency	Δf = 1.87 MHz
Resolution Bandwidth	3 kHz
Output Power	8 dBm

in both the muscle and the fat layer. As a reminder, in Fig. 3.14 (e) and (f) show the size and the shape of the container used in these measurements.

Case C

For these measurements, and following previous campaigns not only a phantom container comparison, but also an on-body antenna comparison was performed. For that, two on-body antennas were used *On 1* and *On 4*. The in-body antenna is also the antenna most used along this dissertation *In 1*. Table 4.4 lists the VNA parameters used for this configuration. The phantoms used for these measurements were the muscle and fat phantom described in section 3.1.1. Moreover, following other sections structure, in Fig. 4.4 the methodology of
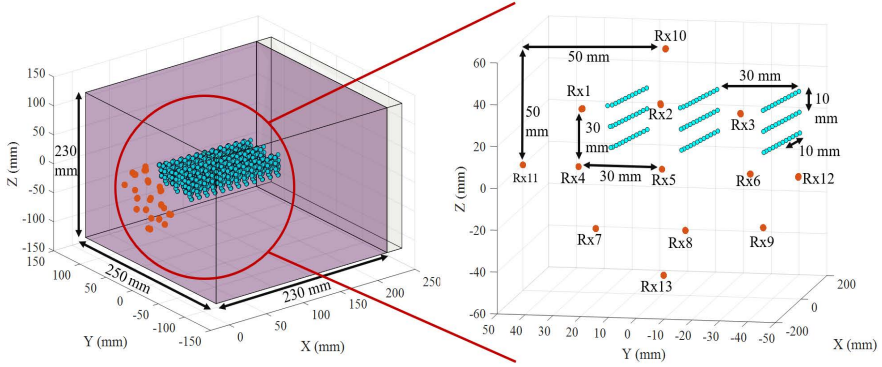
69
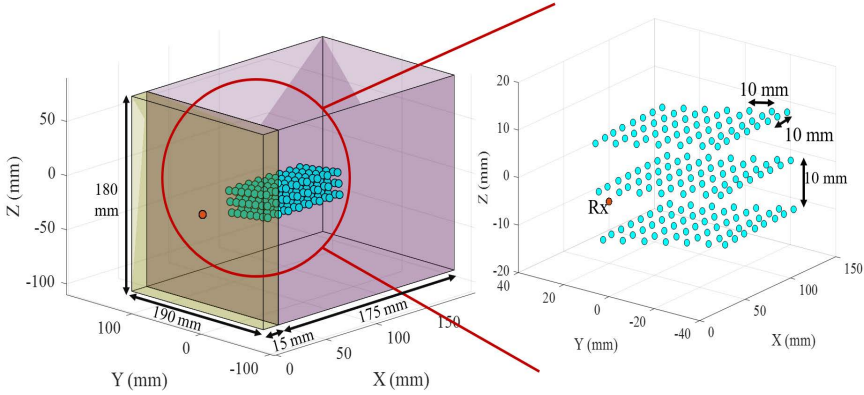
Figure 4.4: Case C: Phantom measurement grid setup. On the left, the general view for the 1 Rx and the in-body positions. On the right the zoomed view of the Rx and the in-body grid.

the measurements is shown. For these measurements only one Rx position is chosen due to the small dimensions of the phantom and the relatively large size of the antenna with respect of the container. Therefore, only the central position of the outer layer of fat phantom is chosen for the measurements. Both antennas were placed approximately at the same position (with some manual displacement), thus in Fig. 4.4 only one Rx position is shown. Concerning the in-body antenna, it was attached to the 3D cartesian positioner and it formed a rectangular grid in (XYZ) of 8 × 7 × 3 with 10 mm of distance between sample points in all the three axis.

4.1.4 Measurements performed with a tri-layer phantom container

The cardiac scenario required a different characterization of the channel than the gastrointestinal scenario. First of all, the channel is application-oriented. This means that we are characterizing the channel for the case of a leadless pacemaker and an eavesdropper trying to interfere with the signal. As explained in section 1, the leadless pacemaker consists of an intra-heart node that transmits signals to the subcutaneous transceiver, which sends the signal to the external device. Nevertheless, the problem arises when there is a malicious attacker trying to interfere with the intra-heart signal. According to this, the characterization of the channel now is performed at IB2IB and IB2OFF

scenarios, which slightly differs from the previous IB2OB measurements. The in-body antennas used for the measurements are two identical antennas, (*In 1* described in section 3.1 and Fig. 3.1), being the only difference between them those caused by the manufacturing process. The off-body antenna used for the measurements is the on-body antenna also described in section 3.1 and Fig. 3.3 *On 1*, which also behaves well at the vicinity of the human body.

The phantom setup used for the cardiac measurements contrasts with the gastrointestinal scenario because inside the heart, the blood is the main component. Therefore, the blood phantom, described in section 3.1.1 and Fig. 3.13 (a), was added to the large-square container and it was shown in section 3.1.1, Fig. 3.15. In this case, one in-body antenna was located inside the fat phantom, replicating a subcutaneous transceiver placed under the skin and the second in-body antenna was placed inside the blood phantom mimicking the leadless pacemaker located inside the ventricle of the heart. The antenna inside the blood phantom was moved by the 3D Cartesian positioner, trying to mimic the movement of the heart with steps of 5 mm. For the IB2OFF link, the off-body antenna was attached to the 3D cartesian positioner, while the in-body antenna inside the blood remained static.

The methodology used to perform these measurements was divided in two parts. Firstly, an IB2IB measurement campaign was conducted and the data was processed. Different assumptions obtained from the results were considered to conduct the IB2OFF measurement campaign. Moreover, in order to properly understand how the blood is affecting the measurements, two IB2IB measurement campaigns were performed, with the only difference of the blood phantom. In Fig. 4.5 the sample points of each measurement campaign are described. Fig. 4.5 shows the general view of the phantom measurements campaign, it is similar to other cases where the large-squared container was used, but now the third container containing blood is added. This container is located approximately at 45 mm from the external wall of the fat layer. The schema on the left shows the sample points used to perform both measurements. Nevertheless, the measurements were performed with different configurations. On the right-top the IB2IB is shown, the red circle represents the subcutaneous receiving antenna. Two different measurements were performed with the moving antenna: with and without the blood container (only with muscle and fat) to observe the influence of the blood on the channel. For the blood-case the sample points were spaced 5 mm $\times$ 5 mm $\times$ 10 mm on (X,Y,Z) achieving 295 sample points. For the in-body measurements without the blood, the space between antennas was slightly different, being: 10 mm $\times$ 10 mm $\times$ 10 mm on (X,Y,Z) and having 175 sample points.

On the right-bottom, the off-body grid measurements are shown. Now, the procedure was to maintain still the in-body antenna, which was located inside
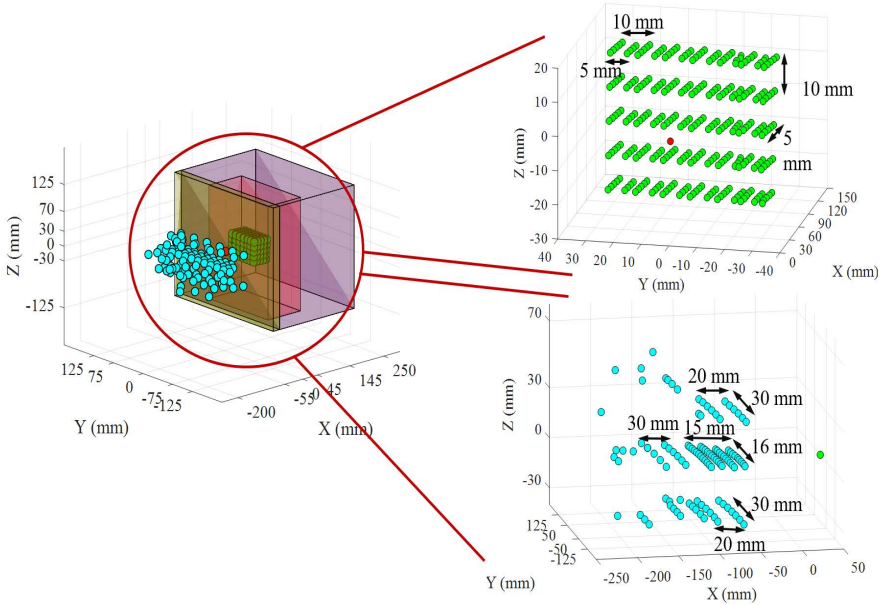
Figure 4.5: Cardiac scenario: Phantom measurement grid setup for the tri-layer measurements. On the left the genetral view for the IB2IB and IB2OFF measurements. On the top right, the zoomed view of the IB2IB grid and on the bottom right, the zoomed view of the IB2OFF

the muscle phantom (on Chapter 7 the reason why the in-body antenna is placed inside the muscle phantom and not the blood phantom will be clarified) approximately at 5 cm from the wall of the container. Then, the off-body antenna was moved first with the 3D cartesian positioner and then manually, because the range of the robotic arm was not large enough. From the Fig. 4.5 it can be seen that the off-body grid has more irregular shape than the in-body grid, this is because the movement performed on air and not inside the body suffer from less attenuation, thus, the measurements were performed to cover the maximum space possible and also to optimize on time. The total number of off-body samples was 111.

The VNA parameters used for both scenarios are given on Table 4.5

Table 4.5: Measurement setup parameters for cardiac scenario

Resolution points	N = 1601
Frequency Band	f = [3.1, 5.1] GHz
Resolution frequency	Δf = 1.25 MHz
Resolution Bandwidth	3 kHz
Output Power	8 dBm

4.1.5 Summary of the phantom experiments

Table 4.6 summarizes the main information of the phantom measurements previously described. To avoid repetition, the parameters that are maintained constant for all the measurements are not in the table. Concretely, the common elements are the output power P = 8 dBm, the snapshots per position N_s = 5, the magnetic tracker samples per position N_d = 100 and the resolution bandwidth f_{if} = 3 kHz.

Table 4.6: Summary of the phantom experiments parameters

Measurement	Resolution points	Frequency band (GHz)	Δf	Container type	Phantoms	In-body positions	On-body positions	In-body antennas	On-body antennas
Case A	3201	[3.1 - 8.5]	1.67 MHz	Large-square	Muscle and fat	$12 \times 11 \times 2 = 264$	5	1	1
Case Homogeneous	3201	[3.1 - 6]	937.21 kHz	Large-square	Muscle (sugar)	$11 \times 3 \times 3 = 99$	13	1	2
Case Hexagonal	1601	[3.1 - 6.1]	1.87 MHz	Hexagonal	Muscle and fat	$6 \times 9 \times 3 = 162$	6	2	2
Case C	1601	[3.1 - 6.1]	1.87 MHz	Small-square	Muscle and fat	$8 \times 7 \times 3 = 168$	1	1	2
Case cardiac	1601	[3.1 - 5.1]	1.23 MHz	Tri-layer	Blood, muscle, and fat	295 & 175	111 (off)	1	1

4.2   *In vivo* experiments

All the experiments described here have been performed either at the facilities of the Hospital Universitari i Politècnic la Fe, València, Spain or at the Intervention Center of the Oslo University Hospital, Oslo, Norway. They all were performed in female pigs of approximately 50 Kg. Moreover, to accomplish with the ethical regulations [36], in each intervention not only these experiments but others (out of the scope of this dissertation) were performed. At the end of this section a table summarizing all the experiments is found.

First *in vivo* experiment

In Section 3.1.2 the system used to perform the measurements is described. As a reminder, this experiment was conducted via laparoscopy and the antennas used for the measurements were *In 1* and *On 1*, described in Section 3.1 and shown in Fig. 3.1 and Fig. 3.3. Moreover, the antennas are connected to the Port-1 and -2 of a VNA and the 3D magnetic sensors of the *trakStar* system are attached to the antenna. The configuration parameters of the VNA for this experiment are given in Table 4.7.

Table 4.7: *In vivo* I
Measurement setup parameters

Resolution points	N = 1601
Frequency Band	f = [3.1, 8.5] GHz
Resolution frequency	Δf = 3.37 MHz
Resolution Bandwidth	3 kHz
Output Power	8 dBm

It must be stressed that these measurements were performed with the aim of compare the phantoms measurements in Section 4.1.1, "Case A". As in phantoms the forward transmission coefficient (S_{21}) for different IB2OB positions was calculated. Moreover, to reduce the noise produced by the channel, five snapshots per positions are calculated and then averaged. The magnetic tracker also computes 100 positions per each IB2OB position, which are also averaged. The dynamic range for this configuration was found to be 100 dB. In Fig 4.6 a general view of the receiver grid over the pig is shown, as well as, a detailed schema of the distance between antennas.

In Fig. 4.6 (a) the setup used for the experiment is shown: the trocars used for the laparoscopy, the on-body antenna with the magnetic tracker, and the

(a)   (b)   (c)
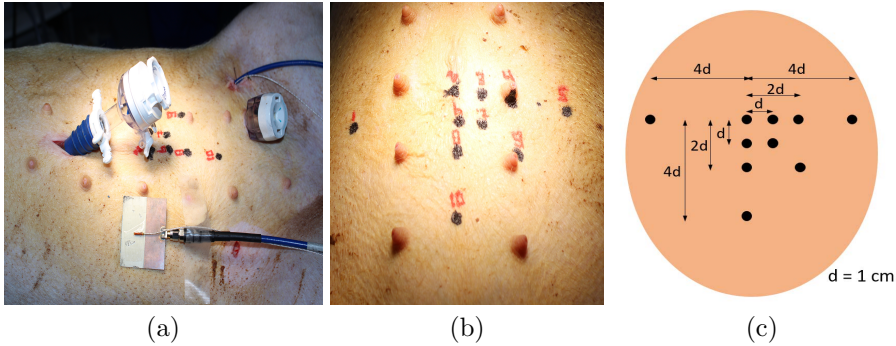
Figure 4.6: *In vivo* experiment I (a) Full setup (1), (b) on-body grid (1), (c) on-body grid detailed (1)

on-body grid. In Fig. 4.6 (b) and (c) the positions of the on-body antenna are depicted. With the aim of optimization an asymmetric grid was chosen with 10 on-body positions. The minimum distance between on-body positions was 1 cm and a maximum of 8 cm between positions 1 and 5.

For this experiment 4 in-body positions were measured for different organs, concretely, small bowel, liver, and two positions in the colon. Unfortunately, due to some inconveniences, like the ripping of the latex covering the in-body antenna, only the measurements taken in one in-body position of the colon are performed with enough precision to extract information from the measurements. Regarding the measurements taken in the liver and the small bowel, the in-body antenna and the on-body grid were placed at distances of about 20 cm, which are too far for UWB frequencies.

Second *in vivo* experiment

The second animal experiment was performed as a replica of the previous experiment, which suffered for many inaccuracies and mistakes due to the lack of experience and unpredictable variables that occur during the *in vivo* measurements.

In this case, two different on-body antennas were used. This was a first approach to compare between antennas in *in vivo* experiments. The first on-body antenna was the patch antenna shown in Fig. 3.3, *On 1* and omnidirectional, while the second antenna is shown in Fig. 3.5, *On 2* and it is directive. Moreover, the VNA parameters are found in Table 4.8. The main difference is the bandwidth which now is reduced to $f_{max} = 6$ GHz, this is a bandwidth (BW) of

Table 4.8: *In vivo* II
Measurement setup parameters

Resolution points	N = 1601
Frequency Band	f = [3.1, 6] GHz
Resolution frequency	Δf = 1.81 MHz
Resolution Bandwidth	3 kHz
Output Power	8 dBm

2.9 GHz instead of BW = 5.4 GHz as it was before. This change is motivated by the results shown in phantom and in the previous animal experiment, which will be fully explained in the next chapter. Likewise, 5 snapshots were taken per measurements and averaged to reduce the noise, and also the magnetic tracker took 100 measurements per sample point.

Fig. 4.7 shows similar information as the Fig. 4.6 but for the second *in vivo* experiment. It must be stressed that, Fig. 4.7 (a) is the same image as Fig. 3.16. In this case, the on-body grid is different compared with the first experiment. Now, 13 Rxs are placed at different positions and at larger distances. Being the minimum distance 2 cm and the maximum 10 cm. Now, more similar conditions to the real WCE application, where the patient has a belt around the abdomen, are mimicked.

Concerning the in-body positions, in this case it was important to compare both antennas in the most similar conditions. Therefore, first, the in-body

(a) (b) (c)
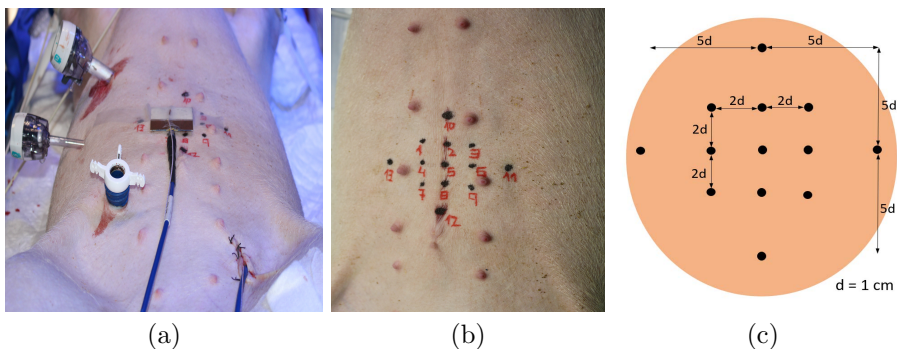
Figure 4.7: *In vivo* experiment II. (a) Full setup (2), (b) on-body grid (2), (c) on-body grid detailed (2)

antenna (*In 1*) was placed at the desired position and the *On 1* antenna is measured for all the 13 positions of the on-body grid. Then, maintaining the in-body antenna at the same position, the on-body antenna is changed for the *On 2* antenna and the same procedure is repeated. Finally, 3 in-body positions were measured, due to time constraints and some unexpected problems that appeared during the procedure. All the in-body positions were located around the small or large bowel of the pig and the first and second positions were performed with both on-body antennas. For the last in-body position the time ran out and the measurements were performed only with one antenna (*On 1*).

Third *in vivo* experiment

The third *in vivo* experiment had as an objective the comparison between antennas in a deeper way than the previous measurements. In this case, three on-body antennas were used for the comparison: *On 1*, *On 2* and *On 3* (Fig. 3.6). The VNA parameters are found in Table 4.9, where it is possible to see how the BW is of only 2 GHz from 3.1 to 5.1 GHz, i.e., the low-UWB frequency band and the resolution points are larger N = 2001. For these measurements, also 5 snapshots per position were taken with the VNA and 100 samples per position are taken with the magnetic tracker.

Table 4.9: *In vivo* III
Measurement setup parameters

Resolution points	N = 2001
Frequency Band	f = [3.1, 5.1] GHz
Resolution frequency	Δf = 1 MHz
Resolution Bandwidth	3 kHz
Output Power	8 dBm

Fig. 4.8 shows the setup used for the *in vivo* measurements. Following the structure in previous sections. Fig. 4.6 (a) shows the laparoscopy performed to the animal and the on-body antenna, which in this case in the slot patched directive antenna (*On 2*). Fig. 4.8 (b) and (c) show the grid used as on-body positions.

In this case, also 13 receiving positions were used for the on-body grid. This schema is slightly different to the previous ones because now the positions are spread over the abdomen of the pig. This is motivated so for each in-body position a larger range of distances are measured, being the shortest distance
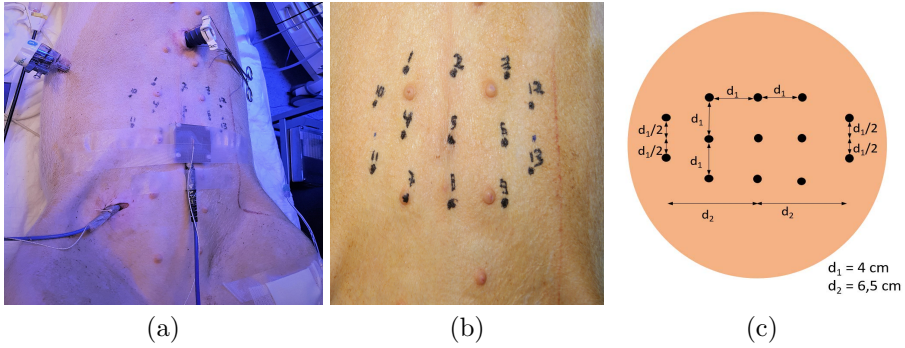
Figure 4.8: *In vivo* experiment III. (a) Full setup (3), (b) on-body grid (3), (c) on-body grid detailed (3)

between on-body antennas 2.7 cm and the largest distance 13.6 cm. Now, three in-body positions were measured for each on-body antennas.

In vivo experiment for low UWB signals

The last *in vivo* experiment was different than the previous animal experiments described above. This experiment was performed in the facilities of the Intervention Center at the Oslo University Hospital. In this case, two helical invert-F antennas (Fig. 3.8, *Helical*), were placed inside and outside the animal body. As commented, the in-body antenna was attached to an FPGA transmitter [73], which transmits the signal depicted in Fig. 4.9 between 0 and 80 MHz.

Fig. 4.10 (a) shows the setup used for the experiment, and as explained in section 3.1.2, both the spectrum analyzer and the EM Aurora tracker are connected to the laptop, which had a dedicated software created to automatize as much as possible the procedure. The on-body antenna is placed over the abdomen of the pig, which previously had an on-body grid drawn Fig. 4.10 (b) of 12 Rxs. The distances between the adjacent Rx positions are 3 cm horizontally (X-axis) and 5 cm vertically (Y-axis), and in this case the EM Aurora tracker takes 208 samples per position, that afterwards are averaged to reduce the uncertainty in the calculation of the antennas distance. Regarding the in-body antenna, it is attached to the FPGA based transmitter and it is placed at 3 different positions of the human body, resulting in 36 different distances. The different in-body positions were chosen to observe how the placement of the antenna inside the body affects the signal. It was always

Table 4.10: *In vivo* for low UWB signals
Measurement setup parameters

Spectrum Analyzer Model	MS2723B
Resolution points	N = 550
Frequency Band	f = [0, 80] MHz
Resolution frequency	Δf = 145.45 KHz
Reference level	-12 dBm
RBW	10 kHz
VBW	3 kHz

placed between and deep to the intestines of the animal replicating typical wireless capsule endoscope positions.

Finally, the parameters used for the spectrum analyzer are given in Table 4.10

4.2.1 Summary of the *in vivo* experiments

In Table 4.11 the summary of the differences between the experiments are shown. The common elements for the VNA-based measurements are the output power P = 8 dBm, the snapshots per position N_s = 5, the magnetic tracker samples per position N_d = 100 and the resolution bandwidth f_{if} = 3 kHz.
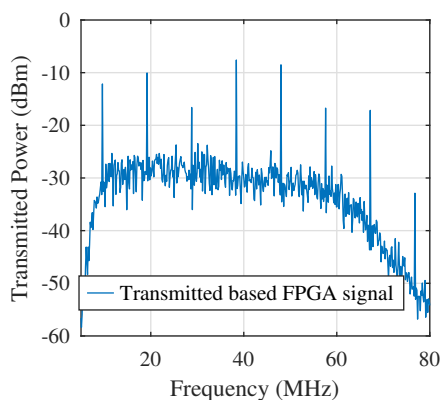
Figure 4.9: Signal transmitted by the FPGA from 0 to 80 MHz [73]
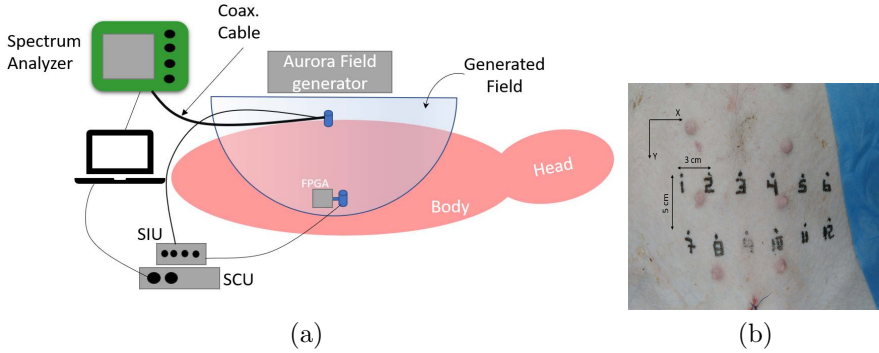
Figure 4.10: *In vivo* experiment for low UWB signals (0-80 MHz). (a) Schema of the setup, (b) On-body grid

Table 4.11: Summary of the *in vivo* experiments parameters

	Resol. points	Δf (MHz)	Frequency band	In-body positions	On-body positions	On-body antennas
In vivo 1	1601	3.37	[3.1, 8.5] GHz	1	10	1
In vivo 2	1601	1.81	[3.1 6] GHz	3	13	2
In vivo 3	2001	1	[3.1 5.1] GHz	3	13	3
In vivo low	550	0.145	[0 80] MHz	3	12	1

Finally, in Fig. 4.11 the timeline of the *in vivo* experiments and the phantom measurements previously described is shown.

4.3   Software simulations

The software simulations are used to compare the described measurements in sections 4.1 and 4.2. Two different designs were used for this purpose and they can be divided between container-like designs and human body designs.
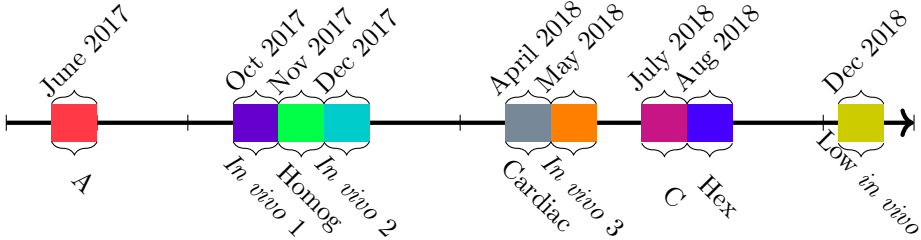
Figure 4.11: Timeline of the phantom measurements & *in vivo* experiments

For the UWB frequency band, a design used to mimic the phantom measurements described in Case A was developed, and then a design whose purpose was to mimic a real torso, the *in vivo II* measurements, and the low UWB signal *in vivo* experiments.

Squared container design

This design had the purpose to mimic the experimental phantom measurements described in Case A. For that the conditions were replicated in the fairest way possible. It should be mentioned the frequency band used was f ϵ [3.1, 5.1] GHz, the low UWB frequency band. Moreover, the antennas used for this simulations were the designs of *In 1* and *On 1* (Fig. 4.12). Fig. 4.12 (a) shows the in-body antenna *In 1* (Fig. 3.1), and the on-body antenna *On 1* (Fig. 3.3 is shown in Fig. 4.12 (b).

Fig. 4.13 shows the design in CST, which consists in the phantom container, the muscle and fat phantom, and the in- and on-body antennas. Contrarily to experimental measurements, all the variables are controllable in simulations, thus, some elements such as the anechoic chamber, the 3D cartesian positioner, and the magnetic tracker, which were employed to better control the unpredictable variables of the environment, are not included in the design.

As seen from Fig. 4.13 both antennas were faced, being both of them aligned with the front plane (fat phantom layer). The misalignment between them is considered negligible. As well as in the experimental setup Case A, the in-body and the on-body antennas were the transmitting and the receiving antenna respectively. In addition, the forward transmission coefficient (S_{21}) was calculated. Regarding the methodology used to perform the simulations, the in-body antenna was placed in the center of the phantom container, whereas the on-body antenna is 3 mm away from the center of the external side of the fat phantom layer. The only variable in the simulations was the in-body distance

which ranged from 5.5 to 9.5 cm. First the in-body antenna was moved along the Y-axis (Fig. 4.13) from d = 5.5 cm to 9.5 cm in steps of 1 cm each. Then it was moved along the X-axis at a fixed Y-axis position of d_y = 7.5 cm and d_x ranging from -4 cm to 4 cm with steps of 2 cm for each sample point. The total number of sample points obtained was 9, which entirely differs with the amount of sample points obtained with phantom measurements (sample points in Case A = 1320). It should be said that for each sample position, one day of simulation was required, while the phantom measurements were performed in approximately five days.

Furthermore, the computational time and memory required for the software simulations are critical parameters. And for that reason there should be a compromise between the size of the model, the resolution obtained and the time and memory required. The size of the container was set as 17 × 15 × 15 cm^3 with two layers of 15 × 15 × 15 cm^3 and 2 × 15 × 15 cm^3. The reduction of the container design allows the increasing of the mesh size of the model, i.e., more accurate, but the time and memory resources decrease.

Human body design

The second design uses the abdominal part of the voxel human family of CST MWS. Concretely from the female CAD model Nelly. It was chosen to confirm whether the measurements performed in living pig were well performed. There were two different designs using this model, one for the UWB frequency band and the other one for the low UWB signals.

(a)   (b)
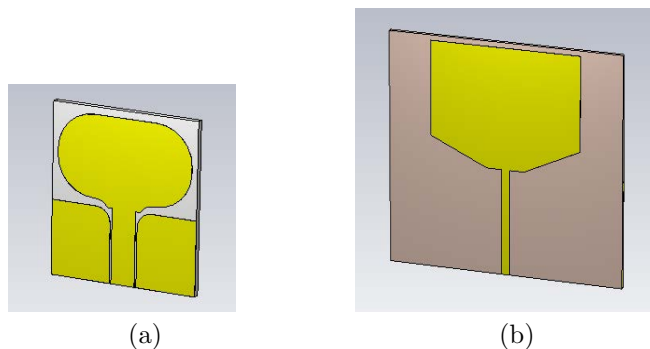
Figure 4.12: Design of the antennas used in the software simulations with CST. (a) *In 1*, CPW-feeding planar in-body antenna, (b) *On 1*, planar patch on-body antenna
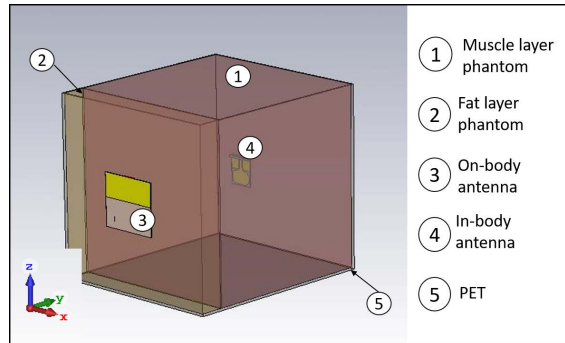
Figure 4.13: CST MWS design to replicate the experimental measurements performed in phantom
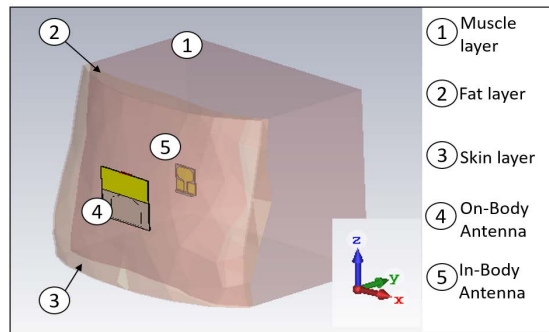
Figure 4.14: CST MWS design to replicate the torso of a human female model

The first design was used for the low UWB frequency band (3.1 - 5.1 GHz) and to reduce the complexity of the simulation, only the skin, fat and muscle of the human body was considered as shown in Fig. 4.14. Besides in order to have the most accurate result, cells with a mesh size ranging from an edge length of 0.14 - 2.61 mm were used for these simulations.

The in-body and on-body antennas (*In 1* and *On 1*) were located in different positions along the X-, Y- and Z-axis. The on-body antenna was placed in three different positions over the skin layer of the CAD model Nelly. First, at the position shown in the Fig. 4.14 (0,0,0) (X,Y,Z) and then 2 cm displaced in X and Z, having then (2,0,0) cm and (0,0,2) cm in (X,Y,Z) . The in-body antenna was moved at six different positions for each on-body position. Firstly, it was
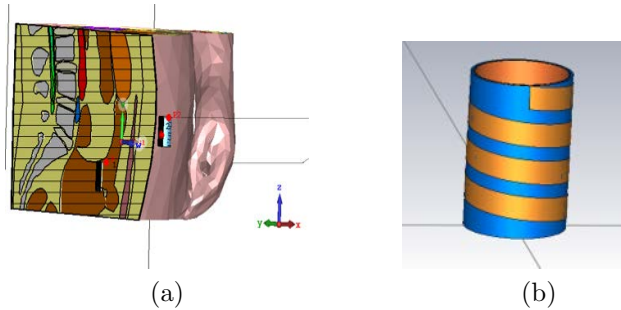
Figure 4.15: (a) A sagittal slice of CST MWS software CAD model Nelly, including in- and on-body antennas. (b) Design of the Helical invert-F implanted antenna used for the simulations

moved 1 cm along the Y-axis, considering the antennas aligned, and then it was displaced at two positions shifted 2 cm in X-axis. The points covered (all in cm) were [0,(4-7),0], and [(2,4),6,0] in (X,Y,Z) concretely ranging from d = 4 cm to 7.95 cm. Finally, 18 sample points were obtained from simulations using this configuration.

The second design was simulated for low UWB signals, Fig. 4.15 (a) shows the model used for the measurements and one location of the antennas. It is a sagittal slice of the model, where in this case all the organs and tissues provided by the software are considered. Moreover, Fig. 4.15 (b) shows, the design of the antenna Helical invert-F antenna described in the Fig. 3.8, *Helical*. The bandwidth used for the simulations was f ϵ [40,80] MHz with 1001 frequency points and different cell size ranging between [0.00146, 138.41] mm. A total of 55 samples points were taken, where 29 positions were performed with the antennas aligned, and only changing the Y-Distance, between d_{min} = 4.4 cm and d_{max} = 17.1 cm. The last 26 samples points were taken while changing the azimuth and elevation between antennas until ϕ = 35° and θ = 30°.

Chapter 5

Results for the Gastrointestinal scenario at the UWB frequency band

In this chapter the results obtained for the gastrointestinal area at the UWB frequency band from all the measurements and simulations are exposed. A deep study of all the data extracted either in frequency and delay domain is realized. Furthermore, the results are linked with the published papers of this dissertation.

5.1 In-body to On-body characterization via Path Loss models

5.1.1 Phantom container Case A and software simulations results

The phantom measurements described in Case A showed the following reflection parameters (Fig. 5.1). These parameters were obtained with the VNA during the measurements campaign. As seen both parameters are matched since they are below -10 dB.

Nevertheless according to some researchers [64, 78] the standard used to see whether the antennas are radiating or not, commonly set as having a reflection coefficient below -10 dB, is not applicable to in-body antennas. The antenna is not in a free-space environment but in a high losses environment, thus the tissue around the antenna is acting as a radiating element so the VNA

Figure 5.1: Reflection parameters (S_{11} & S_{22}) obtained with the VNA for the phantom experiments described in section 4.1.1 as case A

calculation of the S_{11} is no longer accurate depending on how the antenna is designed. This topic is still under research, so it will not be further treated and in this dissertation, the in-body antennas are considered matched for reflection parameters below -6 dB as in [64].

Experimental Path loss model obtained from the Case A

As said the VNA calculated the forward transmission coefficient S_{21} with N resolutions points (Table 4.1), so from the S_{21} the path loss (or system loss) was calculated as

$$PL(dB) = -10 \log_{10} \left(\sum_{i=N} \frac{(|H(f_i)^2|)}{N} \right) \tag{5.1}$$

being $H(f)$ the channel transfer function with N resolution points, where $H(f) = |S_{21}|e^{-j\phi_{S_{21}}}$, being $|S_{21}|$ and $\phi_{S_{21}}$ the module and the phase of the transmission coefficient respectively.

In Fig. 5.2 the channel transfer function is depicted. Each line represents the absolute value of the S_{21} as a function of the frequency for different distances between antennas. For simplicity, the misalignment between antennas was selected to be negligible, considering always 2 cm of fat between antennas.
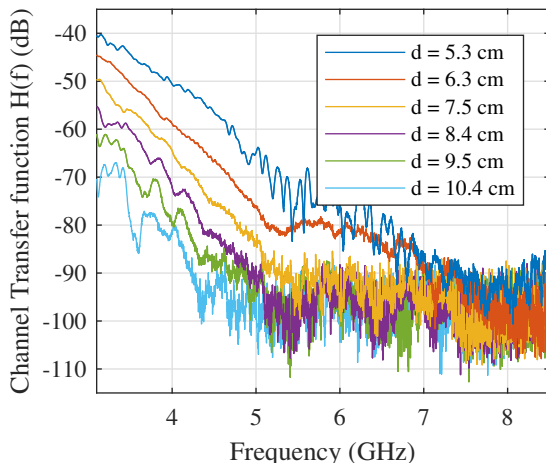
Figure 5.2: Channel transfer function, $H(f)$, obtained from the measurements performed during the measurement campaign case A. The lines represent different samples points at different distances considering the antennas aligned

As seen for the Fig. 5.2 the signal becomes very noisy for values below than -95 dB approximately, thus the signal is considered negligible for values below this threshold. For further calculations a margin of 5 dBs is considered for the noise level, thus the threshold of -90 dB is considered to assure the validity of the signal. Furthermore, from Fig. 5.2, the tendency of the channel transfer function as a function of the frequency for different distances is also examined. For a distance of approximately d = 5.5 cm the H(f) has a constant decay until f = 5.5 GHz. For d = 6.5 - 9.5 cm the decay arrives until f = 5.1 GHz, same occurs with d = 10.5 cm but the signal is very unstable. From the curves it can be seen a clear response considering the noise negligible until f = 5.1 GHz and with a power decrease of approximately 8 dB between them. This power decay agrees with the results obtained in [54], where the decay is 7.4 dB/cm for homogeneous phantom measurements.

From the measurements obtained, the path loss from f = 3.1 to 5.1 GHz and a d_{max} = 9.5 cm is depicted in Fig. 5.3. As already mentioned, only the measurements with power above the noise threshold are computed. The path loss obtained can be modeled as a distance-dependent logarithmic function (Eq. 2.3, please note the renamed of the SL for PL to standardize with previous literature), where the shadowing term is given by $N(\mu, \sigma)(dB)$, a normal distribution with standard deviation $\sigma = 2.307$ and zero mean (μ). The path
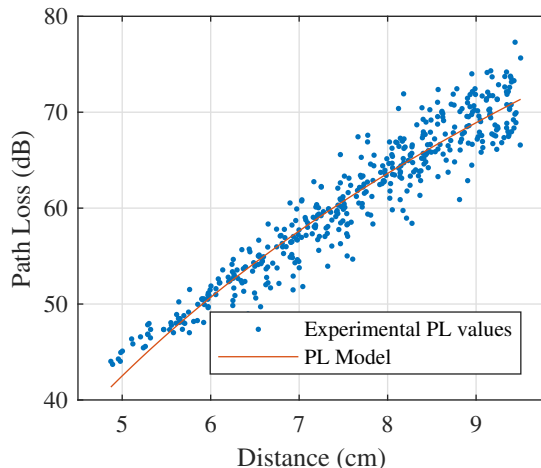
Figure 5.3: Path Loss values and Path Loss model obtained from the phantom experiments performed in the measurement campaign Case A

loss exponent is given as $n = 10.34$ and the reference distance and PL value are given by $d_0 = 1$ cm and $PL_0 = $ -29.76 dB. Setting the reference distance as to 1 cm is not trivial. Despite measurements were not taken at such low distances, this value mathematically obtained is more convenient to compare with previous models in literature and the posterior models that will be presented in this dissertation. Moreover, setting $d_0 = 1$ cm allows the simplification of the model.

$$PL(dB) = PL_0(dB) + 10n \log (d/d_0) + N(\mu, \sigma) \qquad \text{(2.3 revisited)}$$

Similar studies are presented in the literature with similar results, like in [20], in which they conducted software simulations for 3.4 to 4.8 GHz.

Software simulation results of the phantom experimental setup

As explained in section 4.3 the measurements were replicated in simulations, but the simulations are very complex in time and computational results so a reduction in the size of the container was a non-avoidable step. The size of the container chosen for the simulations was $17 \times 15 \times 15$ cm^3 as already said, but before arriving to that conclusion, different tests were conducted with different containers size. Concretely, following the design and specifications shown in Fig. 4.13, four setups were used.
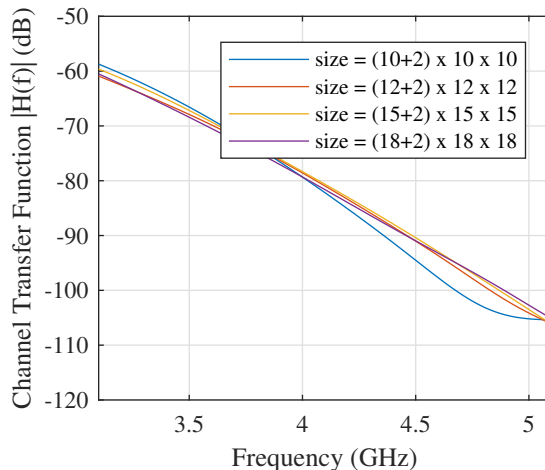
Figure 5.4: Channel transfer function obtained from simulations used to evaluate how the size of the container is affected in simulations. Distance between antennas = 9.5 cm

- $12 \times 10 \times 10$ cm^3, with two layers of $10 \times 10 \times 10$ cm^3 and $2 \times 10 \times 10$ cm^3 for the muscle and fat phantom respectively

- $14 \times 12 \times 12$ cm^3, with two layers of $12 \times 12 \times 12$ cm^3 and $2 \times 12 \times 12$ cm^3 for the muscle and fat phantom respectively

- $17 \times 15 \times 15$ cm^3, with two layers of $15 \times 15 \times 15$ cm^3 and $2 \times 15 \times 15$ cm^3 for the muscle and fat phantom respectively

- $20 \times 18 \times 18$ cm^3, with two layers of $18 \times 18 \times 18$ cm^3 and $2 \times 18 \times 18$ cm^3 for the muscle and fat phantom respectively

For these simulations the on-body antenna was always placed on the middle of the fat layer of the phantom container and the in-body antenna always located 9.5 cm away from the on-body antenna. In Fig. 5.4 the results of the four simulations can be seen. For a long distance of d = 9.5 cm the smaller container showed slightly different results than the other simulations. This shows how for aligned antennas and distances up to 9.5 cm between antennas the size of the container can be easily decreased from the original phantom container, which was 25 cm of edge length. Finally, the container of 15 cm of edge length was used for the comparison.

Fig. 5.5 the comparison between measurements performed in phantom and the software simulations is shown. Now, the measurements are only plotted
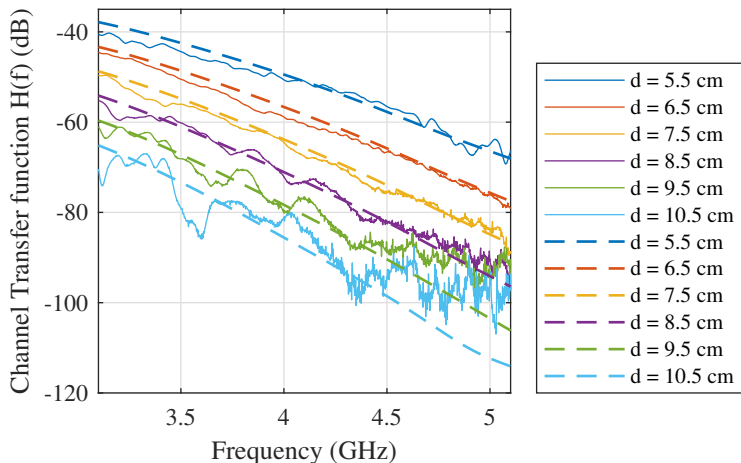
Figure 5.5: Channel transfer function obtained from phantom measurements (Case A) (solid lines) and software simulations in CST MWS (dashed lines)

until f = 5.1 GHz because it is chosen as the upper limit in frequency. In addition, in Fig. 5.5 for distances larger than 9.5 cm the measurements and simulations disagree for values below -90 dB (approximately), as explained this is due to the noise that appear in the system for that values which of course does not exist in ideal simulations.

The path loss of the software simulations was calculated and compared with the phantom measurements (Fig. 5.6). The results showed high level of agreement with the experimental results, where the simulated PL is coinciding with the lowest experimental PL for each given distance.

Summary

From the first phantom measurement campaign (Case A) and the software simulations that replicated it, an initial path loss model is defined for the low UWB frequency band, concretely from f = 3.1 to 5.1 GHz and for a distance range of 4.8 to 9.5 cm.

All this results are published in the following:

[40] **S. Perez-Simbor**, M. Barbi, C. Garcia-Pardo, S.Castelló-Palacios, N. Cardona "Initial UWB In-Body Channel Characterization Using a Novel Multilayer Phantom Measurements Setup," in *IEEE Wireless Communications and Networking Conference, WCNC*, Barcelona, Spain, April 2018.
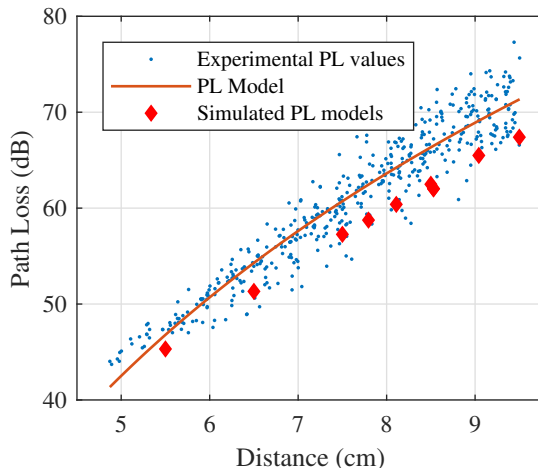
Figure 5.6: Experimental path loss values (Case A), path loss model and simulated path loss values obtained with CST MWS

5.1.2 Phantom Container Case Homogeneous results

The homogeneous phantom measurement campaign was performed with the aim of start a comparison between on-body antennas for IB2OB measurements. The reflection coefficient of the in-body and both on-body antennas placed inside the sugar phantom and over the layer of the container are shown in Fig. 5.7. All the antennas showed a good reflection coefficient for the full band under study (3.1 to 6 GHz in this case).

Following the steps in previous section 5.1.1 the channel transfer function was directly computed from the measured S_{21} and it is shown in Fig. 5.8. Fig. 5.8 (a) depicts the response of the omnidirectional patch antenna while the response of the antipodal Vivaldi antenna is shown in Fig. 5.8 (b). The response of the patch antenna shows that for distances greater than 6.5 cm the noise floor threshold set as -90 dB (see section 5.1.1) is reached for frequencies aroung 4.5 GHz, whereas for the Vivaldi directive antenna, longer distances are achieved. Therefore, the behavior of the omnidirectional antenna is more restrictive than the directive antenna in terms of distance and frequency bandwidth as a function of frequency. Therefore, in order to have the maximum components above the noise level for both antennas, the maximum distance chosen for the calculation of the path loss (system loss) is $d_{max} = 6.5$ cm and a maximum frequency of $f_{max} = 5.1$ GHz.
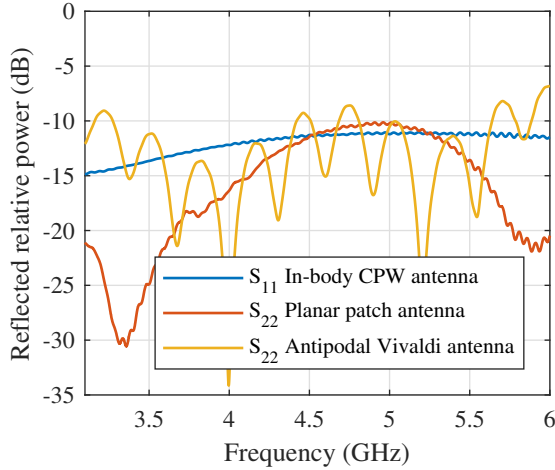
Figure 5.7: Reflection parameters (S_{11} & S_{22}) obtained with the VNA for the phantom experiments described in section 4.1.1 as case Homogenous

From the response of the $|H(f)|$ is seen that the *Vivaldi* antenna has smoother response and greater slope whereas the omnidirectional is antenna is more irregular and has a lower slope. This behavior is reflected in the PL values, which are extracted from the channel transfer function by Eq. 5.1. In Fig. 5.9 the path loss values are depicted for both antennas, where a different behavior is easy to see. As expected from the results in Fig. 5.8, the directive Vivaldi antenna has higher path loss values than the omnidirectional patch antenna (greater slope). A possible explanation might be due to the high path losses that the directive antenna experiences when the antennas are not located in the area of the directive beam. Besides, in Fig. 5.9, the aligned samples of the omnidirectional patch antenna are highlighted in brown color. As seen they have more similar behavior to the PL values of the antipodal Vivaldi antenna. Then, from the path loss values, different path loss models are computed from Eq. 2.3 and listed in Table 5.1

From the results, the *Vivaldi* antenna shows a higher path loss exponent (n), than the other two models, which was expected from the results. Nevertheless, it may come out as a surprise that the variance (σ) of the omnidirectional antenna is smaller than the directive one. The path loss model resulting from the combination of both antennas has a path loss exponent in between the other two models and a higher variance. This is due to the wide spread and wide difference that appear between the measured path loss values.
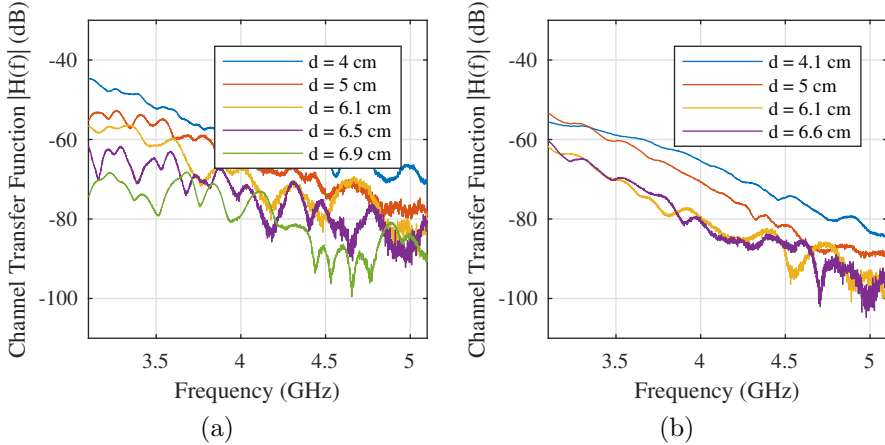
Figure 5.8: Measurement campaign Case Homogeneous. (a) $|H(f)|$ for the planar patch omnidirectional antenna (b) $|H(f)|$ for the directive antipodal Vivaldi antenna

Table 5.1: Path loss models for phantom measurements Case Homogeneous

Path Loss model Vivaldi	Path Loss model Patch omnidirectional	Path Loss model both antennas
d = [3, 6.5] cm	d = [3, 6.5] cm	d = [3, 6.5] cm
f = [3.1 , 5.1] GHz	f = [3.1 , 5.1] GHz	f = [3.1 , 5.1] GHz
$PL_0 = 17.5$ dB	$PL_0 = 24.86$ dB	$PL_0 = 19.05$ dB
$d_0 = 1$ cm	$d_0 = 1$ cm	$d_0 = 1$ cm
n = 7.37	n = 5.09	n = 6.56
$\mu = 0$	$\mu = 0$	$\mu = 0$
$\sigma = 5.72$ dB	$\sigma = 4.26$ dB	$\sigma = 6.79$ dB

Summary

These results were published in [79] and were the result of a collaboration between institutions. In [79], in addition to the path loss models a practical case where those were applied for localization purposes was presented. From the results, despite the higher path loss exponent, the directive antenna performed slightly better than the omnidirectional antenna when using localization al-
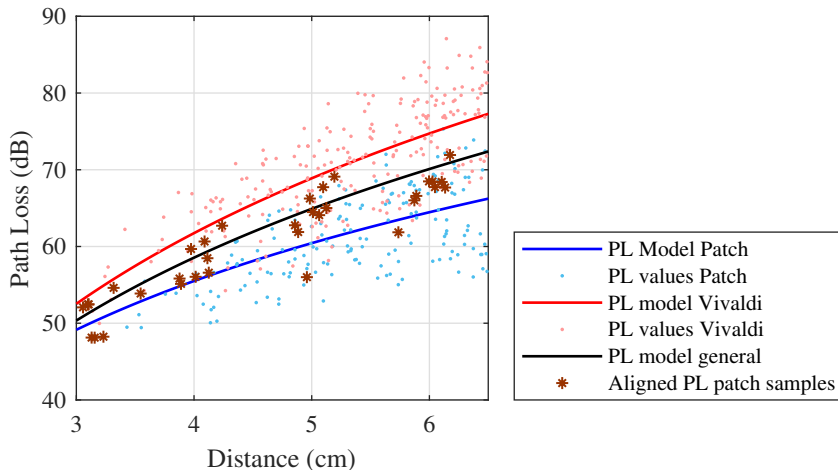
Figure 5.9: Experimental path loss values (Homogeneous case), path loss models for each on-body antenna and the combination of both of them. The highlighted samples are the aligned path loss samples

gorithms. This result might seem contrary to as the expected ones, since as said, the path loss exponent was smaller for the omnidirectional antenna. The necessity of a good understanding of the effect of the antenna in the channel to properly characterize the IB2OB channel in the UWB frequency band arises. Further comparisons between antennas should be performed.

[79] **S. Perez-Simbor**, M. Barbi, M. Ramzan, X. Fang, C. Garcia-Pardo, N. Cardona, Q. Wang, N. Neumann, D. Plettemeier, "Experimental Path loss models comparison and localization of Wireless Endoscopic Capsule in the Ultra Wideband Frequency Band," *Bodynets*, pp.1-11, Oulu, Finland, October 2018

5.1.3   *In vivo* 1 and 2 and software simulations results

In this section the results obtained from the first two *in vivo* measurements are described. As explained in section 4.2, from the first *in vivo* experiment only the results in colon were successful. Even though these measurements were used as an initial approach to understand the behavior of the human body as a propagation channel, the channel model was calculated from the results obtained in the second animal experiment.
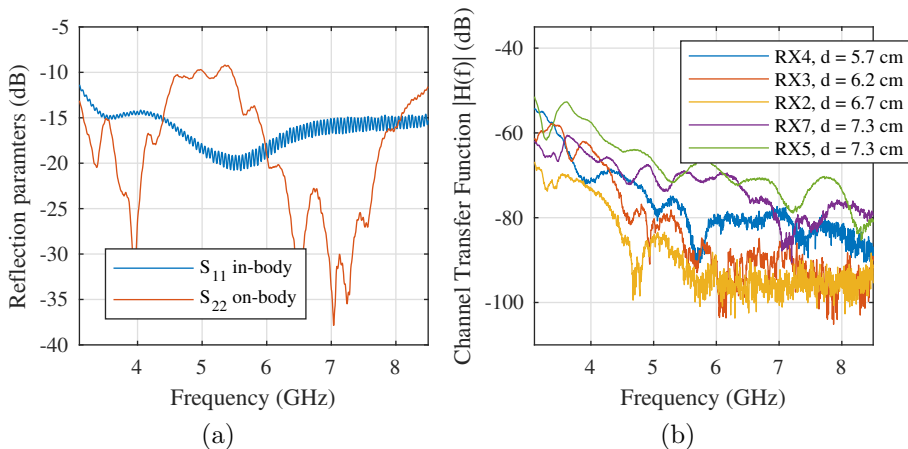
Figure 5.10: *In vivo* experiment I. (a) Reflection parameters (S_{11} & S_{22}), (b) channel transfer function obtained from the forward transmission coefficient (S_{21})

Antenna matching and channel transfer function for *in vivo* 1

The reflection coefficient of both the in-body and on-body antenna are shown in Fig. 5.10. The reflection parameters and the channel frequency response were directly obtained from the VNA. As seen both antennas showed good reflection parameters. The channel transfer function had similar results as the phantom measurements previously described, with good propagation behavior until approximately $f = 5.1$ GHz. From the measurements obtained in phantom and animal measurements, it is possible to assure that for the higher part of the spectrum, the signal presents very high losses, thus, in the *in vivo 2* measurements, the maximum frequency is set as $f = 6$ GHz.

Antenna matching and channel transfer function for *in vivo* 2

The second *in vivo* experiments used two different on-body antennas as described in section 4.2. In this section only the measurements performed with the omnidirectional patch antenna (Section 3.1 and in Fig. 3.3, *On 1*) will be described. The results obtained with the *On 2* antenna Fig. 3.5 will be shown in the following sections.

Regarding the in-body antenna, the matching varies with the surrounding tissues. In Fig. 5.11 the three in-body positions of the transmitting antenna can be seen. Since the scenario of interest is mainly the GI tract of the animal,
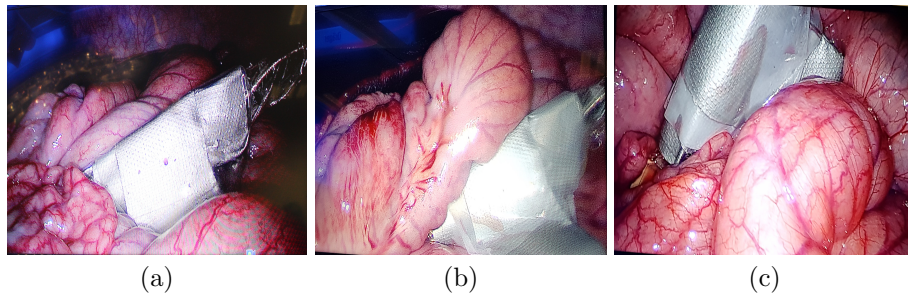
Figure 5.11: In-body positions for the *in vivo* 2 measurements. (a) In-body position 1, colon (Tx1), (b) in-body position 2, small bowel and colon (Tx2) and (c) in-body position 3, colon (Tx3)

the in-body positions were located so as to be surrounded by either color or small bowel indistinctly. Tx1 and Tx3 are surrounded by colon, whereas Tx2 is surrounded by small bowel and colon.

The reflection coefficient of either in-body or on-body can vary depending on their location and the surrounding tissues, especially in real configuration. In Fig. 5.12 (a), the absolute value of the S_{11} is shown for the *in vivo* 2 measurements considering the three transmitting positions (Tx1, Tx2 and Tx3) and three random on-body receiving positions.
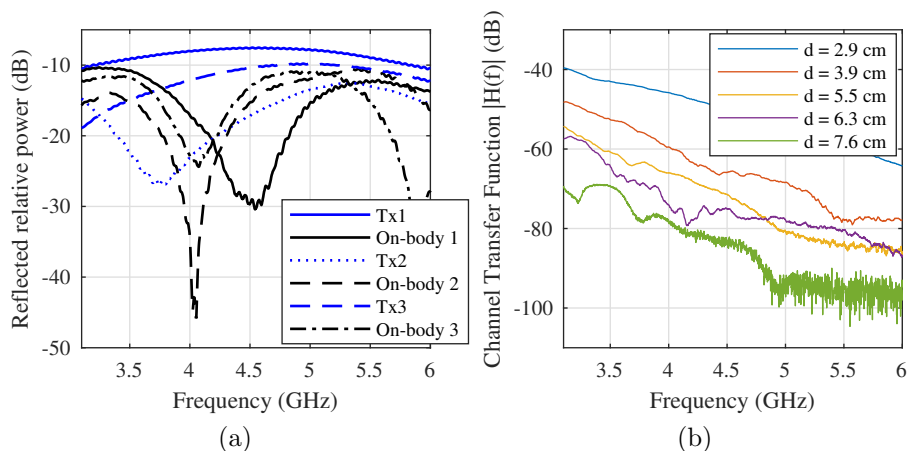
Figure 5.12: (a) Reflection parameters of the *in vivo* 2 experiment, (b) Channel transfer function $|H(f)|$ of the *in vivo* 2 experiment

As can be observed, the reflection coefficient of the in-body and on-body antennas varies depending on the position of the antenna, i.e., Tx1 and Tx3 show similar response (both are surrounded with small bowel), while Tx2 has slightly different shape. In any case, the S_{11} has a maximum value of -7 dB for Tx1, for which we consider this antenna matched, because as said, for in-body communications values of -6 dB are accepted values for the S_{11}. The on-body matching is also shown with the reflection coefficient plotted for three different on-body positions. As seen, the on-body reflection coefficient is always below -10 dB. Moreover, comparing Fig. 5.12 (a) and Fig. 5.1 it is possible to see the high level of agreement between the phantom measurements and the *in vivo* measurements.

According to previous sections, the channel transfer function for different in-body and on-body positions from 3.1 to 6 GHz is depicted in Fig. 5.12 (b). One can observe how as the distance between antennas becomes larger, the response of the $|H(f)|$ above the noise floor level (approximately -90 dB) decreases, and thus, the useful bandwidth. Therefore from Fig. 5.12 (b), for distances above d = 7.62 cm and frequencies above f = 5.1 GHz the signal is considered to be under the noise floor level. Therefore, for further analysis, a trade-off between the maximum distance between antennas and the maximum useful bandwidth should be achieved. Hereinafter, the frequency band considered will be 3.1 - 5.1 GHz and maximum distance of d_{max} = 8 cm. These results agree with the literature in which the low UWB frequency band is studied [20, 54].

Software simulations results of the human body design

The software simulations described in section 4.3 were compared in this case to the *in vivo* 2 measurements. The channel transfer function of the results obtained with simulations are shown in Fig. 5.13. Simulations were performed only for the desired frequency bands i.e., 3.1 to 5.1 GHz in order to reduce the computational cost. Fig. 5.13 also shows that the slope of the channel transfer function is very similar for equivalent distances between antennas. It is important to take into account that inside the pig, the exact tissues between antennas are unknown. In this comparison, it is possible to see high similarities between the results performed with both methodologies like in the phantom measurements Case A and its respective software simulations. In that case (section 5.1.1), when the antennas were completely aligned and perfectly matched with the simulations, the results were very similar. Same occurs here, where the comparison between *in vivo* and simulations shows a high level of matching, validating the animal experiments.
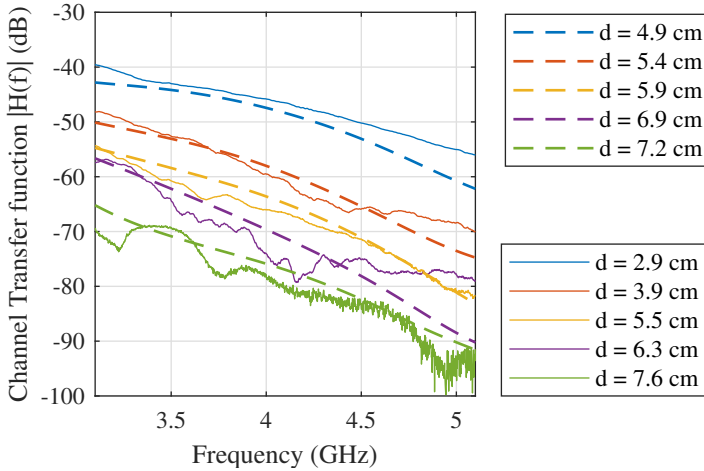
Figure 5.13: Channel transfer function obtained from *in vivo* 2 measurements (solid lines) and software simulations in CST MWS using the CAD mode Nelly (dashed lines)

Path Loss models

The path loss model (or system model) is obtained from the channel transfer function as described in Eq. 5.1. Fig 5.14 (a) illustrates the PL as a function of the distance for the *in vivo* 2 measurements and the simulations performed in with Nelly. As seen, the 3 different in-body positions are highlighted. At Fig. 5.14 (b) the PL values of the first *in vivo* experiment are added, now all the in-body positions of the second experiment are homogenized and it is possible to see a difference between the first and the second experiment. The first experiment nonetheless, was the first one performed and some inaccuracies were committed, therefore, for further analysis these measurements will be omitted.

Furthermore, one can observe how the PL values given by the numerical simulations are a few decibels below those deduced from the *in vivo* measurements (Fig. 5.14 (a)). This slight mismatch is given for all the contributions that appear in real experiments, i.e., reflections inside the pig, blood flow, and respiration, which are not considered in the numerical simulations. Moreover, in simulations both antennas are faced, whereas in *in vivo* measurements, a perfect alignment between antennas is difficult to achieve. The same behavior was obtained in section 5.1.1, where the values of the numerical simulations are lower than the experimental measurements in phantom.
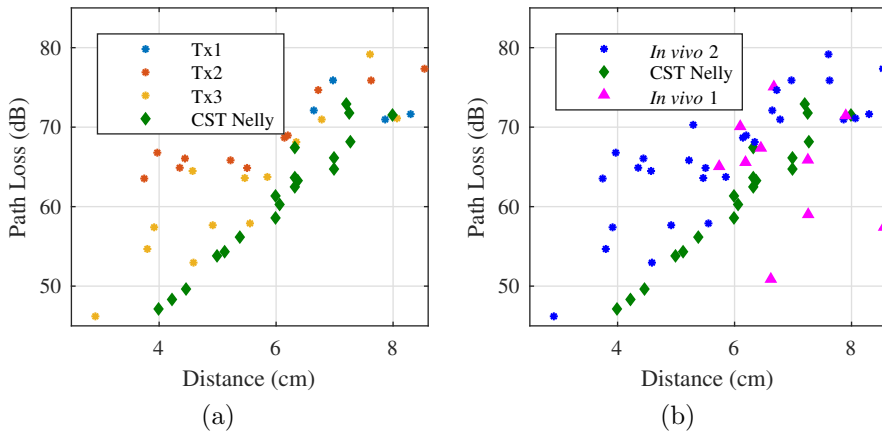
Figure 5.14: Path loss values for *in vivo* measurements. (a) Path loss values for each in-body position for the *in vivo* experiments 2 and software simulations with CST Nelly. (b) Path loss values for the *in vivo* measurements in 1 and 2 and the CST software simulations with CST Nelly

In order to obtain a general PL model, phantom measurements have to be taken into account for the large number of positions measured and the real external conditions of the measurements. For this purpose, the PL phantoms measurements from Case A and their correspondent software simulations are added to Fig. 5.14 and plotted in Fig. 5.15. In Fig 5.15, a similar trend and PL values between the three configurations can be observed. Nevertheless, the data values obtained from the multilayer phantom container have a shift of two centimeres in the x-axis. As a recall, the experiments performed in phantom considered muscle and 2 cm width of fat phantom layer. From the EM properties of the human tissues (Fig. 2.1) the conductivity of the fat is very low, barely affecting the attenuation of the signal. As a consequence, the distance used for this model can be changed regarding the quantity of abdominal fat. To confirm this, the phantom measurements performed in Case A were compared with the phantom measurements performed in Case Homogeneous. This is, because they used the same antennas and the same phantom container one with and the other one without fat phantom. Despite the fact that the phantom used for the homogeneous case was sugar phantom, it can be used for comparison purposes. Therefore, in Fig. 5.16 (a) the PL for the phantom measurements described in Case A and Case Homogeneous are depicted. It should be stressed that the frequency band used for the calculation of the path loss was f = [3.1 to 5.1] GHz for both cases. As seen in Fig. 5.16 (b), where the multilayer measurements are 2 cm shifted to the left (this is, subtracting
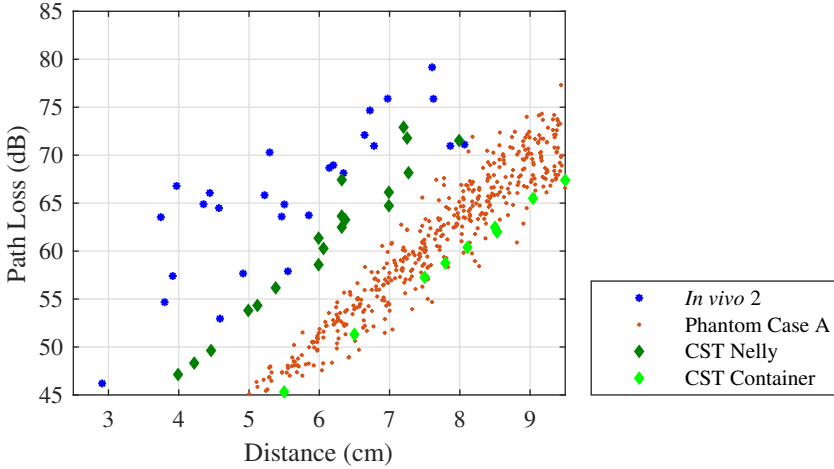
Figure 5.15: PL values for the experimental measurements in phantoms Case A, *in vivo* 2, and software simulations mimicking the human body with the CAD model Nelly and mimicking the multilayer phantom container

2 cm) for distances between 3 to 6 cm approximately, the PL values between both measurements are very similar. From the results obtained with this comparative, the measurements performed with fat phantom can be shifted up to 2 cm to the left in order to replicate as much as possible the *in vivo* results, where the pig has less than 2 cm of abdominal fat. Thus, in Fig. 5.17 the comparison between *in vivo* 2 measurements, shifted phantom measurements and software simulations (human body CST design) are shown. In this case, the agreement between results coming from the three methodologies is clearly shown. Therefore, a general PL model can be deduced from the results. It should be noted that the maximum distance achieved for simulations, phantom measurements, and *in vivo* measurements is not exactly the same. In the case of *in vivo* experiments the maximum distance measured is $d_{max} = 8.07$ cm, and for the multilayer phantom model, it is $d_{max} = 9.5$ cm or $d_{max} = 7.5$ cm (if the samples are shifted 2 cm due to the fat layer). In software-based simulations, the maximum distance is $d_{max} = 7.95$ cm.

As discussed in section 2.2 the election of one or another model to fit the measurements is a key factor. Different models are proposed using the logarithmic (Eq. 2.3) and linear (Eq. 2.4) models for that. Results are given in Table 5.2 where the Mean Squared Estimator (MSE) and the Root Mean Squared Estimator (RMSE) are computed for both the linear and logarithmic methods,
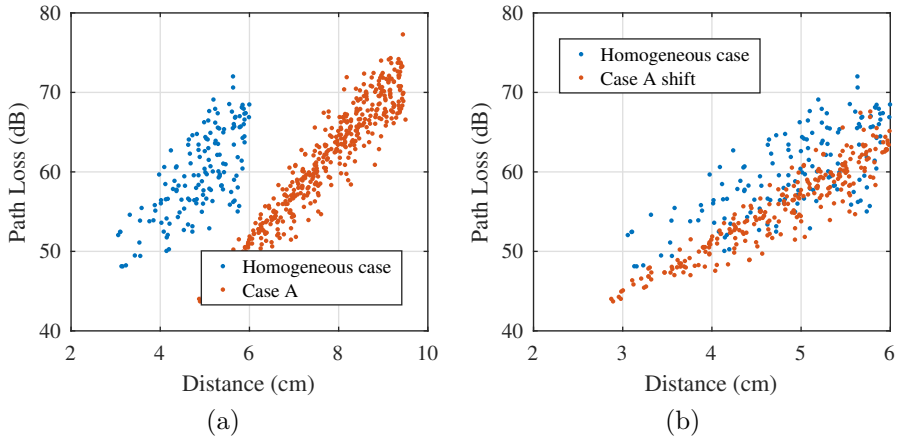
Figure 5.16: PL values comparison between the phantom measurements performed in Case A and the Homogeneous case. (a) Original values. (b) PL values of Case A 2 cm shifted to the left
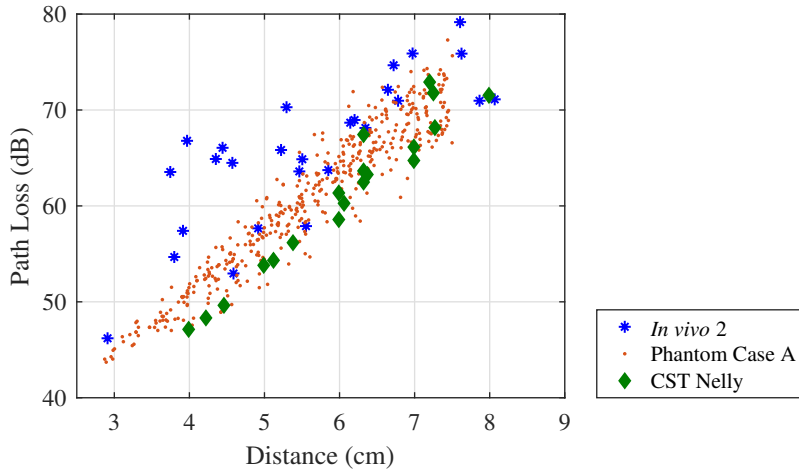
Figure 5.17: PL values of the *in vivo* 2 measurements, phantom Case A measurements 2 cm shifted, and software simulations with the human body design

for the three methodologies. Fig. 5.18 shows the measured PL models and fitting models.

From Table 5.2, the results with logarithmic and linear model seem to be unlike. Nevertheless, for all the models the MSE and the RMSE have similar

Table 5.2: Path Loss models for *in vivo* 2, phantom Case A and CST human body

	Logarithmic model	Linear Model
In vivo 2	$PL_0 = 26.23$ dB $d_0 = 1$ cm $n = 5.40$ $\mu \approx 0$ $\sigma = 4.5$ dB MSE $= 27.7$ RMSE $= 5.2$	$PL_0 = 41.56$ dB $d_0 = 1$ cm $\alpha = 4.34$ $\mu \approx 0$ $\sigma = 4.6$ dB MSE $= 29$ RMSE $= 5.4$
CST Human Model simulations	$PL_0 = -8.38$ dB $d_0 = 1$ cm $n = 8.97$ $\mu \approx 0$ $\sigma = 1.98$ dB MSE $= 7.6$ RMSE $= 2.7$	$PL_0 = 19.74$ dB $d_0 = 1$ cm $\alpha = 6.83$ $\mu \approx 0$ $\sigma = 1.95$ dB MSE $= 7.3$ RMSE $= 2.7$
Phantom Case A shifted	$PL_0 = 6.29$ dB $d_0 = 1$ cm $n = 7.38$ $\mu \approx 0$ $\sigma = 2.38$ dB MSE $= 3.9$ RMSE $= 2$	$PL_0 = 26.16$ dB $d_0 = 1$ cm $\alpha = 6.1719$ $\mu \approx 0$ $\sigma = 2.27$ dB MSE $= 3.6$ RMSE $= 1.9$
Phantom Case A original	$PL_0 = -29.76$ dB $d_0 = 1$ cm $n = 10.34$ $\mu \approx 0$ $\sigma = 2.31$ dB MSE $= 3.6$ RMSE $= 1.9$	$PL_0 = 13.82$ dB $d_0 = 1$ cm $\alpha = 6.17$ $\mu \approx 0$ $\sigma = 2.27$ dB MSE $= 3.5$ RMSE $= 1.9$

values. In Fig. 5.18 it is possible to visually realize the similarities between models for the range of given distances. Regarding the comparison between methodologies, the shifted phantom model (Case A) and the simulations are very similar, as shown for the α and n values. The *in vivo* measurements show
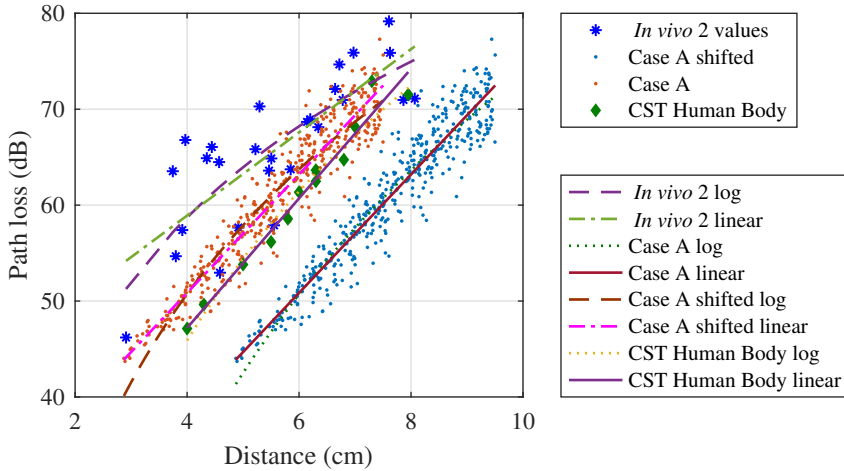
Figure 5.18: PL values and PL models (logarithmic and linear) for the *in vivo* 2, the phantom Case A measurements (original and shifted) and the software simulations mimicking the human model

slightly different results, as expected from the data values. Nevertheless, all the three trends are very similar. Please, note that the logarithmic model of the original phantom measurements is the same as the already proposed in section 5.1.1 being them completely matched.

From the given distance range (3 - 8 cm) and frequency band (3.1 - 5.1 GHz), we can assume that the exponential factor either in the logarithmic or linear model varies from $n = 5.4$ to 8.9 and $\alpha = 4.3$ to 6.8 and the standard deviation of the scattering parameter $\sigma = 2$ to 4.6 dB, for both kind of models.

Discussion with literature

These results were also discussed with other PL models present in literature (Table 2.4). As already mentioned the PL is highly affected by the location of the antenna in the human body due to the different EM properties of the human tissues, as well as by the antenna characteristic, which cannot be deembedded from measurements. Therefore, only PL models for the abdominal region or muscle tissue will be taken into account, regardless of the antennas used.

In Table 2.4, a first comparison was studied. Now, the proposed models in Table 5.2 are compared with the ones in literature that have similar characteristics as described here, i.e., same distance, frequency, scenario, and mathematical model (logarithmic or linear) to evaluate the discrepancies or similarities between the already presented and our models. For our case of study, the
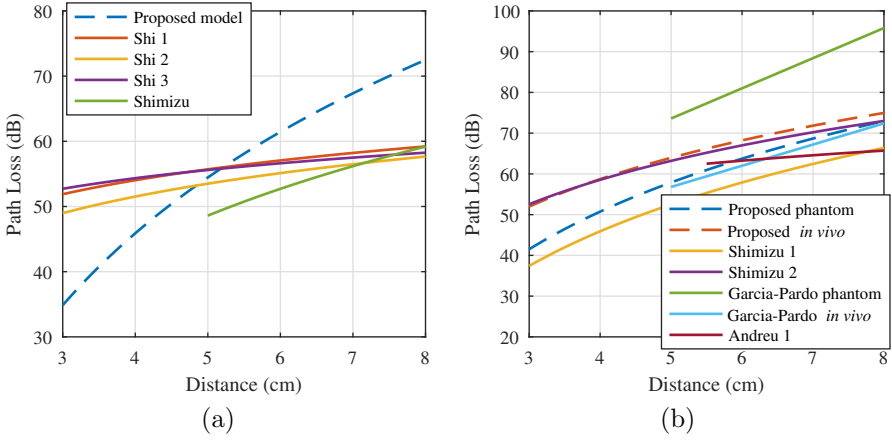
Figure 5.19: Comparison between proposed and presented models found in the literature.
(a) Simulations. (b) Experimental measurements

logarithmic models for simulations, *in vivo* and phantoms are chosen to stan-
darize with the literature, since mostly all the models are logarithmic. Fig.
5.19 shows the PL models within a distance range from 3 to 8 cm, a frequency
range between 3.1 and 5.1 GHz, and considering abdominal or GI scenario.

It should be mentioned that some models have an initial distance value
above 3 cm. In these cases, the PL model is only represented for their defined
distance range.

In Fig. 5.19 (a), the PL models as a result of software simulations are
studied. Concretely, in [20] (Shimizu), some simulations are performed in the
abdominal region for a frequency band from 3.4 to 4.8 GHz and defined from a
distance range from 5 to 9 cm. This model and the proposed model obtained
from simulations (dashed lines) have high level of agreement, with similar in-
creasing trend. In [63] (Shi 1,2,3) simulations are conducted for the same
frequency band as in [20] (Shimizu) but for a distance range from 2 to 24 cm.
In [63] three different PL models with respect the RX position were proposed.
One can observe an evident difference between models. Our model and the
models defined by Shi [63] have a different slope. This is due to the large
distance range (22 cm) defined by the authors.

In Fig. 5.19 (b) the experimental PL models obtained either for phantom
measurements or *in vivo* measurements are depicted. In [56] (Andreu), homo-
geneous phantom measurements were performed. The frequency band starts
at 3.1 to 8.5 GHz and the distance range vary from 5.5 to 20 cm. In [54],
homogeneous phantoms (Garcia-Pardo phantom) and *in vivo* measurements

(Garcia-Pardo *in vivo*) are compared. In this case, the selected frequencies vary from 3.1 to 5 GHz and the distance range from 5 to 11 cm. Stressing that this is the only linear model presented in this selection. Finally, two other experimental models presented by Shimizu *et al.* [55] (Shimizu 1, 2) are depicted. Again, the frequency band selected is from 3.4 to 4.8 GHz and the distance ranges from 3 to 12 cm. Two models are presented because they performed experiments with one antenna but two different polarizations. In Fig. 5.19 (b) it is possible to see how the *in vivo* model presented by [54] and the proposed phantom model, have a high level of agreement although the in-body antenna used were not the same. Moreover, the proposed *in vivo* model shows a quasi-perfect matching with the model presented by Shimizu 2 [55] (also deduced from *in vivo* measurements and with different antennas). Moreover, the logarithmic exponent (n) given by Shimizu 2 and Garcia-Pardo (*in vivo*), $n_{Shimizu} = 5.2$ (logarithmic) and $\alpha_{Garcia-Pardo} = 5.2$ (linear), match with the given values in Table 5.2.

In addition, it should be remarked that the models proposed by Andreu et al. [56] and Shi [63] are given for larger distance ranges than the other models: 14.5 and 22 cm respectively. This may be a reason why both of them present a large disagreement with other models presented in literature.

Summary

From the results obtained in the second *in vivo* measurements and the phantom campaign Case A the radio channel at the GI scenario for the lower part of the UWB frequency band (3.1 - 5.1 GHz) was studied. Some novelties were exposed. First, the PL models are computed using three different methodologies for the channel characterization, i.e., software simulations, experimental measurements in multilayer phantom, and *in vivo* realistic experiments. Then, for each methodology linear and logarithmic PL models were evaluated. As a result, it was shown that the measured PL data values obtained from the three methodologies have a high level of agreement between them in terms of losses as a function of distance. In addition, it was found that the width of fat present in the body affects the model only from a distance point of view, since the distance between antennas increases while not the losses.

Comparing the proposed models with the literature for similar conditions (same frequency band and scenario), some interesting conclusions were obtained. In simulations, phantom and *in vivo* measurements, the closest models were those with similar conditions while the antennas used seem not to have a decisive impact on the results. However, those with the same antennas but larger distance range or different frequency band showed higher disagreement.

For all of this, we can conclude that for the GI scenario, for a distance range from 3 to 8 cm and a frequency band of 3.1 - 5.1 GHz, the PL exponent (n) is in between [4.3 - 6.8] and [5.4 - 8.9] for linear and logarithmic models respectively. These results are supported by *in vivo* measurements in a very realistic case, where three different positions of the small bowel and colon were considered.

From the results it arises the necessity to perform phantom experiments in a container that better mimic the shape of the human body. In addition, it is desirable to obtain more *in vivo* samples, which would confirm the results obtained. Furthermore, more measurements using different kinds of antennas are necessary to confirm these findings and generalize them, which as explained in previous section, the difference between antennas is not always a crucial variable in the channel. Moreover, the values of the path loss exponent given for the model are averaged over the full frequency band, nevertheless it is needed a deeper study about how the frequency could influence the received signal in the UWB frequency band.

All these results are published in:

[80] **S. Perez-Simbor**, C. Andreu, C. Garcia-Pardo, M. Frasson and N. Cardona, "UWB Path Loss Models for Ingestible Devices," in *IEEE Transactions on Antennas and Propagations*, vol. 67, no. 8, pp. 5025-5034, Aug. 2019

5.1.4 Effect of the antenna in the channel, through *in vivo* measurements

From the measurements performed in homogeneous phantom (Section 5.1.2), the necessity of understanding how the receiving antenna affects the channel in the most realistic conditions arose. Moreover, from the results obtained in previous section, the need of having more sample points in *in vivo* measurements also appeared. In this section, first the measurements performed in the second and third *in vivo* experiments are compared, followed by the phantom measurements described in *Case Hexagonal*.

Recalling the methodology used for these measurements: for the second animal measurements, the experiments were performed using the *On 1* antenna and the *On 2* antenna. On the third animal experiments, in addition to these two antennas, *On 3* was employed, which is considered an improved antenna from the original. For the sake of simplicity, the legend in the figures will be named as On 1, On 2, and On 3, being them the omnidirectional, the directive, and the improved omnidirectional antennas respectively. Moreover, for the sake of comparison, the BW that will be taken into account will be f = [3.1, 5.1] GHz, for all the measurements either in phantom or living animal experiments
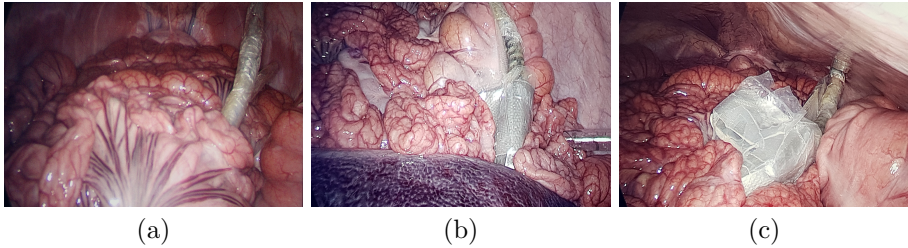
Figure 5.20: In-body positions for the *in vivo* 3 measurements. (a) In-body position 1, colon (Tx1), (b) in-body position 2, liver and colon (Tx2), (c) in-body position 3, colon (Tx3)

In Fig. 5.20, the position of the antennas is shown. Fig. 5.20 (a) and (c) are completely recovered with large bowel while the Fig. 5.20 (b) is recovered with large bowel and liver. Similarly as in the previous experiments the photos are taken when the abdomen of the pig is inflated but for the measurements the CO_2 is extracted.

In Fig. 5.21 the S-parameters for the animal experiments are shown.

Concretely, Fig. 5.21 (a) shows the reflection coefficient of the in-body antenna for the *in vivo* measurements 3. The three curves correspond to the three in-body positions (Tx1, Tx2 and Tx3) shown in Fig. 5.20. The line
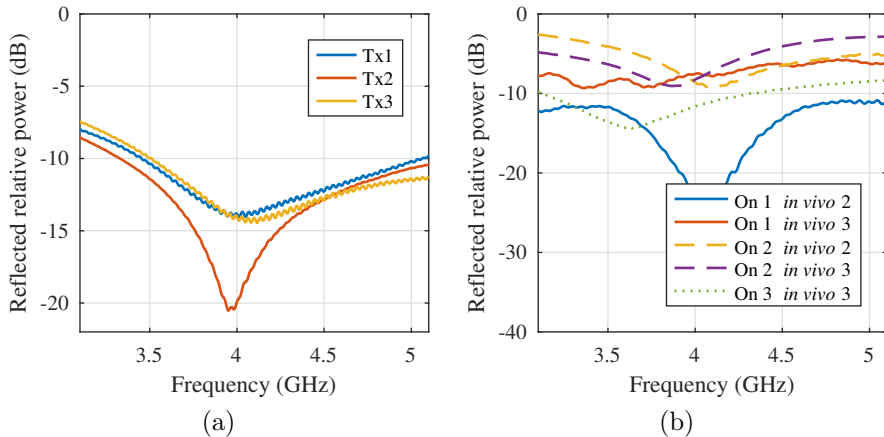
Figure 5.21: Reflection parameters for the *in vivo* 2 and 3 measurements. (a) S_{11} of the in-body antenna for the *in vivo* 2 measurements. (b) S_{11} of the on-body antennas for the two *in vivo* experiments.
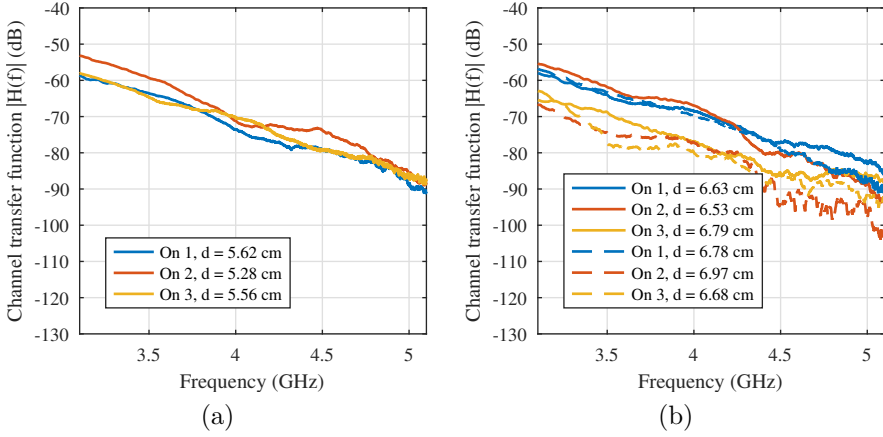
Figure 5.22: Absolute value of the channel transfer function for the *in vivo* 3 measurements. Being On 1, 2 and 3 the directive, the patch omnidirectional and patch omnidirectional improved antenna (a) for the three different antennas at the Tx 2 and Rx 1, and (b) for the Tx 2 and Rx 2 (solid lines) and Rx 10 (dashed lines)

drawn in red color, which corresponds to Tx2, shows slightly different match than the other two positions, which is easy to explain because as said the Tx2 position is surrounded by liver and large bowel, while the other two positions are only surrounded by large bowel.

In Fig. 5.21 (b) the S-parameters of the on-body antennas are depicted. In this figure we can see now the nomenclature of On 1, 2 and 3, which as said is written for the sake of clarity and simplicity in the figures, and they correspond to the omnidirectional, the directive, and the improved omnidirectional antennas respectively. From the Fig 5.21 (b) it is easy to see that even for different experiments and animals the S_{22} of the directive antenna (On 2) are very similar between them although they are not below -10 dB. On the contrary, both the patch omnidirectional and the improved antenna show different response for both experiments. Nevertheless, multiple references in literature agree in the different performance that the reflection coefficient suffers for antennas in the vicinity of human body [81].

Fig. 5.22 depicts the channel transfer function for the third *in vivo* experiment. The antennas are compared for the same conditions, this is, when the in-body antenna is placed at the same place. Fig. 5.22 (a) and (b) are the absolute value of the channel transfer function for different antennas and receivers positions for the in-body position 2 (Tx2). They are separated in two
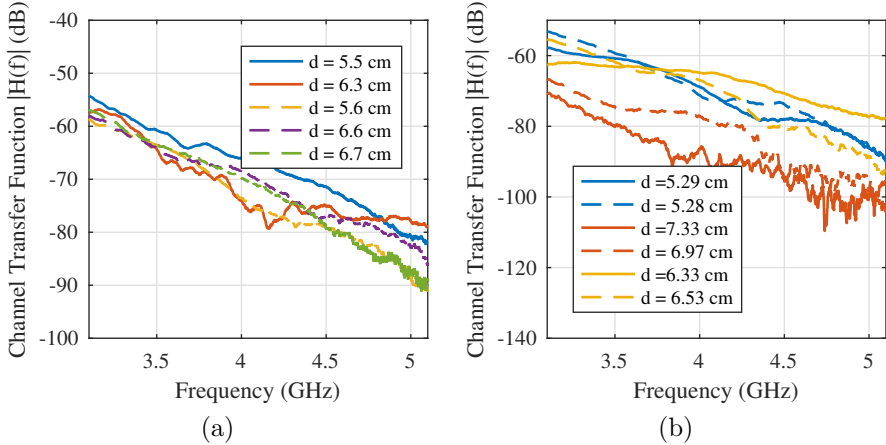
Figure 5.23: Comparison between different *in vivo* measurements (2 (solid lines) and 3 (dashed lines)). (a) Omnidirectional antenna comparison (On 1), and (b) Directive antenna (On 2)

figures to ease the interpretation of the results. Fig. 5.22 (a) depicts absolute value of the S_{21} for the Rx1, which in this case is the receiver closest to the in-body antenna. As seen in this case, the channel transfer function of all the antennas are pretty similar, quasi-identical. Fig. 5.22 (b) shows the channel transfer function for both, Rx 2 (solid lines) and Rx 10 (dashed lines). Those positions were chosen because they are the second and third closest positions of the measurement. Both positions showed very similar results for both antennas, since they are at approximately the same distance and under the same conditions. From the results obtained in the channel transfer function, even though the reflection parameters for the different antennas have noticeable differences, the absolute value of the forward transmission coefficient showed a high level of agreement between antennas.

The measurements performed at the third animal experiments had the intention to compare the performance between on-body antennas in within the experiment, but also with the previous experiments (*in vivo 2*). Therefore, the results were compared with the experiments obtained in the second *in vivo* measurements. In addition, the results performed in the second animal experiment with the directive antenna are here presented. Now, in Fig. 5.23 (a) a comparison for the patch omnidirectional antennas (On 1) is shown. Concretely, the curves of the S_{21} showed in Fig. 5.13 at d = 5.5 and 6.3 cm are
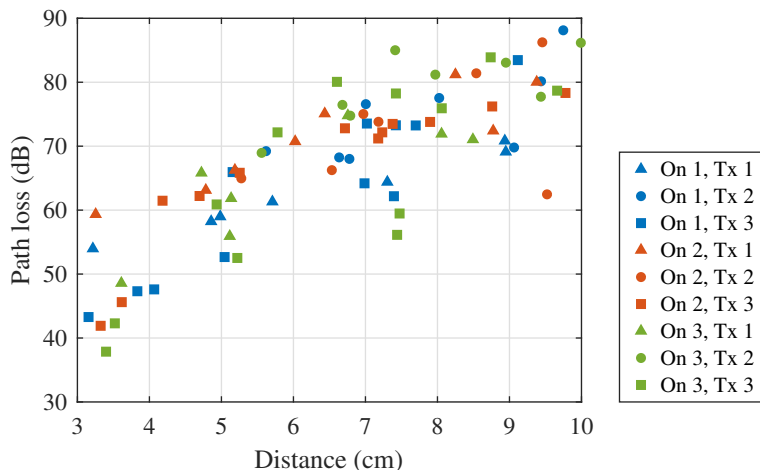
Figure 5.24: Path loss data cloud for the animal experiments 3. On 1 refers to the omnidirectional antenna, On 2 to the directive antenna and On 3 to the improved omnidirectional antenna. Tx 1,2 and 3 refer to the in-body positions for these measurements

plotted together with those showed in Fig. 5.22 (a) and (b) corresponding to the omnidirectional antenna. Those were chosen due to the similar distances they have. As seen, the slope and tendency of the channel transfer function is very similar for both antennas. It is remarkable that, even though the distances vary from 5.5 to 6.7 cm the slope and losses per cm are very similar. Nevertheless, it must be said that both experiments were performed at different pigs and different tissues might have been present between antennas.

Fig. 5.23 (b) represents the comparison for the directive antenna (On 2). The response of the directive antenna for the second *in vivo* experiment was not shown before, those correspond to the solid lines. The dashed lines correspond to the *in vivo* 3 measurements. In this graph now we can also see high level of agreement for the blue and red lines distances around 5.3 and 7 cm. Slightly different behavior is found for the yellow lines, which can be explained for the directive behavior of the antennas. There are multiple measurements, which makes difficult a detailed comparison using the channel transfer function. Therefore, in order to have a more general view, the PL for both measurements are depicted.

First, the PL values for the *in vivo* 3 measurements are plotted in Fig. 5.24. The Fig. 5.24 is divided in colors and marker shapes. The colors represent the different antennas, being the red, the blue and the green the directive, the
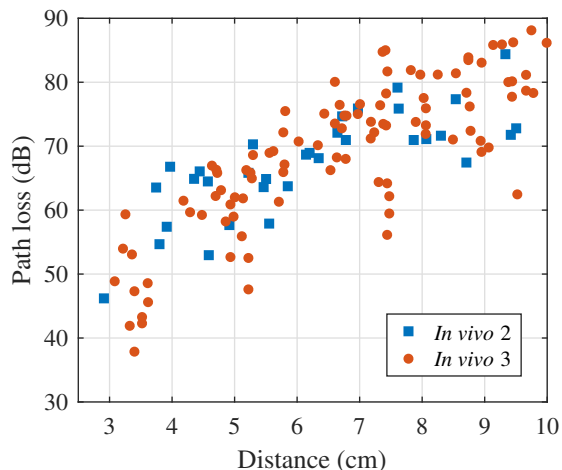
Figure 5.25: Path loss cloud for the *in vivo* measurements 2 and 3 regardless the antenna, and position

omnidirectional, and the improved omnidirectional antennas respectively (On 2, On 1, and On 3). Then, the triangular marker is the in-body positions 1, the circle the in-body position 2, and the squared marker the in-body position 3 (Tx 1, Tx 2, and Tx 3). Having a deeper look into the Fig. 5.24 the directive antenna (On 2) shows slightly higher losses in the PL values, the omnidirectional improved antenna (On 3) shows more dispersive behavior in the measurements regardless the positions of the in-body antenna. Besides, the cloud is represented from 3 to 10 cm of distance because as explained in previous sections, there is a moment when the noise becomes more predominant than the signal itself and that occurs at approximately 9.5 to 10 cm, where some values are already very close from this noise threshold.

As next step, the comparison between PL clouds is depicted in Fig. 5.25, where the PL data cloud for the *in vivo* 2 and 3 are depicted. Now, the comparison is performed for both *in vivo* experiments regardless the antennas and the in-body position. This means, that the only distinction that can be seen are both experiments. Concerning the *in vivo* 2 measurements, the data cloud in blue is the same as used in Fig. 5.14 with the addition of the PL values of the directive antenna that were not previously added. In red, the PL values depicted in Fig. 5.24. As seen both show very similar behaviour even though that different antennas were used and the pig used in both experiments are obviously different ones.

Summary

From previous results, there was a necessity to compare the impact of the on-body antenna over the in-body channel. With that aim, the *in vivo* 3 measurements were performed. In this case, an on-body grid consisting on 13 receiving positions over the abdomen, and three different on-body antennas were analyzed. Moreover, now the measurements were much focused on the frequency band under interest, i.e., 3.1 to 5.1 GHz, the low UWB frequency band.

   The results obtained showed very interesting point of view, since neither in the absolute value of the channel transfer function nor the PL values cloud, a visible distinguish between antennas is possible to recognize. Moreover, in order to perform a higher comparison, the channel transfer function and the and PL data cloud were compared with the *in vivo* 2 experiments. It should be stressed that in the second animal experiment also the directive antenna was employed, however it was not examined until now, when the comparison between antennas became an important point to explore.

   Then, from the comparison between both *in vivo* experiments, surprisingly, there is not evident differences between antennas, neither in the channel transfer function, nor in the PL data cloud. From these results, a new PL model could be obtained, and in fact, in further sections of this dissertation this issue will be analyzed. Prior to that, another exhaustive phantom measurement campaign will be performed, where also antenna and container comparison will be performed.

5.1.5   Antenna and phantom container comparison through phantom measurements

From the previous section, the need to perform measurements with more on-body antennas showed up. The living animal experiments expose that the on-body antenna used for the measurements (either omnidirectional or directive) is not as decisive for the channel as expected. The results may come up as a surprise since until now, the channel was considered antenna dependent. In this section, a comparison between 4 different antennas is conducted. Two in-body antennas and two on-body antennas are measured using the phantom measurement setup and the bi-layer phantom container. In addition, the phantom container is also a variable, which is worth to investigate about. From the results in section 5.1.3, the shape of the container and more specifically the amount of fat, highly influenced the PL model shifting the cloud two centimeters to the right i.e., increasing the distance, from the animal experiments.

Therefore, in this section, not only the on-body antennas but also the phantom containers will be compared.

Phantom container comparison

For this section, different phantom containers will be employed for different measurement campaigns. The large-squared container was used as a recipient for the liquid in both: the Case A and the Case Homogeneous, as explained in section 3. Now, the phantom containers in which the measurements will be conducted are the hexagonal container and the small-squared container. The hexagonal container has more realistic conditions, because the fat layer has more similar shape to the subcutaneous fat existent inside the human body. Moreover, the volume is equivalent to the volume of the large-squared container. On the other hand, the small-squared container has the same shape as the large-squared but much less volume, from 15.6 l to only 6.5 l. In addition, the small-squared container has only 1.5 cm of fat instead of 2 cm.

To perform the fairest comparison between containers, the same antennas are compared, with similar grid i.e., rectangular grid, and the same phantoms. The antennas used for this phantom container comparison are the ones described in section 3.1 and Figs. 3.1 and 3.3 (*In 1* and *On 1*), which ultimately they have been used for all the previous experiments.

In Fig. 5.26 the cloud of the data PL values and the PL models for the three different containers are depicted. In blue color, the cloud of the already depicted PL model for the Case A; in red color the data cloud for the hexagonal container, and finally in yellow color the PL values with the small container. For each data cloud different curves are also plotted. They correspond to the different path loss model. In Table 5.3 the PL models for the different containers are listed. Please note that the PL Model Case A and its correspondent data cloud are the same as explained in section 5.1.1.

From the Fig. 5.26 it is possible to see how the PL values between the hexagonal container and the large-squared container are very similar. They overlap for the lower values of the hexagonal measurements and the higher values of the large-squared container. A possible explanation might be due to the more realistic conditions that the hexagonal container has. The small-squared container, case C shows the same trend as the other two containers, but now, the losses are higher at shorter distances, this is due to the 1.5 cm of fat layer, the other containers have 2 cm of fat layer, which totally corresponds to this displacement that the data cloud has. In Fig. 5.27, now the data cloud of the shifted Case C and the data cloud merging the Case A and Case Hexagonal is plotted, and in Table 5.4 the values of the new PL models are shown.
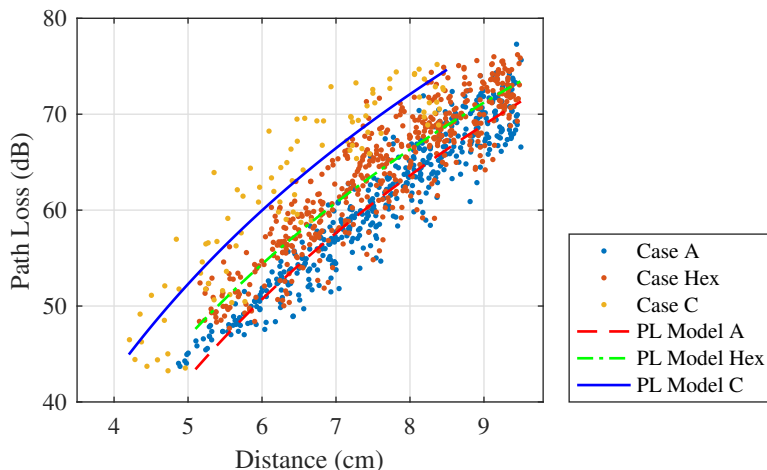
Figure 5.26: Path Loss cloud and path loss models for the phantom experiments in Case A, Case Hexagonal and Case C.

Table 5.3: Path loss models for different containers

Path Loss model Case A	Path Loss model Hexagonal	Path Loss model Case C
d = [4.8, 9.5] cm	d = [5.1, 9.5] cm	d = [4.2, 8.5] cm
f = [3.1 , 5.1] GHz	f = [3.1 , 5.1] GHz	f = [3.1 , 5.1] GHz
PL_0 = -29.76 dB	PL_0 = -20.1 dB	PL_0 = -15.50 dB
d_0 = 1 cm	d_0 = 1 cm	d_0 = 1 cm
n = 10.34	n = 9.6	n = 9.7
$\mu = 0$	$\mu = 0$	$\mu = 0$
σ = 2.31 dB	σ = 2.94 dB	σ = 3.54 dB

Interesting results arose, the shifted Case C which has the same shape than the large-square container shows the same path loss exponent (n) as the Case A. The shifted results show similar behavior to the results obtained at the *in vivo* 2 measurements (section 5.1.3). The losses at the small-squared container are higher than for the larger containers even for the shifted version, this is mostly
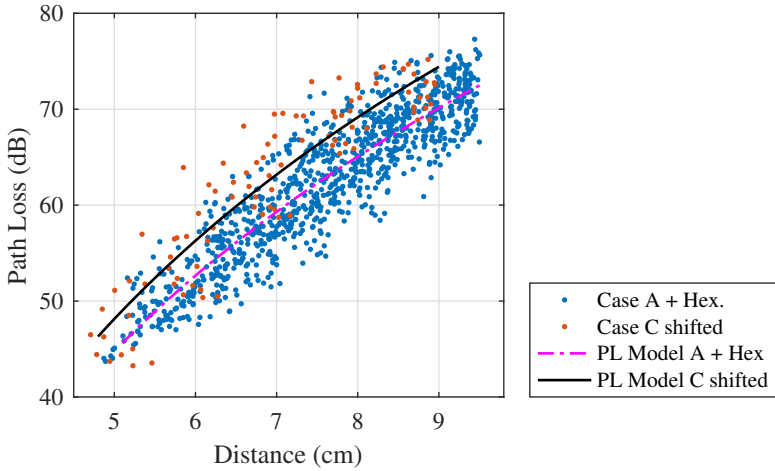
Figure 5.27: Path Loss cloud for the phantom experiments in Case A + Case Hexagonal and Case C shifted 0.5 cm to the right (increasing distance).

Table 5.4: Path loss models for different containers II

Path Loss model Case A + Hex	Path Loss model Case C shifted
d = [4.8, 9.5] cm	d = [4.7, 9] cm
f = [3.1 , 5.1] GHz	f = [3.1 , 5.1] GHz
PL_0 = -24.7 dB	PL_0 = -23.9 dB
d_0 = 1 cm	d_0 = 1 cm
n = 9.94	n = 10.3
$\mu = 0$	$\mu = 0$
$\sigma = 3.05$ dB	$\sigma = 3.49$ dB

because of the large size of muscle layer that the signal has to go through in comparison with the fat layer.

After this rough comparison between containers, the PL values showed high correspondence regardless the phantom container used. For the moment, and following the results in section 5.1.3 the path that the signal has to go through seems more important than the container itself.
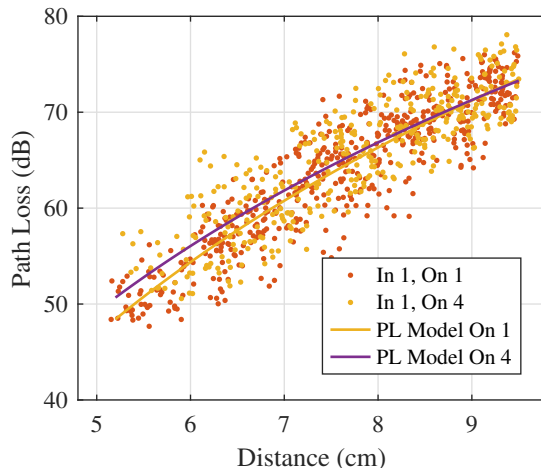
Figure 5.28: Path Loss cloud for the phantom experiments in Case Hexagonal with two different antennas (On-body)

On-body antenna comparison

After the results obtained in the previous section, in which it is concluded that the size or shape of the container itself does not highly affect the channel but the tissues (phantoms) that the signal has to go through. Moreover, it is becoming more evident that the fat tissue does not highly affect the channel. It is time now, to continue with the on-body antenna comparison started in section 5.1.4 with the *in vivo* 2 and 3 measurements. Phantom comparison is required due to the appropriate control of the variables that it is possible to have while the living animal experiments always have some uncertainties.

Recalling the antennas used for these measurements, the on-body antennas are the following, first the omnidirectional patch antenna already used in the previous sections described in section 3.1 and Fig. 3.3 as usual it will we named as *On 1*. Lastly, the on-body antenna used for these experiments is described in [82] and Fig. 3.7, and it will be named as *On 4*. Moreover, the PL data will be compared for different containers, thanks to the results obtained in previous section, in which it is seen that the container itself does not influence the measurements.

In Fig. 5.28 the PL data cloud and the PL models for different on-body antennas are depicted. This figure (Fig. 5.28) represents the PL values and the PL models for the Case Hexagonal with two different antennas. The PL data values and the PL model corresponding to In 1, On 1, are the same as

in Fig. 5.26 "Case Hex" and "PL Model Hex". The PL model obtained with the on-body antenna 4 considers the same frequency band and distance as in Table 5.3 case Hexagonal: PL_0 = -11.2 dB, n = 8.64, and σ = 3.25 dB. These results, show that the difference between antennas for the given frequency and distance is not significant. It is possible then to merge all the PL data cloud, achieving the following PL model: PL_0 = -16.7 dB, n = 9.25, and σ = 3.11 dB, which shows a high level of agreement with the PL Model in Table 5.4 "Path Loss model Case A + Hex".

In-body antenna comparison

The in-body antenna comparison is also performed in phantom measurements. Previous results in phantom (section 5.1.5) and *in vivo* (section 5.1.4) measurements, showed that the channel seems not to be as dependent from the on-body antenna as expected. Nevertheless, is this true for in-body measurements? This kind of comparison (in-body antenna comparison) is not easy to perform for many reasons, firstly, the inherent difficulties than in-body measurements already have. Secondly, the lack of in-body antennas for the UWB frequency band, it is not that common that research laboratories, institutes, or groups have multiple in-body antennas. And lastly, the resources needed to properly perform a fair comparison, maintaining as much as possible the same conditions between measurements. At the Hexagonal measurement campaign, the *In 2* antenna was measured for the first time on an accurate phantom [82]. Fig. 5.29 shows the performance of the channel transfer function for two different antennas, concretely *On 1* and *On 4*. From the Fig. 5.29 one can see how the performance for d = 5 cm to d = 7 cm is very similar between both antennas but after 7 cm, the combination of *In 2* and *On 1* degrades very fast because there signal remains constant independently of the distance. In Fig. 5.29 (b) the performance of *In 2* and *On 4* shows a more understandable behaviour until approximately 9 to 10 cm. This behavior can also be seen in the PL of the values depicted in Fig. 5.30. This figure shows the previous Fig. 5.28 and adds the PL values for the measurements performed with the directive in-body antenna (*In 2*).

As seen in the figure the results show high level of agreement between all the measurements. It is true that the pair of measurements formed by *In 2* and *On 4* shows worse performance up to 8 cm in comparison with the other measurements. These results are promising from the point of view of channel characterization because even when the antenna performance have to be taken into account in the channel model. It does not seem to highly affect the channel from a path loss point of view. Unfortunately, only phantom measurements were conducted with the *In 2* antenna and not a full model can be extracted
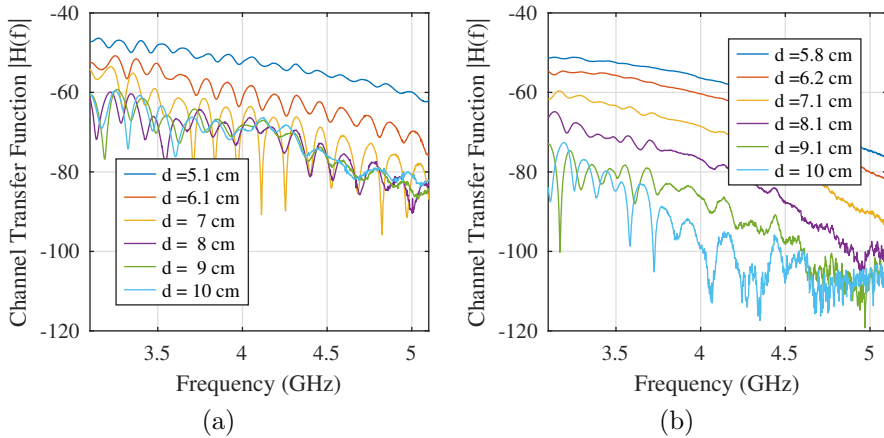
Figure 5.29: Measurements performed with the *In 2* antenna for the hexagonal container. (a) Channel transfer function for *In 2* and *On 1*. (b) Channel transfer function for *In 2* and *On 4*

from it. In any case, the results of this section open some questions related with the design of in-body antennas for the UWB frequency band as already commented. Nevertheless, that topic is out of the scope of this dissertation.
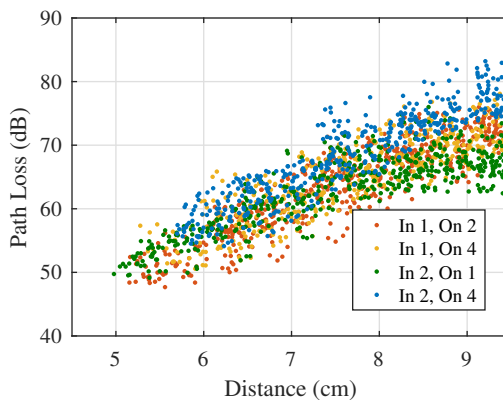
Figure 5.30: PL values for all the pairs of antennas at the hexagonal container

5.1.6 Path Loss summary

In this section the final comparison between all the PL models is performed, using the experimental phantom measurements, the *in vivo* experiments, and all the different on-body antennas described.

Sections 5.1.1 and 5.1.3, the comparisons between both experimental methodologies and software simulations were performed. The software simulations were performed with the aim of replicating the experimental measurements in the most similar way as possible. The results showed that for each case the simulations and the experiments (phantoms or living animals) were alike. From that point no more simulations were carried out, because they take long time and they do not give extra information than measurements. Moreover, in section 5.1.3 an interesting result was obtained, the fat layer located in the channel does not highly increase the losses in the system due to the path, but it increases the distance at which the channel model is valid. Concretely, after comparing the PL models in *in vivo* 2 and the experimental phantom measurements in Case A, it was concluded that the data values and models were very similar between methodologies but the distances were 2 cm different. This difference was caused by the influence of the fat layer in the system, as proved with the Case Homogeneous (section 5.1.2), concretely the fat layer was not adding losses to the system but it was increasing the distance between antennas. When shifting the data cloud 2 cm to the left, i.e., reducing the distance between antennas, the agreement between animal and laboratory experiments was obvious either graphically and mathematically. Then, the path loss models obtained were compared with previous models in literature. Not all the models are fair to compare, so only the ones with similar scenarios, frequency band, and methodologies were compared. The results showed that some path loss models in literature were similar between them when the frequency band and the proposed distance were similar. On contrary, the antennas used for the measurements did not seem a relevant factor for these similar proposed models.

This unexpected result with the antenna used in the characterization of the model led to perform more measurements, in which the objective was to compare how the channel was behaving under the same conditions for different antennas. Sections 5.1.4 and 5.1.5 performed a substantial comparison between antennas. At section 5.1.4 *in vivo* measurements 2 and 3 are compared. At these two experiments, the in-body antenna was the same one (In 1) and the on-body antennas were three different ones (On 1, 2 and 3). In addition, the location of the on-body antennas over the abdomen of the pig was changed for each experiment. The results showed no evident differences between *in vivo* experiments and the antennas used, which strengthened the results obtained in previous sections regarding the antennas used in the system. Section 5.1.5 not
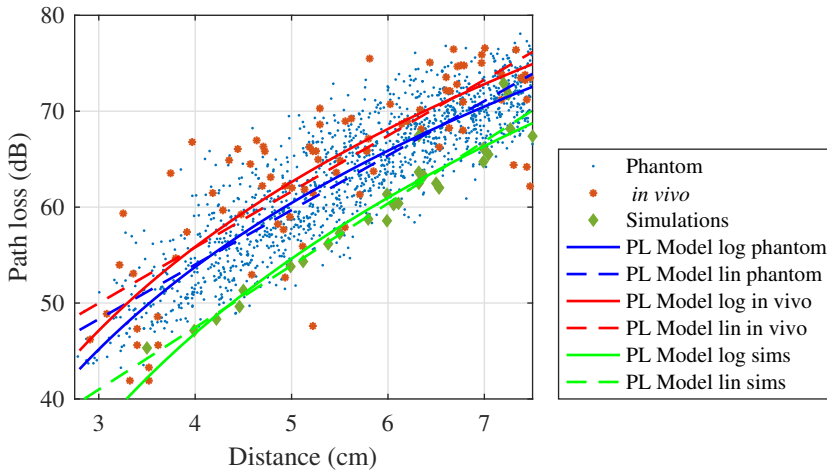
Figure 5.31: Total Path loss

only performed a comparison between receiving antennas (On 1 and On 4) in
the system, but also a phantom container comparison. The common phantom
container has one layer of a main phantom usually in a cubical shape, in this
dissertation a bi-layer phantom container having a cubical (squared) shape was
used, and also a container with two layer and 6-edges having a polyhedral shape
in the form of an hexahedron (hexagonal). The results showed that neither the
phantom container itself nor the on-body antennas are strongly affecting the
channel. For the experiments performed, the amount of phantom, the frequency
band and the distance between antennas seems more determinant.

In Fig. 5.31 the path loss data values are plotted for: the *in vivo* 2 and 3
measurements with the three on-body antennas (Fig. 5.25), the experimental
measurements in Case A, Case Hexagonal and Case C with both on-body
antennas (Fig. 5.26 and Fig. 5.28), and the software simulations. In this case
and following the procedure in section 5.1.3, the phantom measurements are
shifted, reducing in 2 or 1.5 cm the distance between antennas. It is possible to
see now how the data clouds for *in vivo* and phantom are totally overlapping
each other. Several reasons caused that, firstly, the phantom container has
more similar shape to the real abdomen of the human body, secondly, more
animal measurements were taken, and finally, different on-body antennas were
considered for the measurements. It is possible now, to propose a Path loss
model for the gastrointestinal part of the human body at the UWB frequency
band. In Table 5.5 the values for the different models shown in Fig. 5.31

Table 5.5: Path Loss models for *in vivo*, phantom measurements, and software simulations

	Logarithmic model	Linear Model
In vivo	$PL_0 = 13.82$ dB $d_0 = 1$ cm $n = 6.98$ $\mu \approx 0$ $\sigma = 5.33$ dB RMSE = 7.5	$PL_0 = 32.53$ dB $d_0 = 1$ cm $\alpha = 5.82$ $\mu \approx 0$ $\sigma = 5.45$ dB RMSE = 7.7
Phantom	$PL_0 = 12.33$ dB $d_0 = 1$ cm $n = 6.88$ $\mu \approx 0$ $\sigma = 3.39$ dB RMSE = 4.8	$PL_0 = 31.28$ dB $d_0 = 1$ cm $\alpha = 5.68$ $\mu \approx 0$ $\sigma = 3.43$ dB RMSE = 4.9
Simulations	$PL_0 = -1.49$ dB $d_0 = 1$ cm $n = 8.03$ $\mu \approx 0$ $\sigma = 2.02$ dB RMSE = 2.8	$PL_0 = 21.58$ dB $d_0 = 1$ cm $\alpha = 6.47$ $\mu \approx 0$ $\sigma = 1.83$ dB RMSE = 2.6

are described. All the models have in common the following parameters: d = [2.8, 7.5] cm, f = [3.1, 5.1] GHz and the noise floor threshold level is -90 dB. The results now, showed some some discrepancies with the original results proposed in Table 5.2. For both experimental methodologies, the RMSE for the logarithmic model is lower than for the linear model, this is a discrepancy with the previous results where, the linear model had slightly better MSE and RMSE for the phantom measurements. The phantom measurements now are in a good level of agreement with the *in vivo* experiments in terms of the methodology used. Moreover, phantom and *in vivo* measurements, have quasi-identical PL models as it is possible to see in both ways; graphically, in Fig. 5.31 the phantom and animal experiments show quasi-parallel models; and mathematically, in Table 5.5 the path loss exponent either in linear and in logarithmic show also quasi identical values. These results also match with the proposed in [80] and section 5.1.3, where the proposed values for the path

loss exponent were in within [5.4 - 8.9] for the logarithmic models and now
we find a narrower range of [6.9 - 8]. Similarly as in the previous results, the
linear PL model shows lower RMSE. Unfortunately, the number of samples
simulated are much less than the amount of sample points for both animals
and phantom experiments. Moreover, the difference between the logarithmic
and linear model in terms of RMSE is only of 0.2.

To sum up this section, a final path loss model with the form of equation 2.3
obtained from experimental measurements and simulations is proposed. This
PL model is an improvement of the previously proposed in [80] and the mean
values are: **$PL_0 = 12.7$ dB, n = 7, $\sigma = 4.3$ dB, $\mu = 0$ and $d_0 = 1$ cm**.

5.2 Delay domain analysis

The characteristics of the UWB in-body channel from a delay domain point of
view are barely explored by scientific community. This topic is highly studied in
indoor environments such as in [83–85], and some studies are found for WBANs
in an OB2OFF scenarios [49, 86].

The in-body characterization of the channel helps to understand some char-
acteristics like the multipath components (MPCs) that the signal may suffer,
and the large- and small-scale fading of the channel. In [61, 87] a first ap-
proach of IB2OB delay characterization was performed but only from simula-
tions. There are no delay models extracted from IB2OB measurements either
in phantom or *in vivo* measurements for the UWB frequency band. In this
section, the in-body channel is explored from an experimental point of view.

5.2.1 Theoretical Analysis

From measurements the S_{21} in frequency domain is obtained directly from the
VNA and the channel transfer function is calculated as follows:

$$H(f) = |S_{21}(f)| \, e^{j\phi_{S_{21}}(f)} \tag{5.2}$$

where $|S_{21}(f)|$ and $\phi_{S_{21}}(f)$ are the magnitude and the phase values of the
forward transmission coefficient. For the modeling of the SL in the channel,
only the magnitude of the H(f) was employed for all the calculations (Eq.
5.1), but now the phase information is essential to understand the temporal
behavior of the signal. Equation 5.3 shows the conversion from frequency to
delay domain through an Inverse Fourier Transform.

$$h(\tau) = IFFT[H(f)] \tag{5.3}$$

Now, the obtained values are known as the channel impulse response and it is usually modeled as:

$$h(\tau) = \sum_{i=1}^{N} \alpha_i \delta(\tau - \tau_i) \qquad (5.4)$$

where the α_i and the τ_i are the magnitude and the delay of the MPCs component. At this point it must be remained that as the measurements are real, the measurement system has a limited bandwidth. Nevertheless, it is widely known that for real measurements the signal in frequency cannot be infinite (achieving then a perfect tap-delay model of the channel). Thus, the terminology of the impulse response of the system is accepted even when the delay responses are not perfect deltas.

Lastly, from equation 5.3 the Power Delay Profile (PDP) is calculated as follows:

$$PDP(dB) = 20 \log_{10}(|h(\tau)|) \qquad (5.5)$$

The PDP is the relative received power function of the delay, with this function, it is possible to see the relative received power of the signal with respect to the delay.

5.2.2 Power Delay Profile analysis

In this section, a detailed analysis of the direct path as a function of the location of the in-body antenna is performed. Considering the phantom measurement campaign Case A (Section 4.1.1), Fig. 5.32 shows the PDP of the signal for different positions when the antenna is being displaced in different directions.

Concretely, Fig. 5.32 (a) represents the case where in Fig. 4.1 the Rx and Tx antennas are aligned i.e., the angle between them is approximately 0° either in azimuth and elevation. Then, the in-body antenna is moved 1 cm farther away from the on-body antenna in 1 cm steps (in Fig. 4.1 displacement over the X axis). As seen, from d = 4.9 cm to d = 9.9 cm there is a visible peak in the measurements, which corresponds to the first and strongest line-of-sight contribution. At further distances, the peak becomes weaker and it is not possible to discern the exact delay for the strongest contribution. It must be stressed that the amount of fat between antennas remains constant, being it 2 cm. These results are consistent with the results obtained in section 5.1.1 and Fig. 5.2, where the magnitude of the H(f) was evaluated for the same measurement campaign. In both measurements the decay power per cm is approximately 8 dB/cm.
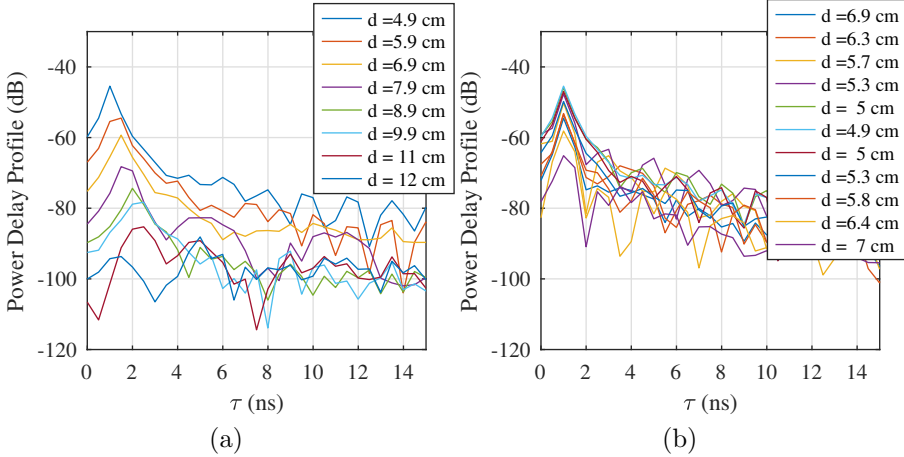
Figure 5.32: PDP for the phantom measurement campaign Case A [88]. (a) PDP when the signals are aligned and being separated. (b) PDP for the closest row in the samples grid

Having an in-depth look in Fig. 5.32 (a), it is possible to see that for d = 5.9 cm, d = 6.9 cm, and d = 7.9 cm the delay corresponding to the first contribution is the same for all the measurements, approximately $\tau = 1.5$ ns. This is due to the delay resolution ($\Delta\tau$), which is the inverse of the considered bandwidth $\Delta\tau = 1/BW = 0.5$ ns. As mentioned before, this is due to the finite response of the system that we are measuring. Moreover, continuing with this reasoning, in d = 5.9 cm and d = 7.9 cm, the difference between the strongest and the second contribution is slightly noticeable, it is then, assumable that the strongest contribution lies in between them.

Fig. 5.32 (b) shows the PDP of different samples when on Fig. 4.1 the antenna is moved over the Y-axis for the closest position of X-axis. The order of the lines is chosen to be from left-to-right over the X-axis, that is why the closest sample between antenna is located at the middle of the legend. The distances vary from d = 4.9 cm (same as in Fig. 5.32 (a) to d = 7 cm). Nevertheless, on contrary than before, all the samples plotted have the strongest contributions at $\tau = 1$ ns. These differences can be explained by the amount of fat existent between antennas, which is now larger than 2 cm in some cases, which leads to a faster signal propagation, due to the lower dielectric properties of the fat compared with the muscle. Moreover, there is also a difference in the relative received power of the signal, now the losses per centimeter vary between 6 and 10 dB/cm.
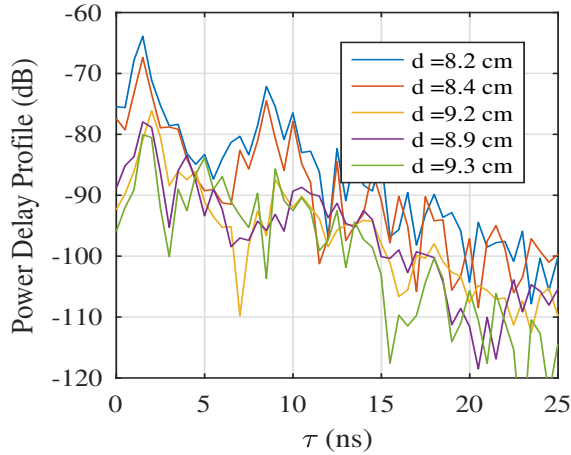
Figure 5.33: Different samples of the PDP that show possible MPCs

5.2.3 Analysis of the multipath components in the measurements

Phantom measurements

MPCs are present in the system when the signal is scattered, reflected, or diffracted due to the surrounding environment. Usually a MPC comes in the shape of a stronger peak in the PDP graph some nanoseconds later than the LoS component. Nevertheless, the resolution of our system is only $\Delta\tau = 0.5$ ns, this means that all the components that arrive in that lapse of time will be seen as the same one. The signal is then divided in bins of bin $= 0.5$ ns, which is the same as the resolution of the system. Then from the PDP, secondary peaks were detected (local maximums). There were some constraints that these maximums had to achieve in order to avoid false positives. Firstly, they had to be larger than 20% of the power of the global maximum contribution; secondly, they had to be above -90 dB otherwise they were considered noise; and lastly, only the samples below 9.5 cm in distance were taken into account, following the results obtained in previous sections. Fig. 5.33 shows and example of 5 different samples that accomplish the previous constrains and thresholds.

After this, 101 samples were computed out of 452 samples for the 5 receiver positions, and the large-squared multilayer phantom container.
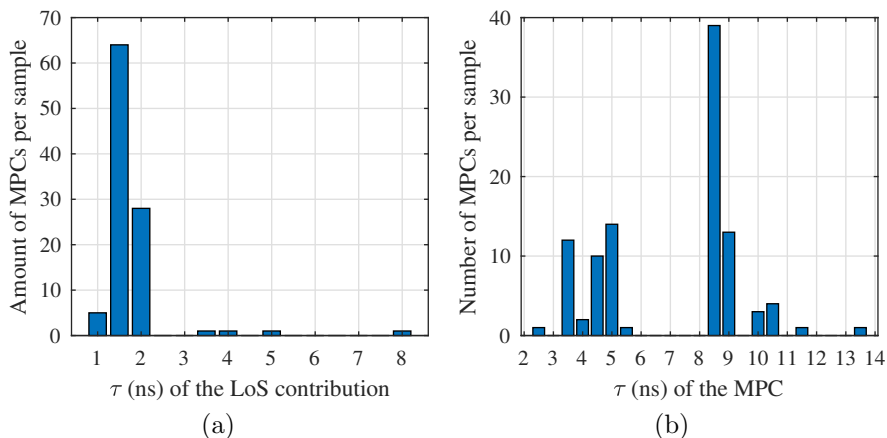
Figure 5.34: Histogram of the time of arrival of (a) the first contribution of the signal and (b) The multipath components (MPCs)

Fig. 5.34 (a) shows the histogram of the Time of Arrival (ToA) for the first direct contribution (only of those that have multipath) and Fig. 5.34 (b) shows the histogram of the time of arrival of the second contribution (MPCs).

From Fig. 5.34 it is possible to see that the ToA of the first contribution usually leads in between 1 to 2 ns. Mainly on 1.5 ns. This results nonetheless are performed with the resolution 0.5 ns. The exact ToA of the signal will vary accordingly to the position inside the container and the amount of muscle and fat tissue between antennas (further explanation in next section (section 5.2.4)). In Fig. 5.34 (b), the MPCs show two different behaviors, first a set of samples around 3 to 6 ns and then a large amount of MPCs at 8.5 - 9 ns. This difference on the ToA depends again on the relative position of the antennas inside the container. Fig. 5.35 shows the distances for which the signal present MPCs.

From Fig. 5.35 (a) the histogram of the distances for which the signal presents MPCs is shown. There is a high increase of MPCs for samples after 8 cm of distance between antennas. Moreover, Fig. 5.35 (b) gives the spatial position of the samples with MPCs. The circles in blue color represent the receivers located over the fat layer of the phantom container (Fig. 4.1) Moreover, the colorbar represent the time in nanoseconds at which the MPC arrives. The samples with darker color (less delay on the MPC), are located at the closest distances between antennas that suffer from MPCs, at distances of 7 to 7.5 cm, and they correspond to those samples in which the antennas are not aligned
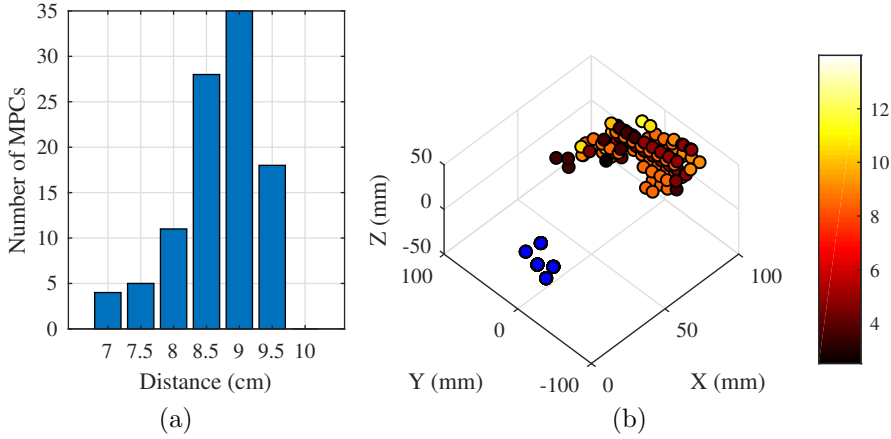
Figure 5.35: (a) Histogram of the distances for those samples with MPCs. (b) Spatial position of the samples that have MPCs. The colorbar represents the time of arrival of the MPCs in nanoseconds.

and the in-body antenna is located closer to the wall of the container. This analysis was repeated for the hexagonal container and the small container using the *On 1* and *In 1* antennas. The results are shown in Fig. 5.36 and Fig. 5.37.

The delay of the first component of the signal (LoS) is represented in Fig. 5.36 (a), where similarly as for the hexagonal container, the majority of the samples fell into 1.5 ns. In this case, a large amount of samples showed to have MPCs, contrely, 358 out of 690 samples. For the analysis of the hexagonal container, only the four frontal receivers were used. Fig. 5.36 (b) shows the delay of the first multipath component, where two different trends are seen likewise the large-squared container. First, some contributions that fall in between 5 to 6.5 ns, and then a larger number of components that fall at 8.5 ns. It must be reminded that the large-square container and the hexagonal container have the same volume and similar size but different shape. Fig. 5.36 (c) and (d), are giving the information related with the distances of the samples that showed MPCs, the large increase of samples appears at 8 cm, and even though it seems to be reduced for 9.5 cm, that is because samples larger than that value are not considered on the study. The spatial position of the samples shows similar results as before. The contributions that arrive faster are those located on the end of the sample cloud so the amount of fat between antennas is larger than 2 cm.
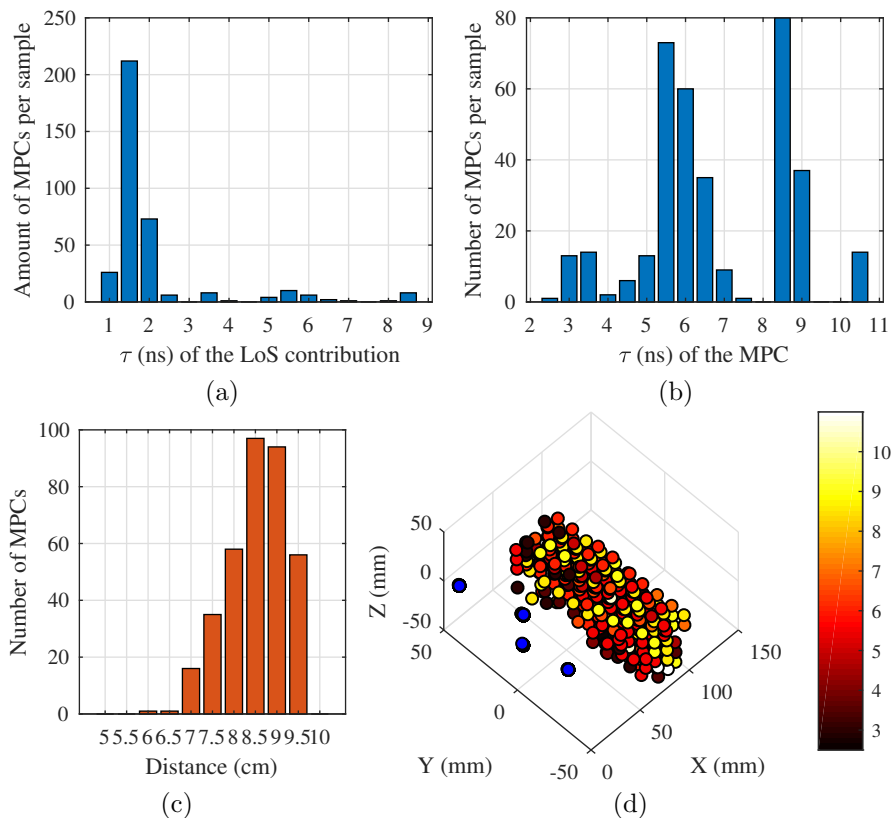
Figure 5.36: Measurements performed at the hexagonal container. (a) Histogram of the delay
(τ) of the strongest contribution of the signal. (b) Histogram of the delay of the first MPC
of the signal. (c) Histogram for distances at which MPCs appear. (d) Spatial position of the
samples that have MPCs in nanoseconds

The small squared container was also evaluated for MPCs and the results
are showed in Fig. 5.37, it must be stressed that only one receiver position was
evaluated in these measurements. Thus, the number of sample points is severely
reduced. Concretely, 120 samples, of which 47 showed MPCs. Fig. 5.37 (a)
and (b) shows the delay for the LoS and MPCs contributions per signal. The
ToA of the LoS contribution has the same distribution as before, but this is
not the same for the ToA of the MPCs as now there are a larger number of
contributions at 4.5 to 5 ns. Moreover, the histogram of the number of MPCs
per distance is shown in Fig. 5.37 (c), in which now the larger amount of
components with MPCs appears at 7.5 cm, not 8.5, and after that, the number
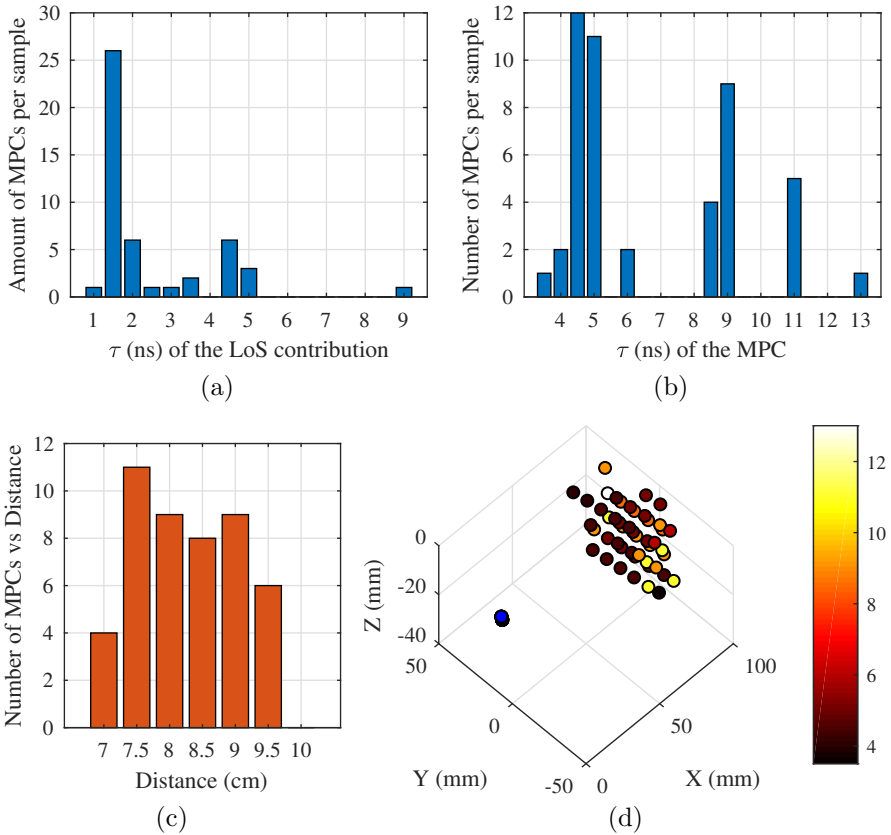
Figure 5.37: Measurements performed at the small-squared container. (a) Histogram of the delay (τ) of the strongest contribution of the signal. (b) Histogram of the delay of the first MPC of the signal. (c) Histogram for distances at which MPCs appear. (d) Spatial position of the samples that have MPCs in nanoseconds

of MPCs per distance decrease. The spatial position of the sample points with MPCs is given in Fig. 5.37 (d), where on contrary as before, the MPCs that arrive before on time are not necessarily located on the edges of the grid.

The analysis on the existence of MPCs was explored for the phantom measurements. The results showed that the signal suffers from MPCs for distances around 8 cm, but this is influenced by the amount of fat in the measurement, because for the smaller container (only 1.5 cm of fat) the MPCs appear in a large proportion at 7.5 cm.
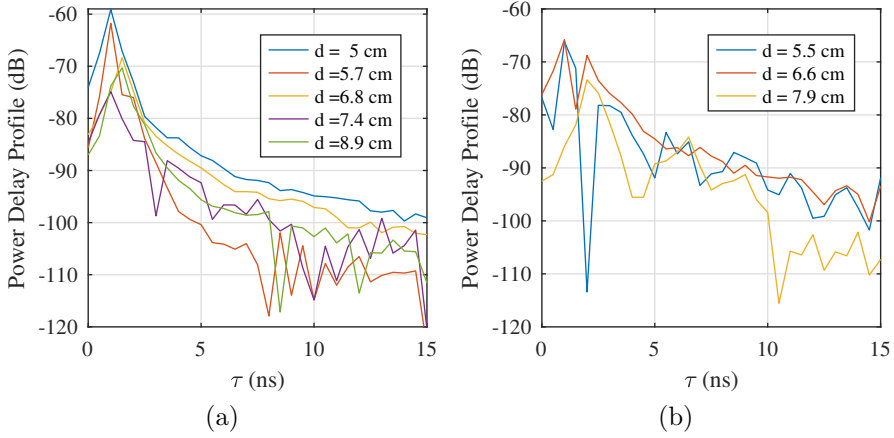
Figure 5.38: PDP for the *in vivo* measurements considering the *On 1* and *In 1* antennas.
(a) Without MPC contribution, and (b) with MPC contribution

Moreover, the ToA of the first and strongest contribution and the MPCs is
evaluated. The results showed that almost all the contributions arrive at 1.5
ns, but this highly influenced by the lack of resolution in the system.

In vivo measurements

The same methodology to post process the signal was performed with the *in
vivo* 2 and 3 experiments for the *On 1* and *In 1* antennas. And surprisingly,
they do not show MPCs. Fig. 5.38 (a) shows some curves of the PDP which
can be compared with Fig. 5.32.

As seen in Fig. 5.38 the behavior of the PDP is smoother than for the
phantom case. Nevertheless, some MPCs were found in the measurements
(Fig. 5.38). Concretely, only 6 out of 78 samples were computed that had
MPC. Of these 6 samples, they are distributed from 5.5 to 9.5 in a very regular
manner. And also the time of arrival of the multipath component is spreaded
from 2 to 10 ns. The histrograms cannot be computed now as for phantom
experiments because the amount of data is not large enough.

From the results in phantom and animal experiments, it is possible to say
that the in-body channel for the low UWB frequency band (3.1 - 5.1 GHz)
has some multipath components. Moreover, the results obtained in *in vivo*
measurements agree with those presented in [61], in which using software simu-
lations and the CLEAN algorithm [89] they detected some MPCs. Nevertheless,
both studies have some susbstancial differences, the first one is that they used

software simulations and not real experiments to study the channel. And secondly, the measured frequency band in [61] ranges from 1 to 6 GHz, which is wider than our considered bandwidth.

5.2.4 Time of arrival of the UWB signal

The results in previous sections (section 5.2.3) the time of arrival of the first and strongest components usually falls in the range of 1.5 ns. This lack of resolution might lead to some inaccuracies when it comes to calculate the ToA of the LoS of the signal. To overcome this issue First, the speed of the signal inside each tissue is computed using the well-known Equation 5.6,

$$v_{tissue} = c/\sqrt{\epsilon_r} \qquad (5.6)$$

where c is the speed of light and ϵ_r is the relative permittivity of the tissue under study. Using the **theoretical** values and the phantom values of the tissues (Fig. 3.12) the obtained range of speeds are the following:

Table 5.6: Values of the velocity of the EM signals inside the tissues

	3.1 GHz		5.1 GHz	
	Literature	Phantom	Literature	Phantom
Muscle	$\epsilon_r = 53.49$ v = 4.10	$\epsilon_r = 53$ v = 4.12	$\epsilon_r = 51.53$ v = 4.18	$\epsilon_r = 50.82$ v = 4.21
Fat	$\epsilon_r = 5.27$ v = 13.07	$\epsilon_r = 5.09$ v = 13.30	$\epsilon_r = 5.10$ v = 13.28	$\epsilon_r = 4.95$ v = 13.48

v in [cm/ns]

From the table it is possible to see how the difference between the lower and higher frequencies is barely noticeable for both, the muscle and the fat tissue. Moreover, the signals travel slower through the muscle than through fat due to the higher relative permittivity of the muscle. The average speed of the EM signal in muscle is $v_{muscle} = 4.15$ cm/ns and in fat is $v_{fat} = 13.30$ cm/ns. Therefore, the muscle is considered the most restrictive tissue in terms of speed.

To double check whether the computed speeds are correct, the speed of the signals is measured using the **phantom measurements**. Nevertheless, the lack of resolution has to be taken into account. In Fig. 5.32 (a) the antennas are considered aligned between them, this means that the amount of fat is the same for all the measurements ($d_{fat} = 2$ cm). Therefore, taking the first
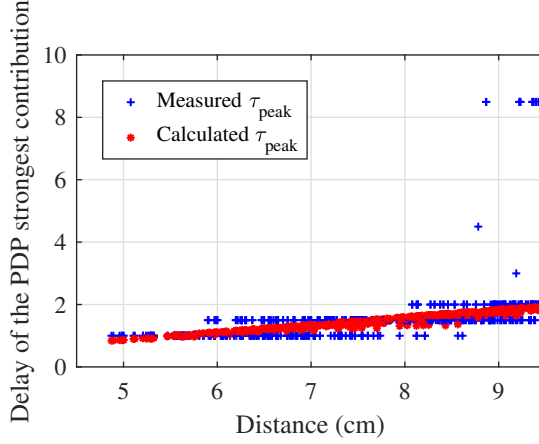
Figure 5.39: Delay of the strongest contribution for the phantom measurement campaign Case A, measured and calculated

contribution at d = 4.9, $\tau = 1$ ns and the fifth contribution at d = 8.9, $\tau = 2$ ns the speed can be computed achieving similar values:

$$v_{muscle} = ((d_{total-max} - d_{fat}) - (d_{total-min} - d_{fat})/(\tau_{max} - \tau_{min})$$
$$= (8.9cm - 2cm) - (4.9cm - 2cm))/(2ns - 1ns) = 4cm/ns$$

The results match the theoretical values considered for the muscle. The speed of the signal inside the fat cannot be computed due the already said, lack of resolution. Thus, the theoretical value of $v_{fat} = 13.30$ cm/ns obtained in Table 5.6 is considered valid.

The real ToA of the system can be computed from the measurements thanks to the magnetic sensors that give the spatial position of the antennas and also, because the size of the container is known. Therefore, it is possible to compute via basic trigonometry the amount of muscle and fat tissue that the direct LoS signal has to go through. Fig. 5.39 shows the calculated τ of the strongest contribution and the measured τ which has a resolution of $\Delta\tau = 0.5$ ns. From Fig. 5.39 the measured and calculated ToA of the strongest contribution, show high level of agreement between them, being the calculated τ_{peak} more accurate. Moreover, it is possible to see how the ToA is quite linear because the muscle is the slowest and main component of the channel. However for some distances around 8 cm some contributions show different trend and this is because the
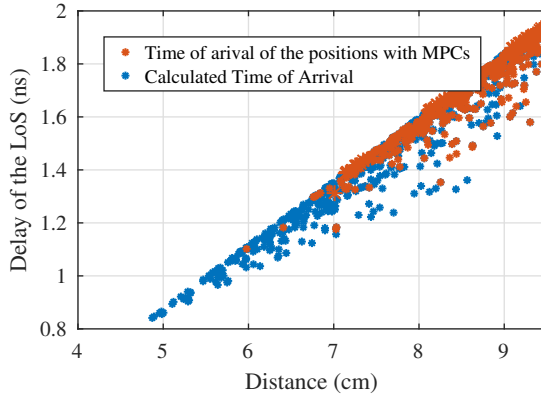
Figure 5.40: Delay of the strongest contribution of the measured samples on the three phantom container and highlighted in red the contributions that have MPCs

fat tissue between antennas is thicker, thus the signal travels at faster speed for longer distances. In addition, for distances above 8 cm some contributions arrive some nanoseconds later than they should. These results are consistent with the results obtained in section (5.2.3), where some contributions appeared several nanoseconds later than they should.

Fig. 5.40 shows the ToA of the measured phantom measurements. Now, the three measurements campaigns (Case A, Case Hexagonal, and Case C) are plotted.

Moreover, the contributions that showed MPCs are highlighted in red color. From the results it is easy to assume that almost all the contributions above 8 cm are showing MPCs for all the containers. These results seems consistent with the histograms previously plotted in which a large amount of samples were presenting MPCs.

5.2.5 Summary of the signal delay

In this section the channel obtained from measurements in the frequency domain was transformed via and inverse Fourier transform to the time domain. This means that for each channel transfer function it is possible to know the time at which the signal arrives to the receiver. On the scenarios in this dissertation the range of time and distances considered are in the order or nanoseconds and centimeters.

From the delay signal obtained, the existence or not of multipath components (MPCs) is explored. In both, phantom and *in vivo* measurements MPCs

135

were detected for distances larger than 7.5 cm and until 9.5 (which is the considered model valid). Unfortunately, the amount of samples with animals experiments are fewer than in phantoms. Therefore, it is difficult to extract conclusions from the *in vivo* measurements.

Finally, the speed of the signal through the different tissues was evaluated because the influence of fat and muscle differs on the signal. The muscle is the tissue, in which the signal travels slower and this affect the time of arrival of the signal on a quasi-linear manner. Finally, the representation of the samples with MPCs and non-MPCs was realized for the phantom measurements. The results showed that MPCs exist for distances larger or equal than approximately 7.5 cm.

The initial results of this section were published in:

[88] **S. Perez-Simbor**, C. Garcia-Pardo, and N. Cardona, "Initial delay domain UWB channel characterization for in-body area networks" in *2019 13th International Symposium on Medical Information and Communication Technology (ISMICT)*, pp. 1-5, May 2019, Oslo, Norway.

Chapter 6

Results for the Gastrointestinal scenarios for low UWB frequency signals

This chapter, shows the results of the experiments and simulations performed for the characterization of UWB signals at low frequencies

6.1   S-parameters for low UWB signals

From the software simulations performed in the human model Nelly explained in section 4.3, it was possible to compute the simulated S-parameters and then calculate the SL (or PL). On the contrary with the previous results in Chapter 5, the *in vivo* measurements were conducted with spectrum analyzer thus, the S-parameters information for experimental measurements remains unknown. In Fig. 6.1 the reflection coefficient for different tissues in simulations is depicted. As a remainder, the antennas under study in this chapter are the described in section 3.1 and shown in Fig. 3.8 (*Helical*). As seen in Fig. 6.1 the difference between muscle, small bowel and fat is barely noticeable. It is important to remark that even the S_{11} is not below -10dB, for in-body applications the effect of the EM radiation is still under study [78]; therefore it is considered between the scientific community that antennas are matched for a reflection coefficient below -6 dB [64]. The considered bandwidth in simulations is given as between

Figure 6.1: Simulated reflection coefficient S_{11} for the Helical invert-F antenna

f_{min} = 54 MHz and f_{max} = 67.2 MHz with the central frequency fc = 60.6 MHz. The constraint given by [23] for UWB signals is achieved with a signal bandwidth larger than 20% of the fc. These results were compared with the results obtained by Wang in [73], where phantom measurements using sugar phantoms were performed with the same Helical invert-F antennas. The results obtained in simulations are shifted 7 MHz to the right (higher frequencies) compared with the phantom measurements. This can be easily explained with the manufacturing process and its possible inaccuracies that may lead to some mismatch between design and final product, but also because the phantom developed for those measurements was a sugar phantom, without the exact same properties as the simulated tissues. Nevertheless, since the objective is to compare the SL, this displacement is considered negligible.

6.2 System Loss for low UWB signals

The calculation of the SL is performed by two different manners. Firstly, the calculation of the simulated values of the SL computed from the forward transmission coefficient (S_{21}) or equivalently, the channel transfer function (H(f)). Equation 5.1 was used for this calculation, being N the total number of resolution points between f_{min} = 54 MHz and f_{max} = 67.2 MHz.

On the other hand, the measurements obtained with the spectrum analyzer directly represent the received power. Therefore, in order to compute the SL

Figure 6.2: Received signal obtained with the spectrum analyzer at different distances for the low UWB frequencies

equation 2.2 is applied,

$$SL(dB) = 10 \log (p_t/p_r) = P_t(dB) - P_r(dB) \qquad \text{(2.2 revisited)}$$

where P_t and P_r are the transmitter and receiver power respectively.

Fig. 6.2 shows the received power for the *in vivo* measurements. As a remainder: the transmitted signal was produced by a FPGA transmitter, which was implanted together with the *Helical* antenna inside the abdomen of the animal (Fig. 4.9). From the *in vivo* results shown in Fig. 6.2 and the phantom results from [73] the signal is considered matched for $f_{min} = 46$ MHz to $f_{max} = 61$ MHz, in which the constraint of the 20% of the bandwidth is also achieved.

Then, the measured SL values are plotted in Fig. 6.3 for the three different in-body positions and the 12 Rx positions (section 4.2). Moreover, the simulated SL values and three different SL models are depicted. These models were computed following the common logarithmic model already used in this dissertation and given in equation 2.3. These models are listed in Table 6.1, where SL_0 is the reference value for the reference position d_0, n is the system loss exponent and d is the distance of the values. Moreover, the shadowing component follow a normal distribution with μ and σ for the mean and the variance. Moreover, for maximum distance considered is $d_{max} = 14.7$ cm, because for longer distances, there was a resolution limitation due to the spectrum analyzer sensitivity.
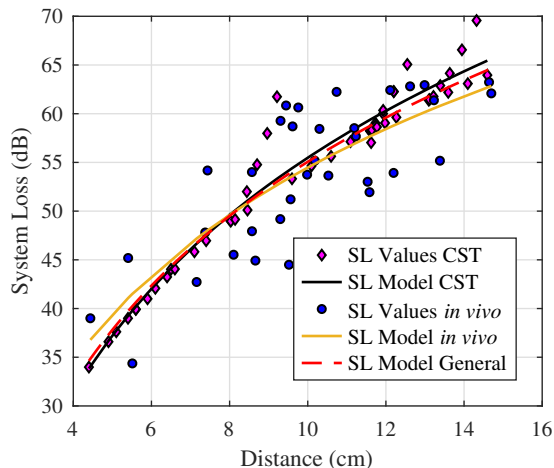
Figure 6.3: SL values and models for CST, *in vivo* measurements, and the combination of both models

As seen in Fig. 6.3 the CST values overlap with the *in vivo* measurements confirming the validity of of the experiments results. Furthermore, the SL was extended combining both the CST simulations and the animal experiments. The jointed model is given in Table 6.1 "General" column, which is applicable to a larger bandwidth, which makes it useful for future wireless medical devices.

Table 6.1: System Loss models for low UWB signals at the GI area of the human body

Parameters	*In vivo*	CST	General
$PL_0(dB)$	36.77 dB	33.84 dB	-2.24 dB
d_0	4.44 cm	4.4 cm	1 cm
n	5	6.07	5.73
μ	0	0	0
σ	4.53 dB	1.97 dB	3.33 dB
Frequency (MHz)	[46, 61]	[54,67.2]	[46,67.2]

6.3   Summary

In this chapter, two different methodologies were employed for the characterization of the IB2OB channel at low UWB frequencies for the GI area of the human body. One antenna was considered ingestible or implantable, whereas the other antenna was placed over the abdomen of the patient. The experiments carried out consisted on software simulations using commercial software modeling the EM properties of the human body, and *in vivo* experiments in a living pig. The results obtained in terms of system loss in both methodologies have high level of agreement. Therefore, a system loss model fitting all the sample poits for UWB frequency band was utilized. The obtained values were PL_0 = -2.24 dB, d_0 = 1 cm, n = 5.73, σ = 3.33 for the frequency band [46, 67.2] MHz and a maximum distance of 15 cm.

Chapter 7

Results for the cardiac scenarios at the UWB frequency band

This chapter explores the channel for the next generation of leadless pacemakers. All the measurements and assumptions are from a security and practical-case point of view. Concretely, two scenarios are considered, an in-body to in-body channel for a intra-heart to subcutaneous link, and then an eavesdropper outside the body, thence in-body to off-body channel

7.1   S-parameters for cardiac scenarios

The experimental measurements in phantom were performed with the VNA and the obtained reflection parameters are plotted in Fig. 7.1. Now the reflection parameters are displayed according to the tissue they were surrounded with. For the first IB2IB measurement, the phantom container with blood, muscle and fat was employed. Thus the S-parameters were measured on the blood and the fat tissue. On the second experiment, the blood was removed and the muscle became the main tissue. In Fig. 7.1 it can be seen how the muscle and the blood show extremely similar behavior for low UWB frequency band. On the contrary, the fat tissue shows a much different behavior but it is still matched for that frequency band. It should be noted that the antennas used for these measurements are all the same, the small CPW antenna described in section 3.1 and Fig. 3.1 (*In 1*). The last curve in Fig. 7.1 is the air reflection parameter which was measured for the IB2OFF measurements and in this case

Figure 7.1: Reflection parameters (S_{11} & S_{22}) for the cardiac scenario. *In 1* was used for the muscle, the blood and the fat, while *On 1* was used for air

the antenna employed was the on-body antenna also described in section 3.1 and Fig. 3.3, and called *On 1*.

7.2 Path loss for cardiac scenarios for the UWB frequency band

The channel transfer function was obtained from the VNA measurements and its depicted in Fig. 7.2. In Fig. 7.2 the solid lines represent the measurements of the IB2IB measurements with only two layers (muscle and fat) and the dashed lines represents the tri-layer measurements (blood, muscle and fat). Moreover, the distances (in cm) for each scenario are chosen to be similar i.e., d = 5.1 and d = 5.35, d = 7.6 and d = 7.44. What it is possible to see is that the average difference between the bi-layer and the tri-layer measurements is about 5 to 7 dB for the same or similar distances. It must be said that the three layers measurements are more irregular due to the change of medium that occurs twice.

This is more noticeable in Fig. 7.3 that represents the PL clouds for both methodologies after using Equation 5.1. In Fig. 7.3 (a) the IB2IB scenario results are shown, two different set of samples are shown. Firstly, in red color the tri-layer phantom measurements and secondly, in blue color, only muscle and fat are considered. The PL models obtained are also plotted in Fig. 7.3 (a)

Figure 7.2: Absolute value of the channel transfer function for IB2IB measurements with two and three layers of phantom. The solid lines are the muscle and fat measurements, and the dashed lines are the blood, muscle and fat phantom measurements.

and listed in Table 7.1. Graphically, it is possible to see how the PL models for each configuration look parallel between them, and this assumption is verified by the path loss exponent on Table 7.1, in which the IB2IB PL models have n = 4 and n = 3.79 for the case with and without blood respectively. Therefore, from the Fig. 7.3 (a) and Table 7.1 it is possible to say that the PL models are identical but the blood adds 6 dB of losses to the model.

From the results of the PL models for IB2IB scenarios the losses are higher when the blood is included on the measurements. This is interesting for the case under study, when a third node is eavesdropping the communication between the intra-heart node and the subcutaneous transceiver. The lower the losses, higher the possibilities to eavesdrop [15]. Therefore, since the location of the intra-heart leadless pacemaker is still under study [57], for the characterization of the eavesdropper channel, the worst case scenario for the patient will be employed, which is the case without blood. The result of the path loss for the IB2OFF case is shown in Fig. 7.3 (b). As a remainder of these configuration, the in-body antenna was placed approximately 5 cm inside the bi-layer phantom, which gives 3 cm of muscle, 2 cm of fat, and 5 cm of air for the closest position chosen (Fig. 3.15). The result listed in Table 7.1 shows a lot of similarities with the free-space model widely known, in which the path loss model exponent is 2. The distance is limited to 25 cm due to the restrictions of the small anechoic chamber.
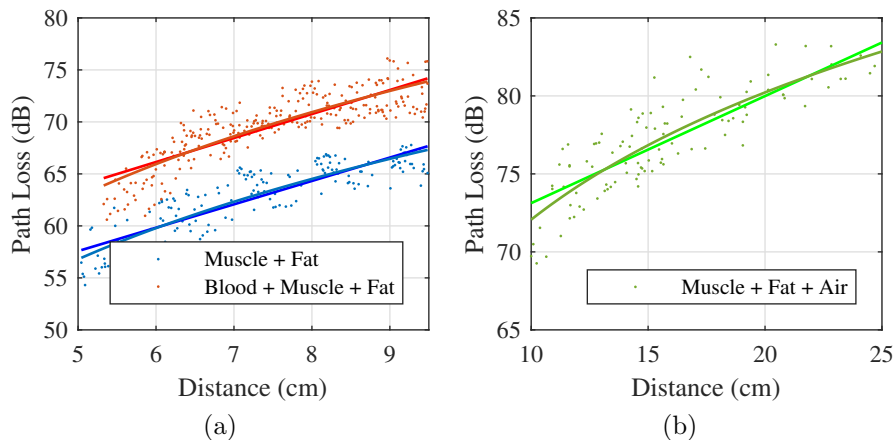
Figure 7.3: PL values and models for the different cardiac scenario. (a) IB2IB scenario with and without blood, (b) IB2OFF scenario without blood.

7.3 Summary

The results exposed in this section are a first approach for the characterization of the channel for the next generation of leadless pacemakers. Currently, there is still not an agreement about which one will be the next standard frequency for the next generation of implantable devices. The ISM band together with the UWB frequency band are being considered. These experiments and the further discussion about security are the results of a collaboration that are published in [15]. It showed that for communications purposes the ISM band showed better results that the UWB frequency band. However, the possibility of eavesdropping the communications is also higher. Nonetheless, the possibility of eavesdrop the communication at the UWB frequency band is reduced to almost 0%, which might be a more desirable option for future applications.

[15] M. F. Awan **S. Perez-Simbor**, C. Garcia-Pardo and N.Cardona "Experimental Phantom-based Security Analysis for the Next Generation Leadless Cardiac Pacemaker," *Sensors*, pp. 1-21, 2018

Table 7.1: Path Loss models for cardiac scenario

	Logarithmic model	Linear Model
IB2IB Blood + Muscle + Fat	$PL_0 = 34.83$ dB $d_0 = 1$ cm $n = 4$ $\mu \approx 0$ $\sigma = 1.64$ dB	$PL_0 = 52.30$ dB $d_0 = 1$ cm $\alpha = 2.31$ $\mu \approx 0$ $\sigma = 1.73$ dB
IB2IB Muscle + Fat	$PL_0 = 30.34$ dB $d_0 = 1$ cm $n = 3.79$ $\mu \approx 0$ $\sigma = 1.73$ dB	$PL_0 = 46.34$ dB $d_0 = 1$ cm $\alpha = 2.25$ $\mu \approx 0$ $\sigma = 1.83$ dB
IB2OFF Muscle + Fat + Air	$PL_0 = 44.98$ dB $d_0 = 1$ cm $n = 2.71$ $\mu \approx 0$ $\sigma = 1.65$ dB	$PL_0 = 66.26$ dB $d_0 = 1$ cm $\alpha = 0.69$ $\mu \approx 0$ $\sigma = 1.75$ dB

Conclusions and future work

This dissertation had as an objective to characterize the in- to on-body channel for the next generation of in-body wireless medical devices. It was mainly focused on the gastrointestinal part of the human body, thinking on practical applications such as the wireless capsule endoscopy (WCE).

Previous research in this topic can be found in literature but never in such as extensive manner as performed here. Three different methodologies that include software simulations, phantom measurements, and animal experiments were carried out. They all have some advantages and drawbacks, thus they were designed so that they were replicating each other and performing similar experiments. This manner of characterizing the channel is a novelty because only a limited number of studies are performed with animal experiments and even less are compared with phantom measurements. Furthermore, the phantoms used here are high accurate mixtures, that were replicating muscle and fat, the main components of the gastrointestinal area. Different antennas designed for the purpose of in- or on-body measurements were used under the same conditions to explore how the channel is affected by them. The results allowed to propose a path loss model for the in- to on-body channel for the low UWB frequency band (3.1 to 5.1 GHz) at the gastrointesintal scenario. Other aspects of the channel were studied, like the influence of the fat in the channel and it was demonstrated that this tissue barely affects the measurement in frequency domain. The receiving and transmitting antennas showed very little influence over the channel. The shape of the phantom container also showed minimal influence over the measurements in frequency domain but not in time domain. The exploration of the multipath components (MPCs) over the time also gave interesting results. Very few MCPs were measured for *in vivo* measurements, on the contrary, many MPCs were detected in phantom measurements for all the containers. Lastly, some *in vivo* measurements for

UWB signals at low frequencies were carried out. And also a characterization of the channel for the cardiac scenario was conducted from a security point of view, in which an eavesdropper is trying to interfere the in-body to in-body signal from outside the human body.

The results presented in this dissertation are an open gate for the next generation of wireless in-body devices. However, there is still plenty of work to do. From the experimental part of view, the use of amplifiers would increase the distance range for which the signal could be detected. In addition, the use of wireless transmitters would eliminate the cables and it would replicate more realistic conditions. Furthermore, a research on how the path loss exponent is affected by the frequency must be done. Moreover, the use of phantoms with the shape of different organs or tissues would be desirable, because it would reduce the amount of *in vivo* measurements needed. On the other hand, the channel model has to be implemented on a real system to observe their reliability.

The technology is growing fast and in the next five years, the new generation of internet of things will increase the demand of wireless controlled devices. In-body devices are not immune to this wave and they will have to increase their functionality. The increase in frequency band is a solution for the WCE and the leadless pacemaker and it will be taken into account when the necessity will become unavoidable. The WCE will have to send higher quality images to be processed using powerful algorithms of image detection. The leadless pacemaker will have to assure that the signal is not eavesdropped and hacked for safety reasons. Moreover, other devices not mentioned in this dissertation like insulin regulation devices, cochlear implants or drug delivery capsules are some examples that are under constant research. They may benefit from the advantages of the UWB frequency band or maybe they need some other solutions out of the scope of this dissertation. What it is certain, is that the future is coming and the medicine and healthcare have to be ready to collaborate in inter-sectorial teams to not to fall behind in the race of medical technology.

Acronyms

WBANs Wireless Body Area Networks

WCE Wireless Capsule Endoscopy

UWB Ultra Wide-band

GI gastrointestinal

PANs Personal Area Networks

RF radiofrequency

EM electromagnetic

HBC Human Body Communications

IB2OB in-body to on-body

IB2IB in-body to in-body

IB2OFF in-body to off-body

OB2OB on-body to on-body

OB2OFF off-body to off-body

MICS Medical Implant Communications Service

ISM Industrial Scientific and Medical radio band

LoS line-of-sight

NLoS non-line-of-sight

PL path loss

LIST OF ABBREVIATIONS

SL system loss

ITU-R International Telecommunication Union, Radiocommunication Sector

Rx receiving

Tx transmitting

CEM high computational electromagnetic

SAR Specific Absorption Rate

FDTD Finite-Differences in Time-Domain

FIT Finite Integration Technique

MoM Method of Moments

FEM Finite Element Method

VNA Vector Network Analyzer

BER Bit Error Rate

PET polyethylene terephthalate

PP polypropylene

ABS acrylonitrile butadiene styrene

SCU System Control Unit

SIU Sensor Interface Unit

MSE Mean Squared Estimator

RMSE Root Mean Squared Estimator

MPCs multipath components

PDP Power Delay Profile

ToA Time of Arrival

Variables

ε	permittivity
σ	conductivity or variance
ε_r	relative permittivity
ε_0	free space permittivity
ε_r'	dielectric constant
ε_r''	loss factor
ω	angular frequency
f	frequency
P_t	transmitted power
P_r	receiver power
PL	path loss
SL	system loss
d	distance
d_0	reference distance
PL_0	reference path loss at d_0
SL_0	reference system loss at d_0
n	system loss or path loss exponent for logarithmic models
$N(\mu, \sigma)$	scattering parameter, normal distribution
α	system loss or path loss exponent for linear models
λ	system loss or path loss exponent for exponential models
β	fitting constant exponent for exponential models
$\varnothing$	diameter
h	height
S_{11}	Reflection parameter in Port 1 of the VNA
S_{22}	Reflection parameter in Port 2 of the VNA
S_{21}	Forward transmission coefficient
$H(f)$	Channel Transfer function
α_i	magnitude of the MPC
τ_i	delay of the MPC
$\Delta\tau$	delay resolution

References

[1] "World population prospects: The 2017 revision, volume I: Comprehensive tables." United Nations, Department of Economic and Social Affairs, Population Division, Tech. Rep. ST/ESA/SER.A/399, 2017.

[2] A. Kiourti and K. S. Nikita, "A review of in-body biotelemetry devices: Implantables, ingestibles, and injectables," *IEEE Transactions on Biomedical Engineering*, vol. 64, no. 7, pp. 1422–1430, July 2017.

[3] G. Iddan, G. Meron, A. Glukhovsky, and P. Swain, "Wireless capsule endoscopy," *Nature*, vol. 405, pp. 417–418, May 2000.

[4] G. Ciuti, A. Menciassi, and P. Dario, "Capsule endoscopy: From current achievements to open challenges," *IEEE Reviews in Biomedical Engineering*, vol. 4, pp. 59–72, 2011.

[5] A. Karargyris and N. Bourbakis, "Wireless capsule endoscopy and endoscopic imaging: A survey on various methodologies presented," *IEEE Engineering in Medicine and Biology Magazine*, vol. 29, no. 1, pp. 72–83, Jan 2010.

[6] R. Noorda, A. Nevarez, A. Colomer, V. Naranjo, and V. P. Beltran, "Automatic detection of intestinal content to evaluate visibility in capsule endoscopy," in *2019 13th International Symposium on Medical Information and Communication Technology (ISMICT)*, May 2019, pp. 1–6.

[7] M. Barbi, S. Perez-Simbor, C. Garcia-Pardo, C. Andreu, and N. Cardona, "Localization for capsule endoscopy at UWB frequencies using an experimental multilayer phantom," in *2018 IEEE Wireless Communications and Networking Conference Workshops (WCNCW)*, April 2018, pp. 390–395.

[8] M. Barbi, C. Garcia-Pardo, N. Cardona, A. Nevarez, V. Pons, and M. Frasson, "Impact of receivers location on the accuracy of capsule endoscope

REFERENCES

localization," in *2018 IEEE 29th Annual International Symposium on Personal, Indoor and Mobile Radio Communications (PIMRC)*, Sep. 2018, pp. 340–344.

[9] M. Barbi, C. Garcia-Pardo, A. Nevarez, V. Pons Beltran, and N. Cardona, "Uwb rss-based localization for capsule endoscopy using a multilayer phantom and in vivo measurements," *IEEE Transactions on Antennas and Propagation*, vol. 67, no. 8, pp. 5035–5043, Aug 2019.

[10] M. Barbi, S. Perez-Simbor, C. Garcia-Pardo, and N. Cardona, "Analysis of the localization error for capsule endoscopy applications at uwb frequencies," in *2019 13th International Symposium on Medical Information and Communication Technology (ISMICT)*, May 2019, pp. 1–6.

[11] M. Maldari, K. Amara, I. Rattalino, C. Jabbour, and P. Desgreys, "Human body communication channel characterization for leadless cardiac pacemakers," in *2018 25th IEEE International Conference on Electronics, Circuits and Systems (ICECS)*, Dec 2018, pp. 185–188.

[12] R. C. Álvarez, P. Joubert, and D. Feuerstein, "Subcutaneous accelerometer-based monitoring of respiration : A pre-clinical exploration," in *2019 13th International Symposium on Medical Information and Communication Technology (ISMICT)*, May 2019, pp. 1–6.

[13] G. Rizzo, V. Loyau, R. Nocua, J. C. Lourme, and E. Lefeuvre, "Potentiality of magnetoelectric composites for wireless power transmission in medical implants," in *2019 13th International Symposium on Medical Information and Communication Technology (ISMICT)*, May 2019, pp. 1–4.

[14] D. Palaksha, G. Rizzo, R. Nocua, E. Lefeuvre, and K. Kansanen, "Load modulation for leadless pacemaker synchronization in a dual chamber pacemaker system," in *2018 IEEE-EMBS Conference on Biomedical Engineering and Sciences (IECBES)*, Dec 2018, pp. 419–425.

[15] M. F. Awan, S. Perez-Simbor, C. Garcia-Pardo, K. Kansanen, and N. Cardona, "Experimental phantom-based security analysis for next-generation leadless cardiac pacemakers," *Sensors*, vol. 18, no. 12, 2018.

[16] A. F. Molisch, "Ultra-wide-band propagation channels," *Proceedings of the IEEE*, vol. 97, no. 2, pp. 353–371, Feb 2009.

[17] R. Chavez-Santiago and I. Balasingham, "Ultrawideband signals in medicine [life sciences]," *IEEE Signal Processing Magazine*, vol. 31, no. 6, pp. 130–136, Nov 2014.

[18] E. Y. Chow, M. M. Morris, and P. P. Irazoqui, "Implantable RF medical devices: The benefits of high-speed communication and much greater communication distances in biomedical applications," *IEEE Microwave Magazine*, vol. 14, no. 4, pp. 64–73, June 2013.

[19] R. Chavez-Santiago, I. Balasingham, and J. Bergsland, "Ultrawideband technology in medicine: A survey," *Journal of Electrical and Computer Engineering*, vol. 2012, p. 9, 2012.

[20] Y. Shimizu, T. Furukawa, D. Anzai, and J. Wang, "Performance improvement by transmit diversity technique for implant ultra-wideband communication," *IET Microwaves Antennas Propagation*, vol. 10, no. 10, pp. 1106–1112, 2016.

[21] A. Ghildiyal, K. Amara, R. D. Molin, B. Godara, A. Amara, and R. K. Shevgaonkar, "UWB for in-body medical implants: A viable option," in *2010 IEEE International Conference on Ultra-Wideband*, vol. 2, Sep. 2010, pp. 1–4.

[22] P. Patel, M. Sarkar, and S. Nagaraj, "Ultra wideband channel characterization for invasive biomedical applications," in *2016 IEEE 17th Annual Wireless and Microwave Technology Conference (WAMICON)*, April 2016, pp. 1–6.

[23] "First report and order 02-48," Federal Communications Comission (FCC), Tech. Rep., 2002.

[24] C. Andreu, C. Garcia-Pardo, S. Castelló-Palacios, A. Valles-Lluch, and N. Cardona, "Frequency dependence of uwb in-body radio channel characteristics," *IEEE Microwave and Wireless Components Letters*, vol. 28, no. 4, pp. 359–361, April 2018.

[25] D. Goswami, K. C. Sarma, and A. Mahanta, "Path loss variation of on-body uwb channel in the frequency bands of ieee 802.15.6 standard," *Healthcare Technology Letters*, vol. 3, no. 2, pp. 129–135, 2016.

[26] R. C. Qiu, "A study of the ultra-wideband wireless propagation channel and optimum uwb receiver design," *IEEE Journal on Selected Areas in Communications*, vol. 20, no. 9, pp. 1628–1637, Dec 2002.

[27] "IEEE standard for local and metropolitan area networks - part 15.6: Wireless body area networks," *IEEE Std 802.15.6-2012*, pp. 1–271, Feb 2012.

REFERENCES

[28] L. Changzhi, M.-R. Tofighi, D. Schreurs, and T.-S. Horng, *Principles and Applications of RF/Microwave in Healthcare and Biosenseing.* New York Academic, 2016.

[29] D. Miklavcic, N. Pavselj, and F. X. Hart, *Electric Properties of Tissues*, April 2006, vol. 6.

[30] C. Gabriel, *Compilation of the dielectric properties of body tissues at RF and microwave frequencies.* King's College London, 1996.

[31] A. Peyman, B. Kos, M. Djokic, B. Trotovsek, C. Limbaeck-Stokin, G. Sersa, and D. Miklavcic, "Variation in dielectric properties due to pathological changes in human liver," *Bioelectromagnetics*, vol. 36, no. 8, pp. 603–612, 2015.

[32] M. Lazebnik *et al.*, "A large-scale study of the ultrawideband microwave dielectric properties of normal breast tissue obtained from reduction surgeries," *Physics in Medicine Biology*, vol. 52, pp. 2637–2656, 2007.

[33] K. Sasaki *et al.*, "Measurement of dielectric properties of the epidermis and dermis at frequencies from 0.5 GHz to 110 GHz," *Physics in Medicine Biology*, vol. 59, pp. 4739–4747.

[34] "The concept of transmission loss for radio link," *Recomendation ITU-R P.341-6*, pp. 1–9, September 2016. [Online]. Available: https://www.itu.int/dms_pubrec/itu-r/rec/p/R-REC-P.341-6-201609-I!!PDF-E.pdf

[35] K. Y. Yazdandoost and K. Sayrafian-Pour, "Channel model for body area network (BAN)," IEEE P802.15 Working Group for Wireless Personal Area Networks (WPANs), Tech. Rep., 2010.

[36] "Directive 2010/63/eu of the european parliament and of the council of 22 september 2010 on the protection of animals used for scientific purposes text with eea relevance," *Official Journal of the European Union*, vol. L 276/33, pp. 33–79, October 2010. [Online]. Available: http://data.europa.eu/eli/dir/2010/63/oj

[37] M. M. Sadiku, *Numerical techniques in electromagnetics.* CRC Press LLC, 2001.

[38] M. Sarestoniemi, M. Hamalainen, and J. Iinatti, "An overview of the electromagnetic simulation-based channel modeling techniques for wireless body area network applications," *IEEE Access*, vol. 5, pp. 10 622–10 632, 2017.

[39] K. M. S. Thotahewa, J. Redoute, and M. R. Yuce, "Propagation, power absorption, and temperature analysis of uwb wireless capsule endoscopy devices operating in the human body," *IEEE Transactions on Microwave Theory and Techniques*, vol. 63, no. 11, pp. 3823–3833, Nov 2015.

[40] S. Perez-Simbor, M. Barbi, C. Garcia-Pardo, S. Castelló-Palacios, and N. Cardona, "Initial UWB in-body channel characterization using a novel multilayer phantom measurement setup," in *2018 IEEE Wireless Communications and Networking Conference Workshops (WCNCW)*, April 2018, pp. 384–389.

[41] D. Kurup, W. Joseph, G. Vermeeren, and L. Martens, "In-body path loss model for homogeneous human tissues," *IEEE Transactions on Electromagnetic Compatibility*, vol. 54, no. 3, pp. 556–564, June 2012.

[42] T. P. Ketterl, G. E. Arrobo, and R. D. Gitlin, "SAR and BER evaluation using a simulation test bench for in vivo communication at 2.4 GHz," in *WAMICON 2013*, April 2013, pp. 1–4.

[43] K. Sayrafian-Pour, W. Yang, J. Hagedorn, J. Terrill, and K. Y. Yazdandoost, "A statistical path loss model for medical implant communication channels," in *2009 IEEE 20th International Symposium on Personal, Indoor and Mobile Radio Communications*, Sep. 2009, pp. 2995–2999.

[44] G. Vermeeren, E. Tanghe, A. Thielens, L. Martens, and W. Joseph, "In-to-out body path loss for wireless radio frequency capsule endoscopy in a human body," in *2016 38th Annual International Conference of the IEEE Engineering in Medicine and Biology Society (EMBC)*, Aug 2016, pp. 3048–3051.

[45] Y. Peng, K. Saito, and K. Ito, "Antenna design for impulse-radio-based wireless capsule endoscope communication systems," *IEEE Transactions on Antennas and Propagation*, vol. 66, no. 10, pp. 5031–5042, Oct 2018.

[46] Q. Wang, K. Wolf, and D. Plettemeier, "An UWB capsule endoscope antenna design for biomedical communications," in *2010 3rd International Symposium on Applied Sciences in Biomedical and Communication Technologies (ISABEL 2010)*, Nov 2010, pp. 1–6.

[47] S. Castelló-Palacios, C. Garcia-Pardo, A. Fornes-Leal, N. Cardona, and A. Vallés-Lluch, "Tailor-made tissue phantoms based on acetonitrile solutions for microwave applications up to 18 ghz," *IEEE Transactions on Microwave Theory and Techniques*, vol. 64, no. 11, pp. 3987–3994, Nov 2016.

REFERENCES

[48] N. Cardona *et al.*, "Synthetic model of biological tissues for evaluating the wireless transmission of electromagnetic waves," Patent WO/2017/109 252, 2015.

[49] C. Tarin, P. Marti, L. Traver, N. Cardona, J. A. Diaz, and E. Antonino, "UWB channel measurements for hand-portable devices: A comparative study," in *2007 IEEE 18th International Symposium on Personal, Indoor and Mobile Radio Communications*, Sep. 2007, pp. 1–5.

[50] E. Miralles, C. Andreu, M. Cabedo-Fabres, M. Ferrando-Bataller, and J. F. Monserrat, "UWB on-body slotted patch antennas for in-body communications," in *2017 11th European Conference on Antennas and Propagation (EUCAP)*, March 2017, pp. 167–171.

[51] W. M. Association, "World Medical Association Declaration of Helsinki: Ethical Principles for Medical Research Involving Human SubjectsWorld Medical Association Declaration of HelsinkiSpecial Communication," *JAMA*, vol. 310, no. 20, pp. 2191–2194, 11 2013. [Online]. Available: https://dx.doi.org/10.1001/jama.2013.281053

[52] A. Kiourti, K. A. Psathas, P. Lelovas, N. Kostomitsopoulos, and K. S. Nikita, "In vivo tests of implantable antennas in rats: Antenna size and intersubject considerations," *IEEE Antennas and Wireless Propagation Letters*, vol. 12, pp. 1396–1399, 2013.

[53] E. Commission, "Seventh report on the statistics on the number of animals used for experimental and other scientific purposes in the member states of the european union," Report from the commission to the council and the European Parliament, Tech. Rep., 2013.

[54] C. Garcia-Pardo, A. Fornes-Leal, N. Cardona, R. Chavez-Santiago, J. Bergsland, I. Balasingham, S. Brovoll, O. Aardal, S. . Hamran, and R. Palomar, "Experimental ultra wideband path loss models for implant communications," in *2016 IEEE 27th Annual International Symposium on Personal, Indoor, and Mobile Radio Communications (PIMRC)*, Sep. 2016, pp. 1–6.

[55] Y. Shimizu, D. Anzai, R. Chavez-Santiago, P. A. Floor, I. Balasingham, and J. Wang, "Performance evaluation of an ultra-wideband transmit diversity in a living animal experiment," *IEEE Transactions on Microwave Theory and Techniques*, vol. 65, no. 7, pp. 2596–2606, July 2017.

[56] C. Andreu, S. Castelló-Palacios, C. Garcia-Pardo, A. Fornes-Leal, A. Vallés-Lluch, and N. Cardona, "Spatial in-body channel characterization using an accurate UWB phantom," *IEEE Transactions on Microwave Theory and Techniques*, vol. 64, no. 11, pp. 3995–4002, Nov 2016.

[57] P. Bose, A. Khaleghi, M. Albatat, J. Bergsland, and I. Balasingham, "Rf channel modeling for implant-to-implant communication and implant to subcutaneous implant communication for future leadless cardiac pacemakers," *IEEE Transactions on Biomedical Engineering*, vol. 65, no. 12, pp. 2798–2807, Dec 2018.

[58] R. C. Álvarez, P. Joubert, F. Ziglio, A. Amblard, and D. Feuerstein, "Cardiac hemodynamic monitoring in the subcutaneous space : A preclinical proof-of-concept," in *2018 IEEE International Symposium on Medical Measurements and Applications (MeMeA)*, June 2018, pp. 1–6.

[59] N. R. Council, "Guide for the care and use of laboratory animals 8th ed." *Washington, D.C.: National Academies Press*, 2011.

[60] S. Stoa, R. Chavez-Santiago, and I. Balasingham, "An ultra wideband communication channel model for the human abdominal region," in *2010 IEEE Globecom Workshops*, Dec 2010, pp. 246–250.

[61] A. Khaleghi, R. Chavez-Santiago, and I. Balasingham, "Ultra-wideband statistical propagation channel model for implant sensors in the human chest," *IET Microwaves, Antennas Propagation*, vol. 5, no. 15, pp. 1805–1812, December 2011.

[62] M. Kanaan and M. Suveren, "A novel frequency-dependent path loss model for ultra wideband implant body area networks," *Measurement*, vol. 68, pp. 117 – 127, 2015. [Online]. Available: http://www.sciencedirect.com/science/article/pii/S0263224115000986

[63] J. Shi and J. Wang, "Channel characterization and diversity feasibility for in-body to on-body communication using low-band uwb signals," in *2010 3rd International Symposium on Applied Sciences in Biomedical and Communication Technologies (ISABEL 2010)*, Nov 2010, pp. 1–4.

[64] P. A. Floor, R. Chavez-Santiago, S. Brovoll, O. Aardal, J. Bergsland, O. H. N. Grymyr, P. S. Halvorsen, R. Palomar, D. Plettemeier, S. Hamran, T. A. Ramstad, and I. Balasingham, "In-body to on-body ultrawideband propagation model derived from measurements in living animals," *IEEE Journal of Biomedical and Health Informatics*, vol. 19, no. 3, pp. 938–948, May 2015.

[65] A. F. Demir, Q. H. Abbasi, Z. E. Ankarali, M. Qaraqe, E. Serpedin, and H. Arslan, "Experimental characterization of in vivo wireless communication channels," in *2015 IEEE 82nd Vehicular Technology Conference (VTC2015-Fall)*, Sep. 2015, pp. 1–2.

[66] A. F. Demir, Z. E. Ankarali, Q. H. Abbasi, Y. Liu, K. Qaraqe, E. Serpedin, H. Arslan, and R. D. Gitlin, "In vivo communications: Steps toward the next generation of implantable devices," *IEEE Vehicular Technology Magazine*, vol. 11, no. 2, pp. 32–42, June 2016.

[67] Z. Bao, Y. Guo, and R. Mittra, "An ultrawideband conformal capsule antenna with stable impedance matching," *IEEE Transactions on Antennas and Propagation*, vol. 65, no. 10, pp. 5086–5094, Oct 2017.

[68] M. M. Suzan, K. Haneda, C. Icheln, A. Khatun, and K. Takizawa, "An ultrawideband conformal loop antenna for ingestible capsule endoscope system," in *2016 10th European Conference on Antennas and Propagation (EuCAP)*, April 2016, pp. 1–5.

[69] D. Nikolayev, M. Zhadobov, L. Le Coq, P. Karban, and R. Sauleau, "Robust ultraminiature capsule antenna for ingestible and implantable applications," *IEEE Transactions on Antennas and Propagation*, vol. 65, no. 11, pp. 6107–6119, Nov 2017.

[70] C. Andreu, C. Garcia-Pardo, A. Fomes-Leal, M. Cabedo-Fabres, and N. Cardona, "Uwb in-body channel performance by using a direct antenna designing procedure," in *2017 11th European Conference on Antennas and Propagation (EUCAP)*, March 2017, pp. 278–282.

[71] Q. Zhang, X. Fang, Q. Wang, and D. Plettemeier, "Planar elliptical ring implanted antennas for UWB body area communication," in *International conference on Body Area Networks, Bodynets*, 2018.

[72] X. Fang, M. Ramzan, Q. Wang, and D. Plettemeier, "Compact antipodal vivaldi antennas for body area communication," in *Advances in Body Area Networks I*. Springer International Publishing, 2019, pp. 357–369.

[73] J. Wang, K. Nomura, H. Narita, F. Ito, D. Anzai, J. Bergsland, and I. Balasingham, "Development and in vivo performance evaluation of 10 to 60 mhz band impulse radio based transceiver for deep implantation having 10 mbps," *IEEE Transactions on Microwave Theory and Techniques*, vol. 66, no. 9, pp. 4252–4260, Sep 2018.

[74] [Online]. Available: https://www.ndigital.com/medical/products/3d-guidance/

[75] [Online]. Available: https://www.ndigital.com/medical/products/aurora/

[76] T. Kumpuniemi, T. Tuovinen, M. Hamalainen, K. Y. Yazdandoost, R. Vuohtoniemi, and J. Iinatti, "Measurement-based on-body path loss modelling for UWB WBAN communications," in *2013 7th International Symposium on Medical Information and Communication Technology (IS-MICT)*, March 2013, pp. 233–237.

[77] E. Y. Chow, M. M. Morris, and P. P. Irazoqui, "Implantable RF medical devices: The benefits of high-speed communication and much greater communication distances in biomedical applications," *IEEE Microwave Magazine*, vol. 14, no. 4, pp. 64–73, June 2013.

[78] D. Nikolayev, M. Zhadobov, and R. Sauleau, "Impact of tissue electromagnetic properties on radiation performance of in-body antennas," *IEEE Antennas and Wireless Propagation Letters*, vol. 17, no. 8, Aug 2018.

[79] S. Perez-Simbor, M. Barbi, M. Ramzan, X. Fang, C. Garcia-Pardo, N. Cardona, Q. Wang, N. Neumann, and D. Plettemeier, "Experimental path loss models comparison and localization of wireless endoscopic capsule in the ultra wideband frequency band," in *Bodynets*, October 2018, pp. 1–11.

[80] S. Perez-Simbor, C. Andreu, C. Garcia-Pardo, M. Frasson, and N. Cardona, "UWB path loss models for ingestible devices," *IEEE Transactions on Antennas and Propagation*, pp. 1–1, 2019.

[81] A. R. N. Huda, Y. Yamada, A. Nordin, and M. Shakir, "Analysis on the effects of the human body on the performance of electro textile antennas for wearable monitoring and tracking application," *Materials*, vol. 12, no. 10, p. 1636, May 2019.

[82] X. Fang, M. Ramzan, Q. Zhang, S. Perez-Simbor, Q. Wang, N. Neumann, C. Garcia-Pardo, N. Cardona, and D. Plettermeier, "Experimental in-body to on-body and in-body to in-body path loss models of planar elliptical ring implanted antenna in the ultra-wide band," in *13th International Symposium on Medical Information and Communication Technology (ISMICT)*, May 2019.

[83] M. Z. Win, R. A. Scholtz, and M. A. Barnes, "Ultra-wide bandwidth signal propagation for indoor wireless communications," in *Proceedings of ICC'97 - International Conference on Communications*, vol. 1, June 1997, pp. 56–60 vol.1.

[84] D. Cassioli, M. Z. Win, and A. F. Molisch, "The ultra-wide bandwidth indoor channel: from statistical model to simulations," *IEEE Journal on Selected Areas in Communications*, vol. 20, no. 6, pp. 1247–1257, Aug 2002.

[85] J. Keignart and N. Daniele, "Subnanosecond uwb channel sounding in frequency and temporal domain," in *2002 IEEE Conference on Ultra Wideband Systems and Technologies (IEEE Cat. No.02EX580)*, May 2002, pp. 25–30.

[86] K. Takizawa, T. Aoyagi, J. Takada, N. Katayama, K. Yekeh, Y. Takehiko, and K. R. Kohno, "Channel models for wireless body area networks," in *2008 30th Annual International Conference of the IEEE Engineering in Medicine and Biology Society*, Aug 2008, pp. 1549–1552.

[87] J. Wang and Q. Wang, "Channel modeling and ber performance of an implant uwb body area link," in *2009 2nd International Symposium on Applied Sciences in Biomedical and Communication Technologies*, Nov 2009, pp. 1–4.

[88] S. Perez-Simbor, C. Garcia-Pardo, and N. Cardona, "Initial delay domain uwb channel characterization for in-body area networks," in *2019 13th International Symposium on Medical Information and Communication Technology (ISMICT)*, May 2019, pp. 1–5.

[89] J. A. Hogbom, "Aperture Synthesis with a Non-Regular Distribution of Interferometer Baselines," *Astron. Astrophys. Suppl. Ser.*, vol. 15, pp. 417–426, 1974.